

**METAMORPHIC INVESTIGATION OF MID-P ALUMINOUS
GNEISSES FROM THE CENTRAL GRENVILLE PROVINCE**

Mackenzie Patrick, B.Sc. (Honours)

A thesis submitted to the School of Graduate studies in partial fulfillment of the
requirements for the degree of

Master of Science

Department of Earth Sciences

Memorial University of Newfoundland

January 25th 2016

ABSTRACT

This is a metamorphic study of mid-*P* anatectic aluminous gneisses from the Manicouagan and lac du Milieu areas of the central Grenville Province. The rocks are derived from hydrothermally altered felsic protoliths and were metamorphosed at granulite facies conditions during the Grenvillian orogeny. The samples come from three locations separated by several tens of kilometers and exhibit a wide range of textures and bulk compositions. However, they all have the same peak mineral assemblage: garnet + biotite + quartz + K-feldspar +/- plagioclase +/- sillimanite with retrograde cordierite in some, and show evidence of partial melting and melt loss. In terms of mineralogy and bulk composition, the samples were divided into two groups, sillimanite-rich and sillimanite-poor, with a high and low Alumina index in the AFM space, respectively.

Phase equilibria modeling in the Na₂O–CaO–K₂O–FeO–MgO–Al₂O₃–SiO₂–H₂O–TiO₂–O (NCKFMASHTO) system using Thermocalc constrained the *P*–*T* field of the peak mineral assemblage at 800–900°C and 6–11 kbar, with melt solidification in the range of 800–865°C and 6–8 kbar. The presence of sillimanite inclusions in garnet, and of only scarce, retrograde cordierite, is consistent with moderate *dP/dT* gradient ‘hairpin’ *P*–*T* paths, which were similar between the three locations.

This study also investigated the role of Fe³⁺ on phase stability in mid-*P* aluminous systems. Fe³⁺ is problematic because although it is incorporated in the NaCKFMASHTO system, it is rarely measured in modeled minerals and rocks and its value is generally assumed. Biotite may contain significant amounts of Fe³⁺, and these were analysed by

Mössbauer spectroscopy in selected samples, where they were found to be low (0-4%). In addition, the effect of increasing the bulk Fe^{3+} in the mid- P portion of phase diagrams was modeled. This increase added new minor phases and changed the phase proportions, as well as shifted phase boundaries to a small degree, but P - T paths remained largely unaffected.

Finally, the two methods commonly used in phase equilibria modeling to account for melt loss were compared. In some cases there were major differences in the topologies between the ‘melt reintegration’ and ‘adding water’ methods, but the former method is the most consistent with the rock data, and should be the method of choice.

ACKNOWLEDGEMENTS

First and foremost, I would like to thank my supervisor, Dr. Aphrodite Indares, for her time and guidance over the last few years beginning in EASC 3055, and for providing me with this opportunity and many others, including also my honours project, and the funding to go to short courses and to display my research at the 2015 Joint Assembly. Next, I would like to thank the other member of my supervisor committee, John Hanchar, for finding the time in his busy schedule to review my thesis, make suggestions, and for including me in some his experiments where he provided a wealth of knowledge. I would also like to thank my external reviewers, Toby Rivers and Carl Guilmette, for taking the time to read and make detailed comments and suggestions. I also want to thank Toby Rivers for excellent suggestions and advice throughout the entirety my research, and for reviewing my poster, and also Greg Dunning and Roger Mason for their wonderful suggestions during our coffee break meetings.

I would like to thank Mike Shaffer, David Grant and Wanda Aylward for their assistance on the SEM and microprobe, I could never have used these instruments without them, and Catherine McCammon, for the Mössbauer analyses. Additionally, most of the samples for my research were taken from previous work, where a large portion of the mineral chemistry and mineral maps were already completed. Therefore, I would like to thank these individuals as well, including Marie Letourneau, Susan Strowbridge, Marissa Hindemith and Stephanie Lasalle.

Additionally, I want to thank all the individuals and groups who provided me with funding, scholarships or other opportunities throughout my masters research, including NSERC, Aphrodite, the School of Graduate Studies, the Earth Sciences dept., Dean of Science, Buchans Scholarship Fund of ASARCO, Dr. Alfred K. Snelgrove Graduate Scholarship, and Geological Association of Canada Jérôme H. Remick Poster award. I am so grateful for this financial assistance.

Finally, I want to thank my family, fiancé, friends and colleagues in the department for their support during this research.

Table of Contents

ABSTRACT	ii
Acknowledgements	iv
List of Tables	ix
List of Figures	x
List of Abbreviations	xii
List of Appendices	xiii
Co-authorship statement	xiv
Chapter 1: INTRODUCTION	1-1
1.1. Organization of the Thesis	1-2
1.2. Background	1-3
1.2.1. Partial melting of aluminous rocks under mid- <i>P</i> conditions 1-3	
<i>1.2.1.1 Determination of P-T Conditions and Paths in Anatectic Aluminous</i>	
<i>Rocks</i>	<i>1-4</i>
1.2.2. Geological Context	1-6
<i>1.2.2.1. The Grenville Province</i>	<i>1-6</i>
<i>1.2.2.2. The Manicouagan and Lac du Milieu Areas</i>	<i>1-7</i>
1.2.3. Sample Choice and Locations	1-10
1.3. Methods	1-11
1.3.1. Documentation of textures: optical microscope and scanning electron	
microscope	1-12
1.3.2. Electron Microprobe	1-13
1.3.3. Mossbauer Spectroscopy	1-13
1.3.4. Phase equilibria modeling	1-14
<i>1.3.4.1. Calculation of bulk composition</i>	<i>1-14</i>
<i>1.3.4.2. Thermocalc</i>	<i>1-16</i>
References	1-17

Chapter 2: METAMORPHIC INVESTIGATION OF MID-<i>P</i> ALUMINOUS GNEISSES FROM THE CENTRAL GRENVILLE PROVINCE	2-1
Abstract	2-1
2.1. Introduction	2-2
2.2. Geological Context	2-3
2.2.1. The Manicouagan and Lac du Milieu areas	2-4
2.3. Textures	2-6
2.3.1. Samples from the PLV	2-7
2.3.2. Samples from the LBS	2-9
2.3.3. Samples from the GAG	2-10
2.3.4. Interpretation of textures	2-11
2.4. Mineral Chemistry	2-12
2.4.1. Garnet	2-13
2.4.2. Biotite and cordierite	2-14
2.4.3. Feldspars	2-14
2.4.4. Interpretation of mineral chemistry	2-15
2.5. Phase Equilibria Modeling	2-16
2.5.1. Bulk compositions	2-16
2.5.2. <i>P-T</i> pseudosections	2-17
2.5.2.1. <i>General topologies</i>	2-18
2.5.2.2. <i>Isomodes and isopleths</i>	2-20
2.5.2.3. <i>P-T paths</i>	2-21
2.5.3. Melt reintegration	2-24
2.5.3.1. <i>General topologies and P-T paths of melt reintegrated pseudosections</i>	2-26
2.5.4. Cordierite stability in pseudosections	2-27
2.6. Discussion and Conclusions	2-29
References	2-31

Chapter 3: THE INFLUENCE OF Fe^{3+} ON PHASE STABILITY AND <i>P-T</i> PATHS IN MID-<i>P</i> ANATECTIC GNEISSES	3-1
Abstract	3-1
3.1. Introduction	3-1
3.2. Sample Choice and Descriptions	3-5
3.2.1. Petrography	3-6
3.2.1.1. <i>Interpretation of petrography</i>	3-7
3.2.2. Mineral chemistry	3-8

3.2.3 Fe ³⁺ contents of biotite	3-9
3.3. Phase Equilibria Modeling	3-10
3.3.1. Phase equilibria diagrams calculated with measured x(Fe ³⁺) _{bi}	3-11
3.3.1.1. <i>General topologies</i>	3-12
3.3.2. Role of varying the bulk Fe ³⁺ /Fe _{tot} composition on topologies and the predicted x(Fe ³⁺) _{bi}	3-13
3.3.2.1. <i>Sample 10-AI-20A</i>	3-14
3.3.2.2. <i>Sample 10-AI-114-B1</i>	3-15
3.3.2.3. <i>Sample 10-AI-58-3B1</i>	3-16
3.3.2.4. <i>Sample 331-e2-11</i>	3-17
3.4. Discussion	3-18
3.4.1. Pseudosections using the measured x(Fe ³⁺) _{bi}	3-18
3.4.2. Effects of artificial increases of the bulk Fe ³⁺ /Fe _{tot}	3-19
3.5. Summary and Conclusions	3-23
References	3-24
Chapter 4: COMPARISON OF MELT REINTEGRATION METHODS	4-1
4.1. Introduction	4-1
4.2. Phase Equilibria Modeling	4-3
4.2.1. Comparison of melt-added and water-added pseudosections	4-4
4.2.1.1. <i>Sample 10-AI-20A</i>	4-4
4.2.1.2. <i>Sample 10-AI-114-B1</i>	4-5
4.2.1.3. <i>Sample HJ-58c</i>	4-6
4.2.1.4. <i>Sample HJ-57b</i>	4-6
4.2.1.5. <i>Sample 10-AI-76</i>	4-7
4.2.2 Comparison of melt compositions	4-7
4.3. Discussion and Conclusions	4-8
References	4-11
Chapter 5: CONCLUSIONS OF THESIS	5-1
References	5-4

List of Tables

Table 2.1. Mineral modes as determined by SEM–MLA, and compared with the modes at the solidus of the phase equilibria diagram.....	2-36
Table 2.2. Compositional ranges of garnet	2-38
Table 2.3. Compositional ranges of biotite and cordierite	2-39
Table 2.4. Compositional ranges of feldspars	2-40
Table 2.5. Bulk compositions.....	2-41
Table 2.6. Mineral isopleths of samples and P – T path coordinates	2-42
Table 3.1. Mineral modes of samples as determined by the SEM-MLA software	3-27
Table 3.2. Bulk compositions for Fe^{3+} pseudosections	3-28
Table 3.3. Predicted $x(\text{Fe}^{3+})_{\text{bi}}$ (FB) at corners of Field I in pseudosections calculated with measured $x(\text{Fe}^{3+})_{\text{bi}}$	3-28
Table 3.4. Predicted $x(\text{Fe}^{3+})_{\text{bi}}$ (FB) at corners of Field I in pseudosections calculated with $O=0.05$, 10% (A), 15% (B) and 20% (C) $x(\text{Fe}^{3+})_{\text{bi}}$	3-29
Table 4.1. Bulk compositions used for the original, melt-added and water-added pseudosections	4-13
Table 4.2. Compositions of melt	4-14

-

List of Figures

Figure 1.1. Simplified map of the Manicouagan and Lac du Milieu areas showing the distribution of the sample locations	1-23
Figure 1.2. Dehydration melting reactions of micas	1-24
Figure 1.3. Example of a simple metapelite pseudosection in the NCKFMASH system	1-25
Figure 2.1. Generalized map of the Manicouagan and Lac du Milieu areas showing the locations of the samples	2-43
Figure 2.2. SEM–MLA maps of aluminous gneisses from the PLV-LM	2-44
Figure 2.3. SEM–MLA maps of aluminous gneisses from the LBS	2-45
Figure 2.4. SEM–MLA maps of aluminous gneisses from the GAG	2-46
Figure 2.5. Photomicrographs showing characteristic microtextures	2-47
Figure 2.6. Bulk compositions of the studied samples plotted on an AFM diagram ...	2-49
Figure 2.7. P – T pseudosections for PLV samples	2-50
Figure 2.8. P – T pseudosections for LBS samples	2-51
Figure 2.9. P – T pseudosections for GAG samples	2-52
Figure 2.10. Selected P – T pseudosections with a reduced range showing relevant isopleths and inferred P – T paths	2-53
Figure 2.11. One example of a melt reintegrated P – T pseudosection from a sillimanite-rich and sillimanite-restricted sample	2-54
Figure 3.1: False colour MLA-SEM mineral maps for samples 10-AI-114B, 10-AI-58-3B1, 10-AI-20A and 331-E2-11	3-30
Figure 3.2. Pseudosections calculated with the average of the measured $x(\text{Fe}^{3+})_{\text{bi}}$ in the bulk for 10-AI-20A, 10-AI-114-B1, 10-AI-58-3B1 and 331-e2-11	3-31
Figure 3.3. Sample 10-AI-20A P – T pseudosections calculated with $O=0.05$, and O corresponding to 10% and 20% $x(\text{Fe}^{3+})_{\text{bi}}$	3-32

Figure 3.4. Sample 10-AI-114-B1 P - T pseudosections calculated with $O=0.05$, and O corresponding to 10% and 20% $x(\text{Fe}^{3+})_{\text{bi}}$	3-33
Figure 3.5. Sample 10-AI-58-3B1 P - T pseudosections calculated with $O=0.05$, and O corresponding to 10% and 20% $x(\text{Fe}^{3+})_{\text{bi}}$	3-34
Figure 3.6. Sample 331-e2-11 P - T pseudosections calculated with $O=0.05$, and O corresponding to 10% and 20% $x(\text{Fe}^{3+})_{\text{bi}}$	3-35
Figure 4.1. Melt-added and water-added pseudosections for 10-AI-20A	4-15
Figure 4.2. Melt-added and water-added pseudosections for 10-AI-114-B1	4-16
Figure 4.3. Melt-added and water-added pseudosections for HJ-58c	4-17
Figure 4.4. Melt-added and water-added pseudosections for HJ-57b	4-18
Figure 4.5. Melt-added and water-added pseudosections for 10-AI-76	4-19

List of Abbreviations

Liq: Liquid or melt

G: Garnet

Prp: Pyrope

Alm: Almandine

Grs: Grossular

Sps: Spessartine

Bi: Biotite

Sill: Sillimanite

AS: Aluminosilicate

Q: Quartz

Ksp: K-feldspar

Or: Orthoclase

Pl: Plagioclase

An: Anorthite

Ab: Albite

Cd: Cordierite

Opx: Orthopyroxene

Mu: Muscovite

Ru: Rutile

Ilm: Ilmenite

Mt: Magnetite

Sp: Spinel

Hb: Hornblende

LIST OF APPENDICES
(Available in file folder on disk)

Appendix A: Additional SEM-MLA mineral maps

Appendix B: Microprobe raw data (Excel file on disk)

Appendix C: Example of a bulk composition calculation (Excel file on disk)

Appendix D: Additional Pseudosections

Appendix E: Example of calculating the Fe³⁺ proportion in biotite on pseudosection

CO-AUTHORSHIP STATEMENT

The manuscript from **Chapter 2** entitled “Petrography and phase equilibria modeling of mid-*P* aluminous gneisses from the Grenville Province, derived from hydrothermally altered protoliths” will be edited and submitted to a peer-reviewed journal after the submission of this thesis. This paper is co-authored with Dr. Aphrodite Indares (Memorial University of Newfoundland). As the first author, I was responsible for all stages of the research project, including literature review, obtaining some of the SEM–MLA maps and microprobe data (where they were not already available in previous work), textural documentation and interpretation, bulk composition calculations, all aspects of phase equilibrium modeling, and writing the manuscript. My supervisor, Dr. Aphrodite Indares, offered knowledge and assistance in all aspects of the research, and was largely involved in editing and organizing the manuscript.

The manuscript from **Chapter 3** entitled “The influence of Fe³⁺ on phase stability and *P–T* paths in mid-*P* anatectic gneisses” will be edited and submitted to a peer-reviewed journal in the coming months. This paper is co-authored with Dr. Aphrodite Indares (Memorial University of Newfoundland) and Catherine McCammon (University Bayreuth). As the first author, I was responsible for all stages of the research project, which included the same steps as Chapter 2, with a much greater emphasis on phase equilibrium modeling. I wrote the original manuscript, and Dr. Aphrodite Indares was again largely involved in the ideas, editing, and organizing of the manuscript, as well as

providing assistance where needed. Catherine McCammon obtained $\text{Fe}^{3+}/\text{Fe}_{\text{tot}}$ in biotite compositions using Mossbauer spectroscopy.

CHAPTER 1: INTRODUCTION

High temperature metamorphic processes play a major role in the recycling of continental crust within mountain belts. This is particularly important in “large hot orogens” (Beaumont *et al.*, 2006) where high temperature (T) in the middle to lower crust results in partial melting, melt transfer and ductile rheology (Brown, 2007). Aluminous rocks are particularly useful for metamorphic studies involving anatexis because in addition to their mineral assemblages being sensitive to changes in pressure (P) and T , they are also the most fertile with respect to melting due to the presence of micas (Spear *et al.*, 1999). Deep crust is of limited accessibility in modern day orogens; however, formerly middle to lower-crust is exposed in ancient orogens by late tectonism and erosion, and provides prime material for the study of high T processes.

The Grenville Province is an example of an ancient large hot orogen that extends along the eastern part of North America and was active between 1.09 and 0.98 billion years ago (Figure 1.1; Rivers, 2008; Rivers *et al.*, 2012). Large portions of the hinterland of the central Grenville Province reached mid- P granulite facies metamorphic conditions and these areas are now exposed and available for examination.

The aim of this thesis is: (1) to evaluate the partial melting history and P – T paths followed by mid-crustal aluminous rocks during mountain building using information recorded within the minerals and textures; and (2) to determine the influence of Fe^{3+} on phase equilibria diagrams applicable to these rocks. The aluminous rocks of this study

come from several localities within the hinterland of the central Grenville Province (in the Manicouagan and Lac du Milieu areas) that were metamorphosed to mid- P granulite facies, and show evidence of partial melting. The samples have a wide range of compositions and textures, most of them having atypical chemistry and odd traits because they are derived from hydrothermally altered felsic protoliths.

This study builds on previous research on aluminous rocks from the central Grenville (Strowbridge, 2006; Letourneau, 2011; Hindemith, 2013; Patrick, 2013), and involves documentation of textures in polished thin sections, mineral chemistry, and phase equilibria modeling.

1.1 ORGANIZATION OF THE THESIS

This thesis is organized into five chapters. The rest of this chapter includes: (a) background information on partial melting of mid- P aluminous rocks, on the Grenville Province and on the study area; and (b) the methodology.

Chapters 2 and 3 are in the form of manuscripts which will be edited later for publishing. **Chapter 2** is the main part of the thesis. In this chapter, the mineral assemblages and textures, along with mineral chemistry, are documented and interpreted in terms of pressure-temperature paths (P - T paths) within the framework of P - T diagrams constructed by phase equilibria modeling for specific bulk rock compositions (pseudosections). **Chapter 3** focuses on modeling the effect of the Fe^{3+} parameter in the bulk composition, using four samples from Chapter 2. This issue is important because

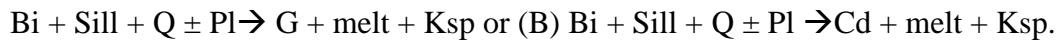
although phase equilibria modeling takes into account Fe^{3+} , in most published studies the values used are assumed. **Chapter 4** is a short communication that explores the differences between methods used to determine the mineral stability fields that are relevant to the prograde portions of P - T paths, assuming that some melt was extracted from the rocks during anatexis, and **Chapter 5** contains the conclusions of the thesis. References are listed at the end of each chapter and additional data are shown in **Appendices A-E**.

1.2 BACKGROUND

1.2.1 Partial melting of aluminous rocks under mid- P conditions

Partial melting occurs in aluminous rocks such as metapelites and metagreywackes under upper-amphibolite and granulite-facies metamorphic conditions. Under these conditions, melt is stabilized by the dissolution of OH^- available in micas (dehydration melting reactions; Spear *et al.*, 1999). With increasing T , muscovite is the first mica involved in dehydration melting, by a reaction of the type: $\text{Mu} + \text{Q} \pm \text{Pl} \rightarrow \text{Ksp} + \text{AS} + \text{melt}$ (mineral abbreviations are listed on page xii), which is the first reaction to produce significant melt (Spear *et al.*, 1999). The exhaustion of muscovite by this reaction marks the boundary of the granulite facies, after which biotite dehydration melting begins. Melting involving biotite can be represented in the simple system NaKFMASH, where it occurs by both continuous and discontinuous reactions, portrayed by fields and lines in Figure 1.2, respectively (from Spear *et al.*, 1999). Melting starts in

divariant field II by one of two reactions that are dependent on the bulk composition: (A)



However, because typical aluminous rocks have high $x(\text{Fe}) = \text{Fe}/(\text{Fe} + \text{Mg})$, reaction A is more common.

Evidence of this reaction at the thin section scale includes garnet overgrowths on sillimanite, and polyminerallic inclusions in porphyroblastic garnet. These inclusions consist of variably resorbed reactants (Bi, Sill, Q) surrounded by a pool of feldspar which is interpreted to be solidified former melt (Platten, 1983; Vernon and Collins, 1988; Sawyer, 1999; Indares *et al.*, 2008; Guilmette *et al.*, 2011). These textures typically occur in garnet because of its refractory nature, however, such pseudomorphed melt pools can also be found in the matrix where they start as pockets with low dihedral angles and develop a more cusped shape as the melt volume increases (Holness *et al.*, 2011). Furthermore, corrosion of garnet by biotite \pm sillimanite is indicative of reaction A in reverse because the melt releases H₂O as it solidifies during cooling (Sawyer, 2008). For this reason, preservation of the peak assemblage suggests at least some melt loss since water, which is required for retrogression, is lost with the melt (White and Powell, 2002). Melt migration is facilitated by deformation, and is common in orogenic environments (Brown, 2007).

1.2.1.1 Determination of P–T Conditions and Paths in Anatectic Aluminous Rocks

Classical thermobarometry was used as the main method of determining pressure-temperature (P - T) conditions for many years. This method involves the calculation of “equilibrium lines” for two continuous reactions, a thermometer and a barometer, involving minerals with compositions sensitive to T and/or P . The intersection of these lines provides an estimate of the P - T conditions of equilibrium, mainly for the thermal peak, but also for points along the retrograde P - T path (Spear, 1993). The most common thermobarometric reactions used for aluminous rocks are the Fe^{2+} -Mg exchange reaction between biotite and garnet, and the GASP reaction $\text{G}_{\text{Grs}} + \text{AS} + \text{Q} \rightarrow \text{Pl}_{\text{An}}$.

However, the application of this method in anatectic rocks has some limitations. First, it is based on the assumption that the assemblage used retains the composition achieved at the thermal peak. However, in granulite facies rocks, biotite may be entirely produced during melt crystallization, in which case, it may be unrelated to the thermal peak. Furthermore, the electron microprobe cannot discriminate between Fe^{2+} and Fe^{3+} so there also may be an overestimation of the concentration of Fe^{2+} in ferromagnesian minerals. Fe^{3+} is most common in biotite in these rocks (4-16% of total Fe; Dyar *et al.*, 2002; Cesare, 2005), and if not taken into account, may affect phase stability (ex. Diener and Powell, 2010).

An alternative approach for assessing the P - T history of metamorphic rocks is phase equilibria modeling which has been increasingly used within the last decade. P - T pseudosections are phase diagrams specific to a particular bulk composition and show the P - T stability fields of mineral assemblages possible. These diagrams allow for the use of

a wide selection of mineral composition parameters to determine P – T conditions, and provide a framework to interpret textures and mineral chemistry of the rock in terms of P – T paths by: (1) delineating the P – T stability of the mineral assemblage of the peak; (2) predicting the P – T conditions by comparing observed mineral chemistry with mineral composition isopleths; (3) constraining portions of the P – T path by comparing textures with the patterns of mineral proportion isopleths; and (4) by comparing the mineral proportions of the rock to those at the solidus (Indares *et al.*, 2008). In the case of aluminous systems, these diagrams can also account for melt loss (White *et al.*, 2002), therefore phase equilibria modeling is the method of choice for determining P – T paths in anatectic aluminous rocks. In this work, we are mainly interested in the field with the mineral assemblage Liq+Bi+Sill+G+Ksp+Pl+Q (Figure 3.3).

1.2.2 Geological context

1.2.2.1. The Grenville Province

The Grenville Province mainly consists of arc terranes developed along the southeast margin of proto-Laurentia between 1700 and 1230 Ma (Rivers and Corrigan, 2000; Gower and Krogh, 2002) that were subjected to a continental collision between 1090 and 980 Ma (Grenvillian Orogeny; see review in Rivers, 2008). This long duration major mountain building event led to the formation of possibly the first large hot orogen in Earth's history, of which the Himalayan mountain chain is a present day analog (Beaumont *et al.*, 2010).

The Grenville Province is divided into two first order orogenic belts. The structurally lowest Parautochthonous Belt marks the NW rim of the orogen, and is made up of foreland units that were deformed and metamorphosed during the Rigolet phase (1000–980 Ma) of the Grenvillian Orogeny (Rivers *et al.*, 1989; Rivers, 2008). The Allochthonous Belt represents the hinterland of the orogen (Rivers, 2008). Large parts of this belt were metamorphosed to mid-*P* (and locally high-*P*) granulite facies conditions during the Ottawa phase (1090–1020 Ma) of the Grenvillian orogeny. High temperatures resulted in partial melting in the low to mid-crust, leading to a high ductility and melt transfer. Heterogeneous ductile flow is inferred to be a critical part of the evolution of the orogen in current tectonic models (Jamieson *et al.* 2007, 2010; Jamieson and Beaumont, 2011), and on the presumed development of an orogenic plateau (Rivers, 2008). The mid-*P* and high-*P* parts of the hinterland are juxtaposed with lithotectonic domains that have experienced lower grades of metamorphism: the low-*P* segment and the Orogenic Lid. This configuration is inferred to have been a result of orogenic collapse of the plateau during the late-Ottawan (Rivers, 2012). The aluminous rocks of this study come from the Manicouagan and Lac du Milieu areas of the mid-*P* hinterland in the central Grenville Province.

1.2.2.2 The Manicouagan and Lac du Milieu Areas

High-*P* and mid-*P* portions of the hinterland as well as the Orogenic Lid are well exposed in the vicinity of the reservoir, which surrounds the 214±1 million year old

Manicouagan impact crater (Figure 1.1; Hodych and Dunning, 1992). The mid-*P* hinterland south of Manicouagan has been described in Dunning and Indares (2010) and Indares and Moukhsil (2013), whereas its eastern extension in the Lac du Milieu area was documented by Moukhsil *et al.* (2012). The two areas display a wide variety of pre-Grenvillian plutonic and supracrustal rocks ranging in age from ~1.7 Ga to ~1.2 Ga, as well as Grenvillian age granite and anorthosite. The main lithologic associations of interest for this study are the Complexe de la Plus-Value (PLV), and the layered bimodal suite (LBS).

The PLV is a metasedimentary sequence that extends from the Lac du Milieu area, where it was first defined by Moukhsil *et al.*, (2012), to the southern Canyon domain of the Manicouagan area (Figure 1.1). The PLV is made up of quartzofeldspathic gneiss, metapelite, quartzite with minor marble and calcsilicate rocks, and is inferred to have been deposited at ~1.5 Ga on the margin of Laurentia (Moukhsil *et al.*, 2012; Lasalle *et al.*, 2013). Locally, the PLV in the Lac du Milieu area (PLV-LM) contains an association of rusty aluminous gneiss – fine-grained quartz-rich rocks with aluminous minerals and minor sulfides. This association is thought to be derived from pre-metamorphic hydrothermal alteration of the paragneisses (Letourneau, 2011).

The LBS, exposed in the central part of the Canyon domain (southern Manicouagan) is made up of mafic and felsic layers, inferred to represent remnants of a volcanic belt emplaced in an extensional crustal setting, at 1238 ± 13 Ma (Lasalle *et al.*, 2013; Indares and Moukhsil, 2013). Some felsic layers are white gneisses that locally

grade into aluminous varieties and garnetite, inferred to represent hydrothermally altered felsic volcanic rocks (Hindemith, 2013).

In addition, an association of aluminous rocks – fine-grained quartz-rich rocks with aluminous minerals – white felsic gneiss is also exposed amongst tonalitic migmatites of the Gabriel Complex, on the Gabriel Islands (Figure 1.1, eastern Manicouagan reservoir; Indares and Dunning, 2004; Strowbridge (2006). These gneisses will be referred to as the Gabriel aluminous gneisses (GAG). However, the age of the Gabriel Complex is unknown, and the affiliation of this association is uncertain (may be related to the PLV or LBS).

Mid-*P* granulite facies metamorphism in the Manicouagan and Lac du Milieu areas is manifested by the presence of G+Sill+Bi+Ksp±Pl+leucosome in aluminous rocks and Hb+Pl+G+Opx+Cpx±leucosome in mafic rocks. The age of this metamorphism is constrained between 1080 and 1040 Ma based on monazite and zircon U-Pb data from the Manicouagan area (Dunning and Indares, 2010; Lasalle *et al.*, 2014).

Previous work on mid-*P* aluminous rocks of the study areas includes: (1) documentation of the petrography and geochemistry of the aluminous – quartz-rich rock association of the PLV-LM by Letourneau (2011), and a preliminary metamorphic study by Patrick (2013); (2) investigations of the geology and metamorphism of the Gabriel Islands by Indares and Dunning (2004) and Strowbridge (2006); (3) a petrographic and geochemical study of the hydrothermally altered felsic rocks of the LBS by Hindemith (2013); and (4) the only modern published metamorphic study of aluminous rocks in the

Manicouagan area by Lasalle and Indares (2014). This latter study used phase equilibria modeling to constrain the P – T evolution of metapelites of the PLV and some hydrothermally altered felsic rocks of the LBS in the Manicouagan area. However, this was not successful in retrieving P – T paths for the hydrothermally altered rocks. Phase equilibrium modeling was also applied to some samples of the PLV-LM in the honours thesis by Patrick (2013) which is expanded in the present study.

1.2.3 Sample Choice and Locations

The aluminous gneisses of this study come from 3 locations: (a) the aluminous and quartz-rich rock association of the PLV from the Lac du Milieu area; (b) aluminous layers from the LBS in the Canyon domain; and (c) the aluminous and quartz-rich rock association of uncertain affiliation of the GAG. These samples were chosen because of their wide range of bulk compositions and textures, some of which are related to pre-metamorphic hydrothermal alteration of felsic protoliths, characteristics that make them unique since other phase equilibria modeling studies in the area used metapelitic rocks.

All samples were collected by Aphrodite Indares. Those from the PLV were collected with the help of Marie Letourneau during the summer of 2010 in the context of a field campaign by the Ministère de l'Énergie et des Ressources Naturelles (MERN), those from the GAG were collected during the 2000 field season, and those from the LBS during the 2003–04 and 2011 seasons. The locations of samples are indicated in Figure 1.1.

1.3 METHODS

This study integrates textural data and mineral chemistry with phase equilibria modeling. This involved the following methods, described in greater detail in the following section:

(i) polished thin sections were first examined under the optical microscope to identify mineral assemblages, to provide a first-order assessment of the textures, and document micro-textures such as those of former melt;

(ii) a scanning electron microscope with mineral liberation analysis software (SEM–MLA) was used to image the overall distribution of minerals and determine mineral proportions at the thin section scale;

(iii) where mineral chemistry was not already available from previous research, the major element chemical compositions of garnet, biotite, cordierite, K-feldspar and plagioclase, as well as pyrrhotite and ilmenite for the samples used for the Fe³⁺ study (Chapter 3), were acquired by electron probe microanalysis;

(iv) biotite from the samples used for the Fe³⁺ study was analysed by Mössbauer spectroscopy to determine the Fe³⁺ content; and

(v) phase equilibria diagrams (also known as *P–T* pseudosections) valid for specific bulk rock compositions of a selected sub-set of samples were calculated with the software Thermocalc (Powell and Holland, 1988).

1.3.1 Documentation of textures: optical microscope and scanning electron microscope

Optical petrography was used to document textures and identify minerals. This is a key traditional tool for visualizing the intimate relationships among minerals; however, it is limited by the fact that it is hard to see the overall texture of the slide because of the small field of view. Furthermore, there are many minerals that look very similar in thin section (ex. quartz, feldspars, cordierite), and although they can be identified one by one, it is hard to see their overall distribution and make an estimate of their proportions.

Back-scattered electron images and mineral maps for the thin sections were obtained with a FEI Quanta 600 scanning electron microscope (SEM) and JKTech Mineral Liberation Analysis (MLA) software at the Bruneau Center, Memorial University of Newfoundland. Thin sections were carbon coated before analysis. An accelerating voltage of 25 kV, a 10 nA beam current, a 50 μm step size, and a dwell time of 10 ms was used.

Phases were identified by comparing the energy dispersive spectroscopy (EDS) spectra obtained to those available in the software database. The modal proportion of each mineral was determined by identifying the mineral at each point for a step size of 50 μm (point-count estimation; Shaffer et al., 2008). A colour was selected for each mineral based on a preselected colour scheme, and a false colour mineral map was created with the software. Some mineral maps were obtained from previous work and included in the

present study: samples 10-AI-58-2A, 10-AI-58-3B1 and 10-AI-114-B1 from the PLV and all from the LBS (Letourneau, 2011; Hindemith, 2014; Lasalle and Indares, 2014).

1.3.2 Electron microprobe

Mineral chemistry for garnet, biotite, cordierite, K-feldspar, plagioclase, and in some samples, ilmenite and pyrrhotite, was acquired using an electron probe microanalyzer (EPMA). Many of the data were obtained from previous research, in which cases the instrument and operating conditions are available in Patrick (2013), Strowbridge (2006) and Hindemith (2014).

Mineral chemistry of ilmenite and pyrrhotite for the samples used in the Fe³⁺ study, and additional data for garnet, biotite, K-feldspar, plagioclase and cordierite in some samples from the GAG, were acquired on the JEOL JXA-8230 at Memorial University of Newfoundland. For all except ilmenite, a 15kV accelerating potential, a 20 nA beam current and a 3 micron beam diameter were used; a 100 nA beam current was used for ilmenite analyses.

1.3.3 Mössbauer spectroscopy

To determine the Fe³⁺/Fe_{tot} of biotite, samples were crushed, biotite grains were handpicked, and analyzed by Dr. Catherine McCammon at the Bayerisches Geoinstitut in Bayreuth, Germany for Mössbauer analysis. The grains were weighed to achieve a dimensionless thickness of 3 (7.4 mg Fe/cm²), soaked in benzophenone to reduce the

effects of preferred orientation, and loaded in a 12mm (or 6mm for sample 10-AI-20a) diameter holder. The spectra were recorded on a constant acceleration Mössbauer spectrometer with a nominal 1.85 GBq ^{57}Co source in a 6 μm Rh matrix at room temperature. In cases where there was asymmetry between the high- and low-velocity doublets (preferred orientation), the samples were rerun with the holder tilted at 54.7° to the γ -ray direction (Ericsson and Wäppling 1976). Values for $\text{Fe}^{3+}/\text{Fe}_{\text{tot}}$ were calculated based on relative area ratios.

1.3.4 Phase equilibria modeling

This part of the study involves the calculation of phase diagrams for a specific bulk composition using Thermocalc (Powell and Holland, 1988). The bulk composition representative of selected polished thin sections was calculated first.

1.3.4.1 Calculation of Bulk Composition

Thermocalc requires the bulk composition input as a molar percent of oxides. The bulk compositions used in this study were derived by combining the composition of each mineral (acquired with the EPMA as an average of multiple analyses in all textural settings and across zoned garnet) and the modal proportion of that mineral in the thin section as determined by the SEM–MLA. This was the method of choice because: (a) it gives bulk compositions representative of the investigated thin sections; and (b) it allows the calculation of a bulk H_2O on the basis of the major hydrous minerals, which is important for the location of the solidus in the pseudosections. We are only interested in

H₂O from biotite and cordierite and conventional methods can only give a loss on ignition value which may include H₂O from secondary alteration phases (Indares et al., 2008; Groppo et al., 2013).

First, the composition of each mineral was used to calculate the exact chemical formula using the method outlined in Nesse (2000), and then the proportion of each end member was determined by calculating the molar fractions. Next, the proportions of each end member of a mineral were multiplied by their molar volumes and summed to get the total molar volume for that phase. The modal percent from the SEM was then divided by this molar volume to give the number of moles of that phase, which was then normalized to the mole percent of all the phases. This number was multiplied by the proportion of each end member and by the number of moles in the structural formula for each oxide to yield the molar percent of each oxide. The individual oxides for each mineral were finally summed and normalized to 100% to give the bulk composition as a molar percent of oxides.

Because of the many possible substitutions in biotite, it was not possible to just use the end member proportions; in this case the cations (normalized to 11 oxygens) were multiplied by the mole percent. Additionally, since there is no way to measure H₂O in biotite directly, the approximate proportions of OH⁻ were estimated using the methods outlined in White et al. (2007) which relate Ti in biotite to H₂O content through the coupled substitution: $M1^{2+} + 2OH^- = Ti^{4+} + 2O^{2-}$. F⁻, which also occurs in the hydroxyl site was measured and accounted for in this calculation. For cordierite, it has been

assumed that there is no significant CO₂ within its framework channels for the calculation of H₂O using the methods of Harley *et al.* (2002).

1.3.4.2 Thermocalc

The program Thermocalc allows one to construct phase diagrams for a specific bulk composition based on what elements are defined as available in the system; these phase diagrams are also known as pseudosections (Holland and Powell, 1998). In this program, the user calculates selected field boundaries one line at a time by defining the variance, the minerals that are involved, the P - T range, and the P - T interval with which to calculate it. Each line represents the appearance or disappearance of a specific mineral and is defined by the mineral proportion reaching a zero value. The calculations are based on an internally consistent dataset of thermodynamic properties of pure phases and solid solution end members, and activity models for solid solutions are frequently updated.

For this study, the Na₂O–CaO–K₂O–FeO–MgO–Al₂O₃–SiO₂–H₂O–TiO₂–O (NCKFMASHTO) system was used, along with THERMOCALC 3.33 and the internally consistent dataset tcds55 (Powell and Holland, 1988), created November 22, 2003. The phases Liq–Q–G–Ksp–Pl–Sill–Bi–Cd–Mu–Ru–Ilm–Opx were considered in the calculations. The following a–x models were used: garnet (g: White *et al.*, 2007), biotite (bi: White *et al.*, 2007), cordierite (cd: Holland and Powell, 1998), muscovite (mu: Coggon and Holland, 2002), plagioclase and K-feldspar (pl, ksp: Holland and Powell,

2003), orthopyroxene (opx: White et al., 2002), ilmenite (ilm: White et al., 2000) and melt (liq: White et al., 2007).

A value for oxygen (O) is also required in the NCKFMASHTO system, which allows for consideration of part of the bulk Fe as Fe³⁺. For this, the software calculates the Fe³⁺ based on the relation: Fe₂O₃ = O+2FeO. Ideally, the amount of O should be based on the minerals considered that contain Fe³⁺ in this study: biotite and ilmenite (the pelitic garnet measured in this study does not contain significant ferric iron). In the first part of the thesis (Chapter 2), Fe³⁺ of biotite was unknown, so for consistency, a low value of oxygen equal to 0.05 was used for all pseudosections. This is a common value typically used in the literature for phase equilibrium calculations that assumes most Fe is Fe²⁺.

The second part of this thesis (Chapter 3) investigates the effect of changing the amount of Fe³⁺ in the pseudosection. Therefore, pseudosections were calculated with O values corresponding to: (1) the measured amounts of Fe³⁺ in the rock, and (2) assumed percentages of the total iron as ferric iron in biotite. The latter was determined with stoichiometry by assuming that 10, 15 or 20% of the iron in biotite is Fe³⁺ during the calculation of the bulk composition.

In orogenic environments, anatectic rocks commonly experience some melt loss. For several samples, additional pseudosections were calculated by reintegrating the presumed portion of the lost melt back into the bulk composition. This melt portion was estimated by obtaining the composition of the first infinitesimal amount of melt formed at

the solidus and changing the amount of melt until a water saturated solidus was reached (see Indares *et al.* 2008). Additionally, in Chapter 4, a second method of evaluating melt loss is evaluated where water is added to the bulk composition.

REFERENCES

- Beaumont, C. Jamieson, R.A., Nguyen, M.H. 2010. Models of large hot orogens containing a collage of reworked and accreted terranes. *Canadian Journal of Earth Sciences* 47, 485–515.
- Beaumont, C., Nguyen, M.H., Jamieson, R.A., Lee, B. 2006. Crustal flow modes in large hot orogens. *Geological Society of London Special Publication* 268, 91–145.
- Brown, M. 2007. Crustal melting and melt extraction, ascent and emplacement in orogens: mechanism and consequences. *Journal of Geological Society of London*, 164, 709–730.
- Cesare, B., Meli, S., Nodari, L., Russo, U., 2005. Fe³⁺ reduction during biotite melting in graphitic metapelites: another origin of CO₂ in granulites. *Contributions to Mineralogy and Petrology*. 149, 129-140.
- Coggon, R. and Holland, T. J. B., 2002. Mixing properties of phengitic micas and revised garnet-phengite thermobarometers. *Journal of Metamorphic Geology*, 20, 683–696.
- Diener, J.F.A. and Powell, R., 2010. Influence of ferric iron on the stability of mineral assemblages. *Journal of Metamorphic Geology*, 28, 599–613.
- Dunning G, and Indares, A., 2010. New insights on the 1.7–1.0 Ga crustal evolution of the central Grenville from the Manicouagan-Baie Comeau transect. *Precambrian Research*, 180, 204–226.
- Dyar, M.D., Lowe, E.W., Guidotti, C.V., Delaney, J.S.,. 2002. Fe³⁺ and Fe²⁺ partitioning among silicates in metapelites: A synchrotron micro-XANES study. *American Mineralogist* 87:514–52.
- Ericsson T, Wäppling R .1976. Texture effects in 3/3-1/2 Mössbauer spectra. *Journal of Physics (Paris) Colloque*, C6, 719-723.

- Gower, C. F. and Krogh, T. E. 2002. A U–Pb geochronological review of the Proterozoic history of the eastern Grenville Province. *Canadian Journal of Earth Sciences* 39, 795–829.
- Groppo, C., Rolfo, F., Mosca, P. 2013. The cordierite-bearing anatectic rocks of the higher Himalayan crystallines (eastern Nepal): low-pressure anatexis, melt productivity, melt loss and the preservation of cordierite. *Journal of Metamorphic Geology*. 31,187-204.
- Guilmette, C., Indares, A., Hébert, R. 2011. High-pressure anatectic paragneisses from the Namche Barwa, Eastern Himalayan Syntaxis: Textural evidence for partial melting, phase equilibria modeling and tectonic implications. *Lithos*. 124, 66-81.
- Harley, S. L., Thompson, P. P., Hensen, B. J., Buick, I. S. 2002. Cordierite as a sensor of fluid conditions in high-grade metamorphism and crustal anatexis. *Journal of Metamorphic Geology*, 20 (1), 71-86.
- Hindemith, M. A., 2013. Petrography and geochemistry of hydrothermally altered volcanic rocks metamorphosed at granulite-facies conditions: an example from the central Grenville Province. Masters Thesis. Memorial University of Newfoundland. 131 Pages.
- Hodych, J.P., and Dunning, G.R. 1992. Did the Manicouagan impact trigger end-of-Triassic mass extinction? *Geology*, 20, 51–54.
- Holland, T. J. B. and Powell, R., 1998. An internally-consistent thermodynamic data set for phases of petrological interest. *Journal of Metamorphic Geology*, 16, 309–343.
- Holland, T. J. B. and Powell, R., 2003. Activity-composition relations for phases in petrological calculations: an asymmetric multicomponent formulation. *Contributions to Mineralogy and Petrology*, 145, 492–501.
- Holness, M.B., Cesare, B., Sawyer E.W. 2011. Melted Rocks under the Microscope: Microstructures and Their Interpretation. *Elements*, 7, 247-252.
- Indares, A. and Moukhsil, A., 2013. Geon 12 crustal extension in the central Grenville Province, implications for the orogenic architecture and potential influence on the emplacement of anorthosites. *Canadian Journal of Earth Sciences*, 50, 955-966.
- Indares, A., and Dunning, G. 2004. Crustal architecture above the high-pressure belt of the Grenville Province in the Manicouagan area: new structural, petrologic and U–Pb age constraints. *Precambrian Research*, 130, 199-208.
- Indares, A.D., White, R.W., Powell, R., 2008. Phase equilibria modelling of kyanite bearing anatectic paragneisses from the central Grenville Province. *Journal of Metamorphic Geology*, 26, 815–836.

- Jamieson, R.A. and Beaumont, C., 2011. Coeval thrusting and extension during post-convergent ductile flow - implications for exhumation of high-grade metamorphic rocks. *Journal of Metamorphic Geology*, 29, 33–51.
- Jamieson, R.A., Beaumont, C., Nguyen, M.H., Culshaw, N.G., 2007. Synconvergent ductile flow in variable-strength continental crust: Numerical models with application to the western Grenville orogen. *Tectonics*, 26, 1–23.
- Jamieson, R.A., Beaumont, C., Warren, C.J., Nguyen, M.H., 2010. The Grenville Orogen explained? Applications and limitations of integrating numerical models with geological and geophysical data. In: *Lithoprobe - parameters, processes and the evolution of a continent* (Lithoprobe Synthesis Volume II, eds Clowes, R M., and Skulski, T.). *Canadian Journal of Earth Sciences*, 47, 517–539.
- Lasalle, S., Dunning, G., Indares, A., 2014. In situ LA–ICP–MS dating of monazite from aluminous gneisses: insights on the tectono-metamorphic history of a granulite-facies domain in the central Grenville Province. *Canadian Journal of Earth Sciences*, 51, 558–572.
- Lasalle, S., Fisher, C.M., Indares, A., Dunning, G., 2013. Contrasting types of Grenvillian granulite facies aluminous gneisses: insights on protoliths and metamorphic events from zircon morphologies and ages. *Precambrian Research*, 228, 117–130.
- Lasalle, S. and Indares, A. 2014. Anatectic record and contrasting P – T paths of aluminous gneisses from the central Grenville Province. *Journal of Metamorphic Geology*, 32, 627–646.
- Letourneau, M. 2011. Anatectic aluminous gneisses from the Mesoproterozoic Complexe de la Plus-Value, Grenville Province, Quebec. Memorial University: Honours thesis.
- Moukhsil, A., Solgadi, F., Lacoste, P., Gagnon, M., David, J., 2012. Geologie de la region du lac du Milieu. Geologie Quebec.
- Nesse, William D. 2000. Introduction To Mineralogy. United States: Oxford University Press: New York, NY, United States.
- Patrick, M. E., 2013 Metamorphic investigation of anatectic aluminous gneisses from the Complexe de la Plus-Value, Grenville Province. Honours thesis, Memorial University of Newfoundland.
- Platten, I. M., 1983. Partial melting of semipelite and the development of marginal breccias around a late Caledonian minor intrusion in the Gremplan highlands of Scotland. *Geological Magazine*, 120, 37–49.

- Powell, R., Holland, T.J.B. 1988 An internally consistent thermodynamic dataset with uncertainties and correlations: 3. Applications to geobarometry, worked examples and a computer program. *Journal of Metamorphic Geology*, 6, 173-204.
- Powell, R., Holland, T.J.B. 2008. On thermobarometry. *Journal of Metamorphic Geology* 26, 155-179.
- Rivers, T., 2008 Assembly and preservation of lower, mid and upper orogenic crust in the Grenville Province – Implications for the evolution of large hot long-duration orogens. *Precambrian Research*, 167, 237-259.
- Rivers, T., 2012. Upper-crustal orogenic lid and mid-crustal core complexes: signature of a collapsed orogenic plateau in the hinterland of the Grenville Province. *Canadian Journal of Earth Sciences*, 49, 1–42.
- Rivers T, Culshaw N, Hynes A, Indares A, Jamieson R, Martignole J. 2012. The Grenville Orogen – A post-LITHOPROBE perspective. Chapter 3 In *Tectonic Styles in Canada: The LITHOPROBE Perspective*. (eds JA Percival, FA Cook, and RM Clowes) *Geological Association of Canada, Special Paper* 49, 97–236.
- Rivers, T. and Corrigan, D. 2000. Convergent margin on southeastern Laurentia during the Mesoproterozoic: tectonic implications. *Canadian Journal of Earth Sciences* 37, 359–383.
- Rivers, T., Martignole, J., Gower, C.F., Davidson, A., 1989. New tectonic divisions of the Grenville Province, Southeast Canadian Shield. *Tectonics*, 8, 63-84.
- Sawyer, E. W., 1999. Criteria for the recognition of partial melting. *Physics and Chemistry of the Earth*, 24, 269–279.
- Sawyer, Edward W. 2008. Atlas Of Migmatites. *Canadian Mineralogist*. Special Publication 9.
- Shaffer, M., Gu, Y., Rohde, M. 2008. Practical Applications for the Silicon Drift X-ray Detector in SEM-Platformed Image Analysis: The Bruker-MLA in Practice. In *SME Annual Meeting 2007 and CMS 109th National Western Conference 2007 The Power of Mining: Energy's Influence*, Denver, CO, U.S.A., 25-28 February, 2007, 1(Preprint 07-029), 1-6.
- Spear, Frank S. 1993. *Metamorphic Phase Equilibria And Pressure-Temperature-Time Paths Monograph Series*. United States: Mineralogical Society of America: Washington, DC, United States, 1993. 799 Pages.
- Spear, F.S., Kohn, M.J., Cheney, J.T., 1999. P–T paths from anatectic pelites. *Contributions to Mineralogy and Petrology*, 134, 17–32.

- Strowbridge, S., 2006. Metamorphic evolution of anatectic metapelites from the Gabriel high strain zone, Grenville Province. Masters Thesis. Memorial University of Newfoundland.
- Vernon, R. H. and Collins, W. J., 1988. Igneous microstructures in migmatites. *Geology*, 16, 1126–1129.
- White, R.W. and Powell, R. 2002. Melt loss and the preservation of granulite facies assemblages. *J. Metamorphic Geology*, 20, 621-632.
- White, R. W., Powell, R., Clarke, G. L., 2002. The interpretation of reaction textures in Fe-rich metapelitic granulites of the Musgrave Block, central Australia: constraints from mineral equilibria calculations in the system $K_2O-FeO-MgO-Al_2O_3-SiO_2-H_2O-TiO_2-Fe_2O_3$. *Journal of Metamorphic Geology*, 20, 621–632.
- White, R.W., Powell, R., Holland, T.J.B., 2007. Progress relating to calculation of partial melting equilibria for metapelites. *Journal of Metamorphic Geology*, 25, 511–527.
- White, R. W., Powell, R., Holland, T. J. B., Worley, B. A., 2000. The effect of TiO_2 and Fe_2O_3 on metapelitic assemblages at greenschist and amphibolite facies conditions: mineral equilibria calculations in the system $K_2O-FeO-MgO-Al_2O_3-SiO_2-H_2O-TiO_2-Fe_2O_3$. *Journal of Metamorphic Geology*, 18, 497–511.

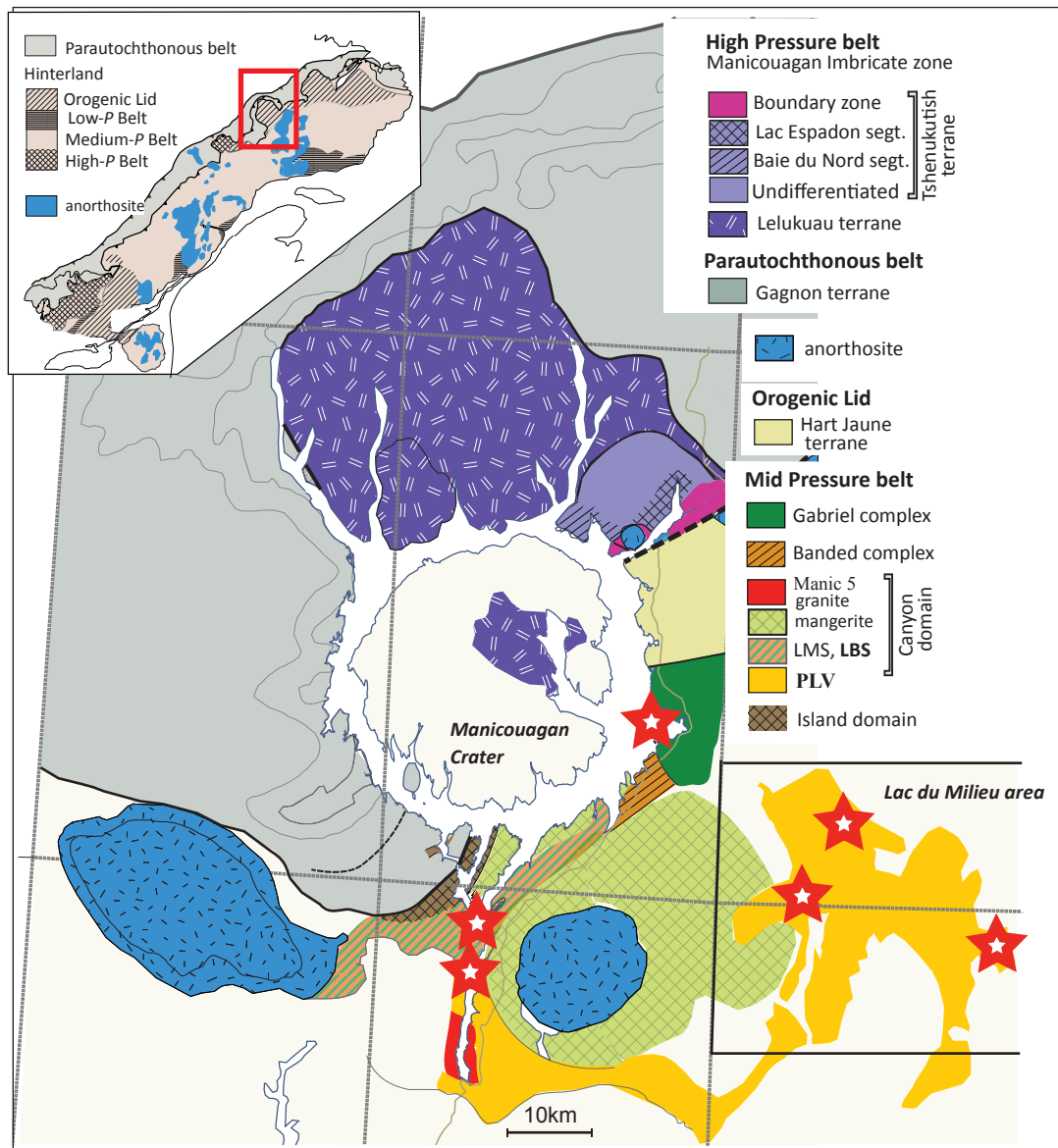


Figure 1.1. Simplified map of the Manicouagan and lac du Milieu areas showing the distribution of the sampled locations (in stars). Inset: location of the study areas in the Grenville Province.

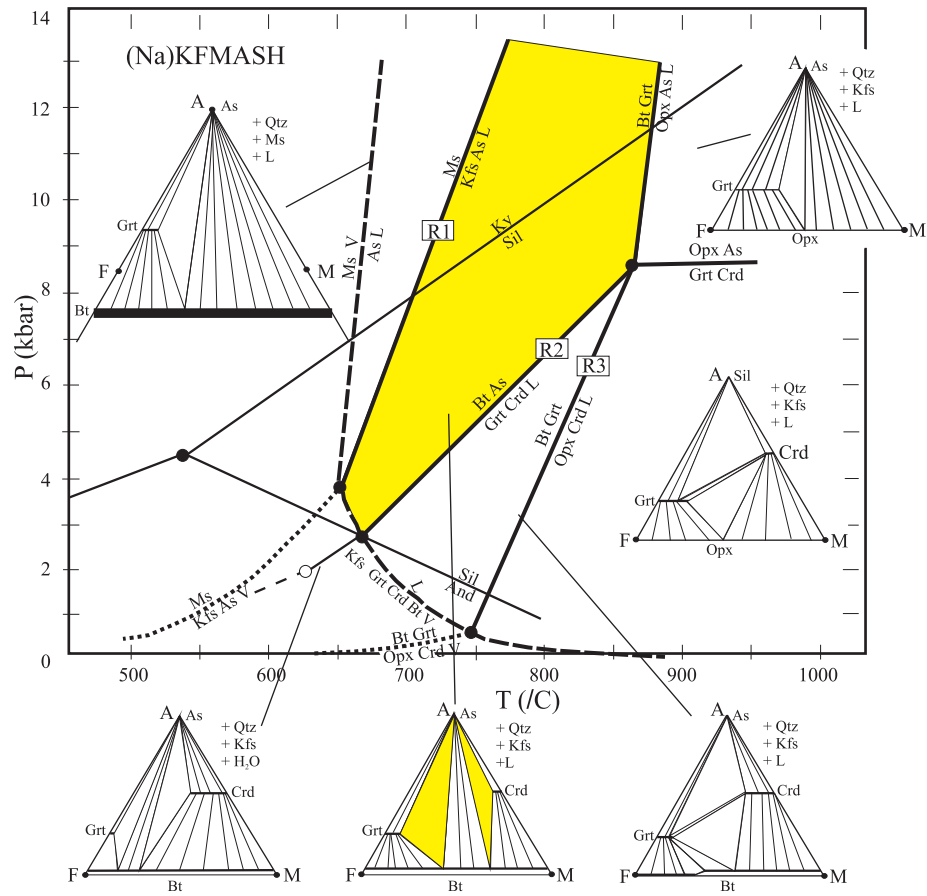


Figure 1.2. Petrogenetic grid showing the dehydration melting reactions of micas. In yellow: field of interest (modified after Spear et al., 1999).

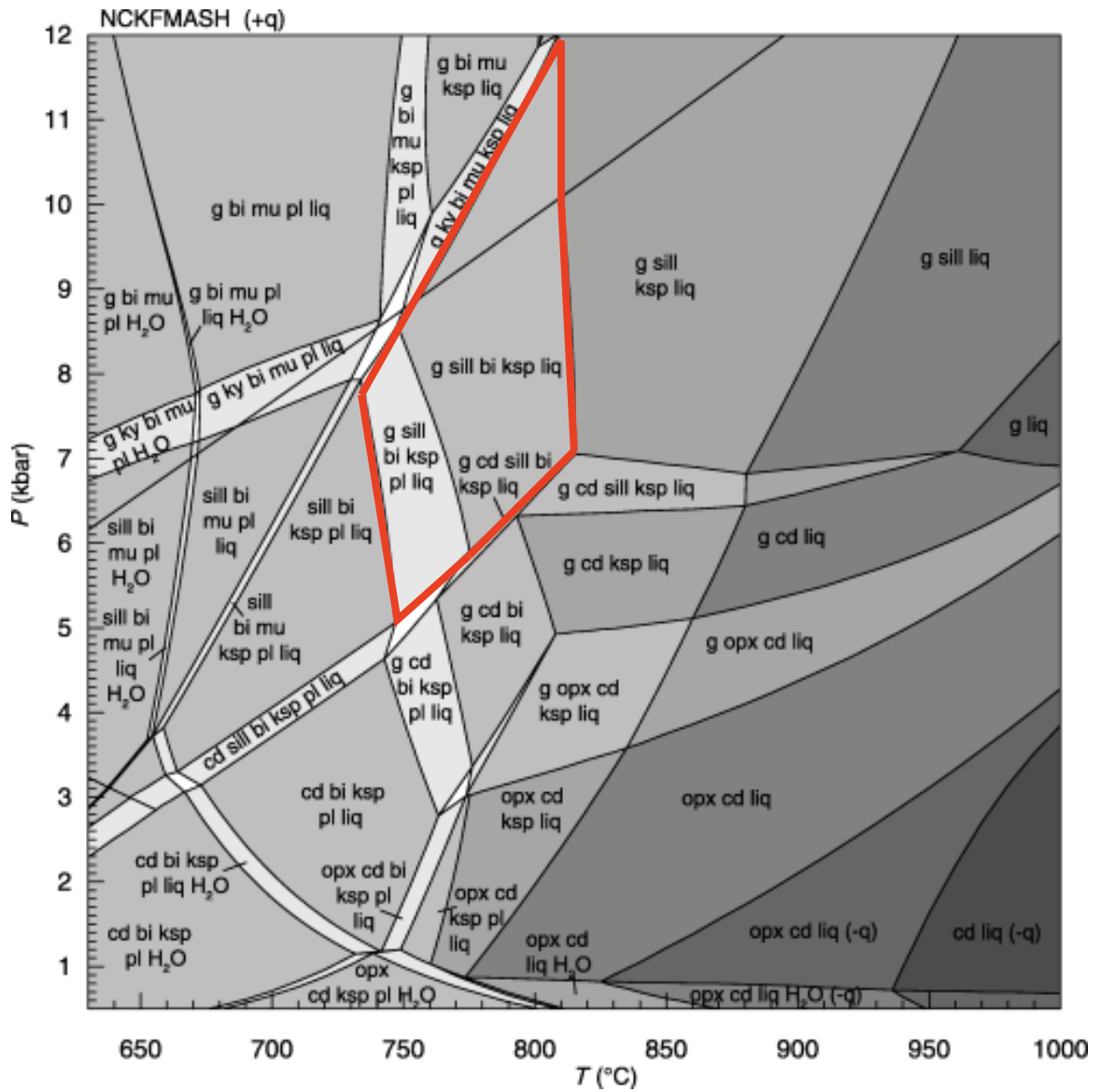


Figure 1.3. Example of a simple metapelite pseudosection in the NCKFMASH system. The field of interest (Liq+G+Bi+Sill+Ksp+Q+/-Pl) is outlined in red (modified after White et al., 2007). Increasing degree of shading corresponds to increasing variance.

CHAPTER 2: PETROGRAPHY AND PHASE EQUILIBRIA MODELING OF MID-*P* ALUMINOUS GNEISSES DERIVED FROM HYDROTHERMALLY ALTERED PROTOLITHS, GRENVILLE PROVINCE, CANADA

ABSTRACT

A large portion of the hinterland of the central Grenville Province is characterized by mid-pressure granulite-facies metamorphism. In the Manicouagan – Lac du Milieu region of Quebec, aluminous gneisses derived from hydrothermally altered felsic protoliths provide a record of anatectic processes and of the pressure-temperature (P – T) evolution during orogenesis. Samples of these gneisses, collected in areas separated by several tens of kilometers, contain the mineral assemblage garnet + biotite + quartz + K-feldspar ± plagioclase ± sillimanite, with retrograde cordierite in some, and most of them display textural evidence of partial melting. However, they have a wide range of bulk compositions and textures, and may be grouped in two types: sillimanite-rich rocks, with a high alumina index in AFM space and sillimanite-poor rocks with low alumina index and in which sillimanite is not part of the peak assemblage.

Phase equilibria modeling with Thermocalc constrained the P – T field of the peak mineral assemblage(s) at 800–900°C and 6–11 kbar, with melt solidification in the range of 800–865°C and 6–8 kbar. The presence of sillimanite inclusions in garnet, and the scarcity of retrograde cordierite is consistent with moderate dP/dT gradient ‘hairpin’ P – T paths. The data suggest that this part of the mid- P hinterland in the central Grenville experienced a rather uniform metamorphic evolution, with large temperature variations

relative to pressure. The high metamorphic temperatures recorded by these rocks are consistent with the proposal that the Grenville is a large hot orogen.

2.1 INTRODUCTION

High-temperature metamorphic processes play a major role in the tectonic evolution of continental crust in mountain belts, and most particularly in “large hot orogens” (Beaumont et al., 2006) where the middle to lower crust experiences partial melting, melt transfer and ductile rheology (Brown, 2007). Formerly deep crust is widely exposed in ancient orogens by late tectonism and erosion. A prime example of such an orogen is the Grenville Province, which was active between 1.09 and 0.98 billion years ago (Rivers et al, 2012; Rivers, 2008) along the eastern part of North America. Large portions of the hinterland of the central Grenville Province reached mid-pressure granulite-facies metamorphic conditions, and constitute prime material for the investigation of high temperature metamorphic and anatexis processes.

Aluminous rocks are particularly useful for metamorphic studies involving anatexis because in addition to their mineral assemblages being sensitive to changes in pressure (P) and temperature (T), they are also the most fertile with respect to melting due to the presence of micas (Spear et al., 1999). Most studies of aluminous systems in the literature have focused on metasedimentary rocks (ex. metapelites and metagreywakes). However, aluminous bulk chemistries may also be derived from hydrothermal alteration processes of a wide range of felsic protoliths (Bonnet and

Corriveau, 2007), in which case they may be significantly different from those of typical metasedimentary rocks (Lasalle and Indares, 2014).

The aim of this paper is to evaluate the partial melting history and P - T paths followed by mid-crustal anatectic aluminous rocks from the hinterland of the central Grenville Province. This study focuses on rocks that have acquired (to some extent) their aluminous character by pre-metamorphic hydrothermal alteration of felsic protoliths, which has resulted in a wide range of compositions and textures, and in some cases, atypical chemistry. The general approach used involves documentation of textures, mineral chemistry and phase equilibria modeling.

2.2 GEOLOGICAL CONTEXT

The Grenville Province mainly consists of arc terranes developed along the southeast margin of proto-Laurentia between 1700 and 1230 Ma (Gower and Krogh, 2002; Rivers and Corrigan, 2000) that were subjected to a continental collision between 1090 and 980 Ma (Grenvillian Orogeny; see review in Rivers, 2008). Large parts of the orogenic hinterland were metamorphosed under mid- P (and locally high- P) granulite-facies conditions during the Ottawa phase of the Grenvillian Orogeny (1090–1020 Ma), resulting in partial melting, high crustal ductility and the development of an orogenic plateau (Rivers, 2008). These parts are juxtaposed with domains that experienced lower grades of metamorphism (low- P segment and Orogenic Lid; Rivers, 2012), in a configuration that is interpreted to be the result of orogenic collapse during the late-

Ottawan (Rivers, 2012). The aluminous rocks of this study come from the Manicouagan and Lac du Milieu areas of the mid-*P* hinterland in the central Grenville Province.

2.2.1 The Manicouagan and Lac du Milieu areas

The mid-*P* hinterland south of Manicouagan (Figure 2.1) has been described by Dunning and Indares (2010) and Indares and Moukhsil (2013), whereas its eastern extension in the Lac du Milieu area was documented by Moukhsil et al. (2012). The two areas display a wide variety of pre-Grenvillian plutonic and supracrustal rocks ranging in age from ~1.7 Ga to ~1.2 Ga, as well as Grenvillian age granite and anorthosite. The main lithologic associations of interest for this study are the Complexe de la Plus-Value (PLV), and the layered bimodal suite (LBS).

The PLV is a metasedimentary sequence that extends from the Lac du Milieu area, where it was first defined by Moukhsil *et al.*, (2012), to the southern Canyon domain of the Manicouagan area (Figure 2.1). It is made up of quartzofeldspathic gneiss, metapelite, quartzite with minor marble and calcsilicate rocks, and is inferred to have been deposited at ~1.5 Ga on the margin of Laurentia (Moukhsil *et al.*, 2012; Lasalle *et al.*, 2013). Locally, the PLV in the Lac du Milieu area (PLV-LM) contains an association of rusty-weathering aluminous gneiss – fine-grained quartz-rich rocks with aluminous minerals. This association is interpreted to be derived from pre-metamorphic hydrothermal alteration of the paragneisses (Letourneau, 2011).

The LBS, exposed in the central part of the Canyon domain (southern Manicouagan; Figure 2.1), is made up of mafic and felsic layers, inferred to represent

remnants of a volcanic belt emplaced in an extensional crustal setting (Indares and Moukhsil, 2013), at 1238 ± 13 Ma (Lasalle *et al.*, 2013). Some felsic layers are white gneisses that locally grade into aluminous varieties and garnetite, inferred to represent hydrothermally altered felsic volcanic rocks (Hindemith, 2013).

In addition, an association of aluminous rocks – fine-grained quartz-rich rocks with aluminous minerals – white felsic gneiss is also exposed amongst tonalitic migmatites of the Gabriel complex, on the Gabriel Islands (eastern Manicouagan reservoir; Indares and Dunning, 2004; Strowbridge, 2006; Figure 2.1). However, the age of the Gabriel Complex is unknown, and the affiliation of this association, which will be referred to here as Gabriel aluminous gneiss (GAG), is uncertain.

Mid-*P* granulite facies metamorphism in the Manicouagan and Lac du Milieu areas is manifested by the presence of garnet + sillimanite + biotite + K-feldspar + plagioclase + leucosome in aluminous rocks and hornblende + plagioclase + garnet + orthopyroxene + clinopyroxene ± leucosome in mafic rocks. The age of metamorphism is constrained between 1080 and 1040 Ma based on monazite and zircon data from the Manicouagan area (Dunning and Indares, 2010; Lasalle *et al.*, 2014).

Previous work on mid-*P* aluminous rocks of the study areas has focused on: (1) the petrography and geochemistry of hydrothermally altered zones of the PLV-LM (Letourneau, 2011), and of the LBS in Canyon domain (Hindemith, 2013), and (2) the geology and metamorphism of the Gabriel Islands (Indares and Dunning, 2004; Strowbridge (2006). In addition, a preliminary metamorphic investigation of the samples

used by Letourneau in the PLV-LM was done by Patrick (2013) and the only modern published metamorphic study of aluminous rocks in the Manicouagan area was done by Lasalle and Indares (2014). This study used phase equilibria modeling to constrain the P – T evolution of metapelites of the PLV and some hydrothermally altered felsic rocks of the LBS in the Manicouagan area. However, it was not successful in retrieving P – T paths for the hydrothermally altered rocks.

The aluminous gneisses of this study come from 3 units, in distinct locations, separated by a few 10s of kilometers (Figure 2.1): (a) the PLV-LM (aluminous and quartz-rich rock association); (b) the LBS in the Canyon domain; and (c) the GAG. These samples were chosen based on their similarity of mineral assemblages in a wide range of bulk compositions and textures, and also because the P – T evolution of some of these areas remains unconstrained and phase equilibria modeling studies involving hydrothermally altered rocks are rare.

2.3 TEXTURES

The samples from all three locations (5 from the PLV-LM, 4 from the LBS, and 7 from the GAG) have the mineral assemblage $G+Bi+Q+Ksp\pm Sill\pm Pl\pm Cd$ with a wide range of textures and mineral proportions (mineral abbreviations are listed on page xii). The general distribution of phases in the investigated samples was imaged by means of false color mineral maps (Figures 2.2–2.4). These maps were acquired with a FEI Quanta 600 scanning electron microscope (SEM) and JKTech Mineral Liberation Analysis

(MLA) software at the Bruneau Center, Memorial University of Newfoundland.

Analytical conditions included accelerating voltage of 25 kV, a 10 nA beam current, and a dwell time of 10 ms. SEM–MLA mineral maps are only shown for the most characteristic samples that have distinctive overall textures; additional maps are available in Appendix A. This method also produced mineral proportions, listed in Table 2.1.

Detailed key microtextures observed by optical microscopy are shown in Figure 2.5.

Most samples exhibit compositional layering with alternating aluminous (rich in garnet, biotite and sillimanite) and quartzofeldspathic layers, and some from the LBS and GAG have aluminous nodules (Figures 2.3–2.4). Foliation is common, and is defined by biotite, and in some cases sillimanite or elongated garnet. However, the quartz-rich rocks from the PLV-LM and GAG are fine-grained and massive. In terms of the proportion and mode of occurrence of Al-silicate, the samples can be classified as: (a) sillimanite-rich, where sillimanite is part of the main assemblage, and occurs in large proportions relative to the total aluminous minerals (in the PLV-LM and some of the GAG samples; Table 2.1); and (b) sillimanite-poor, where sillimanite is restricted within aluminous nodules, patches and/or inclusions in garnet (samples from LBS and some from the GAG).

2.3.1 Samples from the PLV-LM

The samples from the PLV in the Lac du Milieu area mainly consist of G+Bi+Q+Ksp+Sill+Pl±Cd (Table 2.1 and Figure 2.2), where cordierite (or pinnite) is present in all except 10-AI-20A. They belong to the sillimanite-rich group but the ratio of

quartzofeldspathic to aluminous minerals varies greatly between samples (Table 2.1). For example, in 10-AI-58-3B1 the quartzofeldspathic minerals (22.35%) are mainly concentrated in veins, whereas in 10-AI-58-2a, the most quartz-rich rock, these make up the majority (81.65%). These two rocks represent distinct aluminum-rich and quartz-rich layers of the same outcrop. A quartzofeldspathic vein (possibly syn-metamorphic) with alteration along the selvages crosscuts through 10-AI-58-3B1 and 10-AI-58-2a.

Garnet ranges from porphyroblastic to fine-grained. It has an ameboidal shape in the fine-grained samples 10-AI-58-2a and 10-AI-108F, whereas in 10-AI-20A, 10-AI-114-B1 and 10-AI-58-3B1 it occurs as stringers, elongated aggregates of framboidal grains, and flattened bricks, respectively. In the later samples, it is also corroded by Bi+Sill±Pl, or cordierite. Garnet commonly contains inclusions of sillimanite, biotite and quartzofeldspathic minerals, or polyminerallic inclusions of these minerals rimmed by feldspar. Sillimanite grains in the matrix are prismatic whereas those included within garnet are acicular, and in cases where garnet is elongate, the two are parallel. Biotite commonly forms symplectites with quartz, and locally feldspars, in the vicinity of garnet (Figure 2.5a).

Cordierite occurs as elongated interstitial patches within the matrix in 10-AI-58-3B1 and 10-AI-58-2A (Figure 2.5b), which corrode sillimanite and garnet (Figure 2.5c). In addition, in 10-AI-108-F, cordierite pseudomorphs sillimanite prisms (Figure 2.5d). The matrix of this sample also contains rounded, ameboid or oddly shaped quartz grains

rimmed by thin films of feldspar (Figure 2.5e). Plagioclase is restricted to sites of garnet corrosion, and around K-feldspar in 10-AI-114-B1 and 10-AI-58-3B1.

2.3.2 Samples from the LBS

The selected samples from the LBS have the assemblage $G+Bi+Pl+Q+Ksp\pm Sill$ and belong to the sillimanite-poor group (Table 2.1). They display a foliation defined by biotite within the matrix, elongated aluminous nodules, quartz ribbons or elongated aggregates of quartz or feldspars (Figure 2.3).

In all the samples except 216a, which is described separately below, the aluminous minerals biotite, garnet and sillimanite, occur to a large extent in nodules or aggregates. Although biotite is also distributed throughout the matrix, sillimanite is restricted to the aluminous nodules/aggregates, and is absent altogether in 333-2-03. This distribution of minerals is most prominent in 354-2-03, where the entire sample is zoned from the least to the most aluminous minerals, towards the interior of the nodule. That is quartz→K-feldspar→plagioclase in the matrix, and biotite→garnet→sillimanite→spinel→corundum within the aluminous nodules (Figure 2.3; see also Hindemith, 2013). Garnet is porphyroblastic, elongated, highly corroded and contains both monomineralic (quartz, sillimanite, biotite) and polymineralic inclusions where biotite and rounded quartz grains are surrounded by thin films of feldspars (Figure 2.5f–g). Sample 333-2-03 also has a second type of garnet which is equant, and has a “swiss cheese” appearance with inclusions that are made up of predominantly quartz.

Sample 216a consists of garnet of various sizes in a layered quartzofeldspathic matrix, and has very small amounts of biotite and sillimanite. Biotite is mostly concentrated around the largest garnet porphyroblast. Sillimanite occurs in the matrix, where it is mantled by plagioclase in long aggregates, and also occurs as an inclusion in garnet, and in one instance, garnet pseudomorphs sillimanite in a long aluminous seam.

Quartzofeldspathic minerals in all samples occur in a wide range of sizes and forms, exhibit lobate to irregular boundaries, and commonly from triple junctions. Quartz forms ribbons that are partially recrystallized and resorbed, as well as patches of mortar texture in some samples, and symplectites with biotite.

2.3.3 Samples from the GAG

The samples from the GAG mainly consist of $G+Bi+Q+Ksp\pm Pl\pm Cd\pm Sill$, with cordierite only present in HJ-35a and HJ-57-C2 (Table 2.1 and Figure 2.4). They belong to the sillimanite-rich group, except for 10-AI-76 and HJ-74, in which sillimanite is restricted to inclusions in garnet or is absent altogether. Sample HJ-57-C2 is fine-grained, relatively homogeneous and quartz-dominated, whereas all others are medium- to coarse-grained and contain large proportions of aluminous minerals. All except 10-AI-76 and HJ-35a are compositionally banded into layers that are quartzofeldspathic-dominated or aluminous-dominated, and all except HJ-57-C2 have a weak to moderate foliation defined by biotite \pm sillimanite \pm elongated smaller garnet (Figure 2.4).

Most samples (except HJ-57-c2 and HJ-74) have two types of garnet: (1) porphyroblastic, inclusion-bearing, and (2) smaller, elongated inclusion-free garnet. Type

1 garnet is corroded by $\text{Bi} \pm \text{Sill} \pm \text{Pl} \pm \text{Cd}$, and inclusions consist of quartzofeldspathic minerals, biotite and acicular sillimanite, or polymineralic inclusions of any combination of these. There is an aluminous nodule in 10-AI-76, containing inclusions of spinel, corundum and sillimanite, and is rimmed by biotite and mantled by plagioclase (Figure 2.4). Sillimanite in the matrix is prismatic. Cordierite, where present, is variably altered to pinnite and occurs as wisps in the matrix, as well as associated with garnet (Figure 2.5h). Additionally, pinnite-altered cordierite encloses quartzofeldspathic minerals in HJ-57-C2 (Figure 2.5i). Quartz is variably recrystallized, and forms symplectites with biotite, mainly in the areas surrounding garnet. Large plagioclase porphyroblasts in HJ-57B contain inclusions of biotite.

2.3.4 Interpretation of Textures

The dominant mineral assemblage and the textures observed in the rocks of the three locations, are consistent with the biotite dehydration reaction: $\text{Bi} + \text{Sill} + \text{Q} \pm \text{Pl} \rightarrow \text{Melt} + \text{G} + \text{Ksp}$. Acicular sillimanite inclusions within elongate garnet, and relict reactants surrounded by former melt films and other melt textures (to be discussed below) are evidence of this reaction in the forward direction. Furthermore, corrosion of garnet by $\text{Bi} \pm \text{Sill} \pm \text{Pl} \pm \text{Q}$ is indicative of this reaction in reverse.

Cordierite is interpreted as retrograde in samples 10-AI-58-3B1 and 10-AI-108F from the PLV-LM because it corrodes garnet and in some cases, sillimanite, or pseudomorphs sillimanite prisms. In 10-AI-58-2A from the PLV-LM, as well as HJ-57-

C2 and HJ-35a from the GAG, it is not conclusive whether cordierite is part of the peak assemblage or a retrograde phase because it is distributed throughout the fine-grained matrix and lacks reaction textures. Furthermore, the fine-grained nature of the first two samples makes them prone to extensive re-equilibration, therefore, any retrograde reaction textures in them may have been obliterated

Samples from all locations display one or more textures that are interpreted as former melt, including: (1) pseudomorphed multi-mineral melt pools enclosed by or partially protected within garnet porphyroblasts (Figures 2.5f-g), (2) biotite-quartz symplectites (Figure 2.5a), (3) straight edges of garnet grown into melt that has pseudomorphed into cordierite (Figure 2.5c), or (4) rounded or amoeboid shaped quartz grains surrounded thin film of feldspars within garnet or the matrix (Figure 2.5e). For the interpretation of such textures, see also Vernon and Collins (1988) and Sawyer (1999). A quartzofeldspathic vein with alteration along the selvages crosscuts 10-AI-58-3B1 and 10-AI-58-2a, also suggesting melt movement; however, it is not possible to determine how far this melt has moved.

Some samples also have micro textural evidence of hydrothermal alteration prior to metamorphism, to the protolith. The aluminous seams and nodules from both the GAG and the LBS are interpreted to be a relict hydrothermal alteration texture where the original high-alumina minerals were replaced during metamorphism (Hindemith 2013).

2.4 MINERAL CHEMISTRY

Most mineral compositions of the rocks used in this study were compiled from previous work (GAG: Strowbridge, 2006; LBS: Hindemith, 2013; and 216a: Lasalle and Indares, 2014; PLV-LM: Patrick, 2013). Additional data from the GAG were acquired on the five wavelength dispersive spectrometer (WDS) JEOL JXA-8230 at Memorial University of Newfoundland, using a 15kV accelerating potential, a 20 nA beam current and a 3 micron beam (raw data and standards used are available in Appendix B).

The compositions of garnet, biotite, cordierite, plagioclase and K-feldspar were used in order to: (i) calculate the bulk compositions of the thin sections by combining the mineral chemistry with the modal proportions of each mineral; and (ii) calculate lines of equal composition (isopleths) on the phase equilibria diagrams for use to constrain P - T paths.

2.4.1 Garnet

For each sample, compositional ranges of garnet in terms of end members and $x(\text{Fe})=\text{Fe}/(\text{Fe}+\text{Mg})$ are listed in Table 2.2. In most cases, garnet is almandine-rich, with moderate pyrope, and minor grossular and spessartine contents:

- (a) $[\text{Alm}_{64-77}\text{Prp}_{17-32}\text{Grs}_{0-3}\text{Sp}_{1-5}]$, with $x(\text{Fe})=0.64-0.77$ in the PLV-LM;
- (b) $[\text{Alm}_{51-74}\text{Prp}_{15-46}\text{Grs}_{0-4}\text{Sp}_{0-5}]$, with $x(\text{Fe})=0.53-0.83$ in the LBS; and
- (c) $[\text{Alm}_{49-66}\text{Prp}_{20-40}\text{Grs}_{1-13}\text{Sp}_{1-5}]$, with $x(\text{Fe})=0.31-0.76$ in the GAG.

One exception to these ranges is in sample HJ-57-C2 (GAG) where spessartine makes up 26–34% of garnet, and almandine comprises a mere 21–23%. Generally, samples from

the GAG have lower almandine contents, and the widest range of grossular contents. For all areas, there is a slight increase in almandine and spessartine, and decrease in pyrope at the rim of garnet porphyroblasts, whereas small grains do not display such zoning (Strowbridge, 2006; Hindemith, 2013; Patrick, 2013).

2.4.2 Biotite and Cordierite

Compositional ranges of biotite in terms of Ti, Al^{VI}, F and $x(\text{Fe})=\text{Fe}/(\text{Fe}+\text{Mg})$ are listed in Table 2.3. The $x(\text{Fe})$ is 0.30–0.48 in biotite from PLV-LM and LBS, and 0.17–0.40 in that of GAG, with values as low as 0.06 in sample HJ-57-C2. Ti and Al^{VI} contents cover wide ranges, in some cases even at the sample scale where Al^{VI} is negatively correlated with Ti. Biotite from the LBS has higher Ti and that of GAG has significantly lower Al^{VI} compared with other locations. Biotite grains in contact with garnet have slightly lower $x(\text{Fe})$ than those from the matrix. Cordierite is present in three samples from the PLV-LM, and two from the GAG. It is Mg-rich, with an $x(\text{Fe})$ of 0.22–0.27 in the PLV-LM and 0.05–0.13 in the GAG.

2.4.3 Feldspars

Compositional ranges of plagioclase and K-feldspar in terms of end members are listed in Table 2.4. Plagioclase is Na-rich with An₁₀₋₃₀ with one exception, sample HJ-57b from the GAG, which has An₈₂. Within the LBS, plagioclase becomes increasingly An-rich with proximity to garnet (Hindemith, 2013). In the PLV-LM, the cores of plagioclase have a higher average An content in samples 10-AI-20A and 10-AI-114-B1, while the

rest are homogeneous. Differences in core and rim were not investigated in the data obtained for the LBS and GAG samples from previous work. K-feldspar has Or_{76-93} .

2.4.4 Interpretation of mineral chemistry

The variation in mineral chemistry between samples is consistent with the wide range of bulk rock compositions considered. In contrast, variations within individual samples, reflect incomplete re-equilibration during cooling from the metamorphic peak.

The generally uniform composition of garnet cores is consistent with homogenisation during high temperature metamorphism. The slight increase in $x(Fe)$ at the rim of garnet porphyroblasts suggests partial resetting during cooling since higher $x(Fe)$ indicates lower temperatures (Spear, 1993). In combination with the slightly higher spessartine contents at the rim, this zoning is characteristic of a retrograde net transfer reaction (Spear, 1993). This is consistent with textural evidence of $Bi + Sill \pm Pl$ growth at the expense of garnet rims, inferred to have occurred during melt crystallization. In addition to the net transfer reaction, the observation that biotite has the lowest $x(Fe)$ where it is adjacent to garnet suggests that there was also retrograde Fe-Mg exchange between garnet and biotite (Spear, 1993). Within this framework, the composition of the garnet cores is inferred to represent the highest metamorphic temperatures. However, it is possible that at early stages of cooling the composition of the entire garnet was reset, this being most likely for small garnets that do not show retrograde zoning. Therefore, metamorphic conditions predicted by using garnet cores should be considered as ‘minimum’ peak conditions. Concerning biotite, because a large part of it may have been

produced during melt crystallisation, its composition is not appropriate for the determination of the thermal peak.

2.5 PHASE EQUILIBRIA MODELING

The P - T pseudosections in this study were calculated with THERMOCALC 3.33 (Powell and Holland, 1988) using the bulk composition of each sample in the Na_2O - CaO - K_2O - FeO - MgO - Al_2O_3 - SiO_2 - H_2O - TiO_2 - O (NCKFMASHTO) system. Mn was not considered in this system because of the low contents in the bulk composition and this omission should not affect the results and interpretation significantly.

2.5.1 Bulk Compositions

The bulk compositions of the samples were calculated as molar % of oxides by combining modal proportions determined with the SEM-MLA and the average chemical composition for each mineral (average of rim and core chemical analysis of many grains in all textural settings), determined with the SEM-MLA and the EMP, respectively. The bulk H_2O was calculated as the sum of the H_2O in biotite and cordierite using the methods outlined in White et al. (2007) and Harley et al. (2002), respectively. The values have been normalized after removing secondary minerals and alterations, unknown minerals, sulfides, and minor phases such as monazite and zircon which cannot be accounted for in the NCKFMASHTO system.

The bulk compositions are listed in Table 2.5, and are plotted on an AFM diagram in Figure 2.6. Most have $x(\text{Fe})$ between 0.5 and 0.63 with two exceptions, HJ-57-C2 and HJ-35a. Samples from the PLV-LM have higher alumina index than those from the LBS (~0.32–0.50 vs ~0.15–22) whereas the alumina index in those from the GAG has a wide range of values. Samples with an alumina index of >0.25 and <0.25 correspond to the sillimanite-rich and sillimanite-poor groups, respectively. One sample in particular, HJ-57-C2, has an anomalous bulk composition that plots far from the main cluster, with much higher alumina index and $x(\text{Mg})$. The bulk composition of the two mid-*P* LBS samples (333x and 216c) for which *P–T* pseudosections are published in Lasalle and Indares, (2014) are also plotted on the diagram for comparison. These samples have higher alumina index than those from the LBS investigated here.

2.5.2 *P–T* pseudosections

The calculations used the internally consistent dataset *tcds55* (Powell and Holland, 1988), created November 22, 2003, and the minerals Liq–Q–G–Ksp–Pl–Sill–Bi–Cd–Mu–Ru–Ilm–Opx were considered in the calculations. The following *a–x* models were used: garnet (*g*: White et al., 2007), biotite (*bi*: White et al., 2007), cordierite (*cd*: Holland and Powell, 1998), muscovite (*mu*: Coggon and Holland, 2002), plagioclase and K-feldspar (*pl*, *ksp*: Holland and Powell, 2003), orthopyroxene (*opx*: White et al., 2002), ilmenite (*ilm*: White et al., 2000) and melt (*liq*: White et al., 2007). The NCKFMASHTO system also takes into account Fe^{3+} , which is calculated based on an input value of O

(oxygen) in the bulk composition. For consistency, a low value of oxygen equal to 0.05 was used.

The pseudosections were calculated in the P – T range of 3–15 kbar and 700–1000 °C. The full topologies and isomodes for four pseudosections from each area are shown in Figures 2.7–2.9, and P – T paths and isopleths for two examples from each area are shown in Figure 2.10 with a reduced range of 5–13 kbar and 800–950 °C.

2.5.2.1 General Topologies

Within the sillimanite-stability field, all topologies of the P – T pseudosections are muscovite-free and can be divided into two main parts: (1) a mid- P area between the cordierite-in phase boundary and the sillimanite–kyanite transition line, and (2) a low- P area, with cordierite-bearing topologies. Cordierite becomes stable between ~5 and 8 kbar.

Mid- P topologies of the sillimanite-rich samples (Figures 2.7a–d and 2.9a,c,d) are characterized by: (a) a sub vertical solidus within the temperature range of 810–860 °C, and (b) a sub-vertical biotite-out line at higher temperatures. In most cases, biotite is eliminated before 910 °C, but in the P – T pseudosection of 10-AI-58-3B1 (Figure 2.7b), which is quartz poor (see Table 1), quartz is eliminated first, and biotite is stable up to 1050 °C (outside of the range of the diagram). Mid- P topologies of the sillimanite-poor samples show a sub-vertical solidus at 820–870 °C, but up- T orthopyroxene becomes stable before the elimination of biotite (Figures 2.8 a,c,d and 2.9b) or at the biotite-out phase boundary (Figure 2.8b), and both phase boundaries have moderate positive dP/dT

gradients. In these pseudosections, sillimanite is either stable at near solidus conditions (Figure 2.8a-b) or is not stable at all in the mid- P topologies. The later is the case of samples with sillimanite restricted to garnet inclusions. In addition, some mid- P topologies show a plagioclase-out phase boundary up- T at near solidus conditions (in the case of 10-AI-114-B1 and 10-AI-58-3B1 (Figures 2.7b,c) which have only retrograde plagioclase), or at higher T (Figures 2.7a, 2.8a and 2.9c). Mid- P topologies are generally extended into the kyanite stability field, where muscovite becomes stable on the high- P /low- T side of most pseudosections.

Low- P topologies are controlled by shallow dP/dT gradient field boundaries involving the cordierite-in and garnet-out phase boundaries, as well as the appearance of orthopyroxene in the case of the sillimanite-rich samples. Quartz is generally stable throughout the entire range, except in 10-AI-58-3B1, 354-2-04 and 331-e2-11 (Figures 2.7b, 2.8a,c), where it is lost at higher- T . Minor phases include one or more of rutile, ilmenite and magnetite, where rutile is stable throughout or on the high- P side when paired with ilmenite.

For the samples investigated, the P - T stability field of the inferred peak mineral assemblage (Field I) falls within the mid- P part of the pseudosections. For the sillimanite-rich samples, the peak assemblage $\text{Liq}+\text{Bi}+\text{G}+\text{Q}+\text{Sill}+\text{Ksp}\pm\text{Pl}$ is stable between the solidus and the biotite-out phase boundary. Exceptions are the samples with retrograde plagioclase (10-AI-114-B1 and 10-AI-58-3B1, which also has little quartz; Figures 2.7b,c) for which the peak assemblage is stable between the plagioclase-out and biotite-

out or quartz-out phase boundaries, respectively. For the sillimanite-poor samples, the peak assemblage $\text{Liq}+\text{Bi}+\text{G}+\text{Q}+\text{Ksp}+\text{Pl}$ is stable between: (a) the solidus and the orthopyroxene-in phase boundary, in the case of rocks with no sillimanite, or sillimanite restricted to garnet inclusions (Figures 2.8c-d and 2.9b); (b) the sillimanite-out and orthopyroxene-in / biotite-out phase boundaries (Figure 2.8a,b). In terms of T and P conditions, Field I falls within the range of 820–900°C, 820–890°C and 830–920°C in the PLV-LM, LBS and GAG, respectively, at the P interval between ~6–7 (defined by the cordierite-out phase boundary) to 10–12 kbar (defined by the sill–ky transition).

2.5.2.2 Isomodes and isopleths

The isomodes for plagioclase, sillimanite, biotite, garnet and liquid were calculated in Field I for each sample and are shown in Figures 2.7– 2.9. Within the stability field of $\text{Liq}+\text{G}+\text{Bi}+\text{Ksp}+\text{Q}\pm\text{Pl}\pm\text{Sill}$, the isomodes generally have a steep, positive dP/dT gradient. The proportions of sillimanite, plagioclase and biotite decrease, while liquid and garnet increase with increasing T . These trends are consistent with the biotite dehydration reaction A ($\text{Bi} + \text{Q} + \text{AS} \pm \text{Pl} \rightarrow \text{G} + \text{Ksp} + \text{melt}$), discussed earlier. In the quartz-poor sample 10-AI-58-3B1 (Figure 2.7b), at T conditions above the quartz-out phase boundary, biotite isomodes become moderately negative, liquid and sillimanite isomodes become steeply positive, and garnet does not change.

Between the solidus and biotite-out phase boundary, the melt proportion increases with T . The melt fraction is 10% or less for most samples up to the elimination of biotite;

however, in 10-AI-114B1 and 10-AI-58-3B1, which are the most-rich in biotite, it reaches about 20% and 40%, respectively (Figures 2.7b,c).

The isopleths $x(g)$, $z(g)$, $ca(pl)$ and $x(bi)$ in Field I for each sample are shown in Figure 2.10. These are defined in THERMOCALC as $x(g) = Fe/(Fe+Mg)$ and $z(g) = Ca/(Fe+Mg+Ca)$ of garnet, $ca(pl)$ is the anorthitic portion of plagioclase, and $x(bi)$ is $Fe/(Fe+Mg)$ of biotite.

Within the fields of interest, the $x(g)$ and $x(bi)$ isopleths have a steep, positive dP/dT gradient and their values decrease with increasing T in all pseudosections except in those in which the peak mineral assemblage is sillimanite-free, where they have a steep negative dP/dT gradient (Figure 2.10 c–e). The $z(g)$ isopleths generally have a shallow positive dP/dT gradient that increases with P , however, in fields that lack plagioclase, $z(g)$ becomes sub-vertical and in sillimanite-absent fields, these have a moderate negative slope. Isopleths of $ca(pl)$ typically have moderate positive dP/dT gradients.

2.5.2.3 *P–T paths*

The $P–T$ pseudosections can provide several constraints on the peak and retrograde $P–T$ conditions experienced by the investigated rocks. These include: (1) the location of the $P–T$ stability fields of the peak mineral assemblages in the pseudosections, gives the general range of metamorphic conditions, as discussed earlier, (2) the intersection of the calculated isopleths, compared with the mineral chemistry of the rock, provides a minimum peak T (minimum because of potential re-equilibration of the peak compositions during retrograde cooling; see section on mineral chemistry), (3) the degree

of retrogression observed in the thin section is dependent on the angle at which the P - T path cuts the isomodes, and the density of isomodes crossed between the peak conditions and melt crystallization, therefore provides constraints on the shape of the retrograde P - T path and (4) the actual mineral proportions in the rock compared with those along the solidus should match at the P - T conditions of melt crystallization.

Table 2.6 shows the isopleths for each sample, and the P - T coordinates of the peak and of melt crystallization. Isopleths that were used to constrain the minimum peak T are highlighted in bold, mainly $z(g)$ and $x(g)$ from the cores of large garnet. However, in most cases, the isopleths coincide with the solidus, implying adjustments of the mineral chemistry during retrogression, and therefore the peak T is mainly constrained by the stability field of the peak assemblage. Additionally, isopleths of $z(g)$ are widely spaced in this field and provide little constrain on the P of the peak and of melt crystallization. Furthermore, the mineral modes do not change significantly along the solidus between the cordierite phase boundary and the sillimanite-kyanite transition line, so the P of melt crystallization cannot be well constrained unless the sample has retrograde cordierite (see Table 2.1b for comparison of mineral modes at the solidus with the modes of the thin section). For these reasons, a range of possible P - T paths are shown in green (Figure 2.10). Two samples from each area are used for constraining P - T paths; these were chosen on the basis of the best preserved peak assemblages and on the presence or absence of retrograde cordierite.

The P - T paths for 10-AI-20A and 10-AI-58-3B1 from the PLV-LM are shown in Figure 2.10 (a,b). The peak metamorphic assemblage is stable within the $\text{Liq}+\text{G}+\text{Bi}+\text{Sill}+\text{Q}+\text{Ksp}+\text{Pl}$ and $\text{Liq}+\text{G}+\text{Bi}+\text{Sill}+\text{Q}+\text{Ksp}$ fields of each pseudosection, respectively. The minimum peak T and the peak P predicted by the intersection of $z(\text{g})$ and $x(\text{g})$ is 840–865°C and 9–11 kbar.

The moderate replacement of porphyroblastic garnet by $\text{Bi}+\text{Sill}+\text{Pl}+\text{Q}$ in these samples is consistent with the retrograde portion of the P - T path cutting the isomodes for these phases at a high angle, therefore following a shallow to moderate dP/dT gradient. Because of the presence of retrograde cordierite (or pinnite) in 10-AI-58-3B1, the P - T path must cross the cordierite phase boundary; however, 10-AI-20A does not have cordierite and melt solidification must occur at P above the cordierite stability field, but not much higher since the two rocks come from the same area. The T of the solidus and the presence of retrograde cordierite in 10-AI-58-3B1 constrain the conditions of melt solidification at ~820–840 °C and 6–7 kbar in these samples.

The P - T paths for two samples from the LBS, 331-e2-11 and 216a, are shown in Figure 2.10 (c,d). The peak metamorphic assemblage is stable within the $\text{Liq}+\text{G}+\text{Bi}+\text{Ksp}+\text{Q}+\text{Pl}$ field of the pseudosections. The $x(\text{g})$ isopleth coincides with the solidus in both samples so the peak T is only constrained by the T range of Field I, at 830–875 °C with a P of 8–11 kbar. In both cases, it was interpreted on textural grounds that sillimanite is not part of the peak assemblage but was introduced at lower T during melt crystallization, as a product of partial garnet replacement. This interpretation is

consistent with a P - T path at high angle to the isomodes and a peak T that is much higher than the T of the solidus. The conditions of melt solidification were constrained to 825–875°C (approximately the same as peak T for this area) and 6.5–8 kbar based on the shallow to moderate dP/dT gradient needed for the production of retrograde sillimanite, and on the lack of orthopyroxene or cordierite.

The P - T paths for two GAG samples, HJ-58c and 10-AI-76, are shown in Figure 2.10 (e,f). The peak metamorphic assemblage of HJ-58C is stable within the Liq+G+Bi+Sill+Ksp+Q+Pl field or possibly at T above the biotite-out phase boundary this field is narrow and all biotite may be retrograde. The peak metamorphic assemblage of 10-AI-76 lacks sillimanite, and therefore is stable within the Liq+Bi+G+Pl+Q+Ksp+Ru field. In both samples, $x(g)$ coincided with the solidus, however, based on the T range of Field I and $z(g)$ of the garnet core, the minimum peak T is constrained to 840–845 °C with a corresponding P of 8–11kbar. Partial replacement of garnet rims by sillimanite is consistent with a shallow to moderate dP/dT gradient. Because of the lack of cordierite in these samples, the P - T path may cross the solidus anywhere above the cordierite or orthopyroxene phase boundaries, at 835–840°C and 6–8 kbar.

2.5.3 Melt reintegration

It is common for anatectic rocks to experience melt loss in orogenic environments because the melt is squeezed out under deviatoric stress (Brown, 2007). Texturally, the

generally good preservation of the peak assemblage in the investigated samples suggests that a substantial portion of the melt was lost. This is because water, which is required for retrograde reactions, is dissolved in the melt and removed from the system (White and Powell, 2002). The absence of muscovite from mid- P topologies in all pseudosections (muscovite generally becomes stable ~ 13 kbar or higher) and the sub-vertical slope of the solidus, compared with a moderate dP/dT gradient of a water saturated solidus, also suggest melt loss (Indares *et al.*, 2008).

The current bulk compositions therefore represent the final composition of the rock after the loss of melt. Considering this, topologies calculated at temperatures below the solidus (liq=0 line) in these diagrams are not representative of those present under subsolidus conditions, and when considering P - T paths only the peak and retrograde portion can be inferred by these P - T pseudosections (White and Powell, 2002). For this reason, additional pseudosections were calculated with melt reintegrated for selected samples to determine the full P - T path.

To construct these diagrams, the composition of the first infinitesimal amount of melt was calculated where the prograde portion of the path was projected to have crossed the solidus. Although this P is not well constrained, it has been shown that the suprasolidus topologies of the melt reintegrated pseudosections are not significantly affected by P (Indares *et al.*, 2008). Proportions of melt with this composition were then added to the original bulk composition until an amount sufficient to make the water

saturated solidus stable was achieved. Therefore, in using this method, we assume that the rock was water saturated and that the melt loss occurred in one step.

It is not possible to calculate the exact amount of melt loss; however, it has been determined that the suprasolidus topologies of the melt-integrated pseudosections do not change significantly with varying quantities of added melt because they are largely controlled by the solid phases (White and Powell, 2002). Therefore, these melt-reintegrated phase equilibria diagrams are sufficient for the purposes of determining the prograde portion of the path.

Figure 2.11 examples of a melt reintegrated pseudosections for sillimanite-rich and sillimanite-poor (as inclusions in garnet only) samples, 10-AI-20A (from the PLV-LM) and 10-AI-76 (from the GAG), respectively. Melt loss was estimated to be 11 and 20% for these samples. In the former, the T range of the diagram was lowered to 650 °C to show the relevant topologies. The thick dashed white line in the diagrams showing the full P - T path represents the “dry” solidus from the diagrams calculated with the bulk compositions of the rock (before melt reintegration). The “wet” solidus in the melt reintegrated diagrams occurs at much lower temperatures, outside of the range of the pseudosection. The portion of the pseudosection above the “dry” solidus is quite similar in the both the original and melt reintegrated pseudosections, and therefore will not be discussed again here.

2.5.3.1 General topologies and P - T paths of melt reintegrated pseudosections

For all samples, the stability field of muscovite has been shifted to lower pressures in the melt reintegrated diagrams. The appearance of sillimanite or K-feldspar coincides approximately with the disappearance of muscovite for at least a portion of the phase boundaries. A sub-vertical garnet-in phase boundary occurs at temperatures in the range of 700 – 800°C. Because Mn, which expands the stability of garnet to lower T (White *et al.*, 2014), was not considered in the bulk composition, yet a small percentage of garnet is spessartine, the T of the garnet-in boundary in the pseudosections is likely overestimated.

For the samples that have sillimanite as inclusions in garnet porphyroblasts only, there is field where sillimanite becomes stable below the “dry” solidus within the temperature range of 700–800 °C. This explains the presence of sillimanite as inclusions when there is no sillimanite stable within the peak topology, since it is not part of the peak assemblage.

The prograde portions of the P – T paths were constrained by the sillimanite-kyanite transition line since in each of the diagrams garnet grows in the presence of sillimanite and this mineral is found as inclusions within garnet poikiloblasts in the large majority of the investigated samples. This results in the prograde portion of the path having a slope with a moderate dP/dT gradient.

2.5.4 Cordierite stability in the pseudosections

Unlike sample 10-AI-58-3B1 (Figure 2.2b), where cordierite clearly corrodes garnet, samples 10-AI-58-2a and HJ-57-C2 have significant cordierite distributed

throughout the matrix as wispy aggregates (Figures 2.2d and 2.4d). These samples are fine-grained and have likely been extensively re-equilibrated during retrogression. Because of this, it is inconclusive as to whether or not cordierite is part of the peak assemblage. Although these samples were not used to infer P - T conditions and paths, their pseudosections have been included (Figures 2.7d and 2.9d) to investigate the role of bulk composition on the stability of cordierite. Both samples are part of the sillimanite-rich group, with a peak assemblage of G+Bt+Sill+Q+Pl+Ksp and possibly cordierite.

It is known that increasing $x(\text{Mg}) = \text{Mg}/(\text{Fe}+\text{Mg})$ expands the cordierite stability field to higher P (Spear *et al.* 1999; Groppo *et al.*, 2013) and this correlation can be seen to some extent by comparing the $x(\text{Mg})$ of the bulk compositions (Table 2.5) with the locations of the cordierite-in phase boundary in the calculated pseudosections (Figure 2.7–2.9). In particular by comparing the P of the solidus-cordierite point with the bulk $x(\text{Mg})$, samples can be divided into three groups. (1) Samples 354-2-03 and 10-AI-76 have the lowest $x(\text{Mg})$ at <0.40 , and correspondingly, the lowest P at which cordierite becomes stable, at ~ 5 kbar in each (Figures 2.8c and 2.9b). (2) The majority of the samples have an intermediate $x(\text{Mg})$ in the range of 0.40 – 0.50 , and for these cordierite becomes stable between 6.01 and 7.11 kbar. (3) Finally, in HJ-57-C2, which has the highest $x(\text{Mg})$ of 0.74 , cordierite is stable up to ~ 8 kbar (Figure 2.9d). In samples with the lowest $x(\text{Mg})$ and P of the cordierite-in boundary (group 1), orthopyroxene becomes stable before cordierite. Additionally, in fields that are both sillimanite and orthopyroxene-absent, cordierite first becomes stable at lower P compared with samples with similar $x(\text{Mg})$ in sillimanite-present fields.

Based on the P of the cordierite-in phase boundary compared with the P - T paths from each area, it is likely that cordierite was not part of the peak assemblage of 10-AI-58-2a since the peak- P is much higher than that at which cordierite first becomes stable (~6.5–7.5 kbar for cordierite compared with 8–11 kbar for the peak- P of other samples in the area). However, because the cordierite-in phase boundary occurs at ~8–9 kbar between the solidus and biotite boundaries in HJ-57-C2, it is completely possible that cordierite was a peak phase in this sample.

2.6 DISCUSSION AND CONCLUSIONS

This study investigated the pressure-temperature (P - T) evolution of aluminous gneisses from the mid- P granulite facies hinterland of the Central Grenville Province. The samples come from three distinct locations in the Manicouagan and Lac du Milieu areas and belong to three supracrustal units: (1) the Complexe de la Plus Value in Lac du Milieu (PLV-ML); (2) the Layered Bimodal Sequence (LBS); and (3) the Gabriel Aluminous Gneisses (GAG). The aluminous character of these rocks is partly derived by pre-metamorphic hydrothermal alteration. The samples have the main assemblage $G+Bi+Q+Ksp\pm Pl\pm Sill$ but due to variable mineral modes display a wide range of bulk compositions and textures. These were divided into two main groups: (1) sillimanite-rich samples, with a high Alumina index in AFM space, and (2) sillimanite-poor or absent samples with a low Alumina index. In the latter samples, sillimanite restricted to garnet inclusions, aluminous nodules or patches, and is not part of the peak assemblage. Samples from the PLV-LM

and LBS fall into groups 1 and 2, respectively, and samples from the GAG are part of either group.

In addition, some samples contain cordierite which based on the textures is inferred to be a retrograde phase in the PLV-LM, but has an inconclusive origin in samples of the GAG. Furthermore, the presence of cordierite can also be related to the bulk composition, The GAG samples have distinctively high $x(\text{Mg})$, which may have stabilized cordierite at the thermal peak, whereas the samples with retrograde cordierite from the PLV-LM, have higher $x(\text{Mg})$ than those that do not.

Most samples contain micro-textural evidence of former melt, including pseudomorphed former melt inclusions in garnet, relict quartz surrounded by thin feldspar rims, inter-granular films in the matrix and biotite-quartz symplectites. Additionally, garnet overgrowing sillimanite, and the local replacement of garnet by biotite-sillimanite, are textures related to the biotite-melting reaction.

P - T pseudosections (calculated in the NCKFMASHTO system with Thermocalc) show different topologies for the sillimanite-rich and poor samples, and support textural evidence that in the later samples, sillimanite is not part of the peak assemblage. In addition, they support evidence that cordierite and plagioclase, are of retrograde origin in some rocks.

Evidence of melt and the peak mineral assemblages places the peak metamorphic conditions within the stability field of $\text{Liq}+\text{G}+\text{Bi}+\text{Ksp}+\text{Q}+\text{Pl}+\text{Sill}$. The minimum peak T predicted by the P - T pseudosections is in the range 815–880 °C at 8–10kbar; however,

the actual peak T could be higher, up to the loss of biotite, in most cases. Following retrogression, melt is predicted to have solidified at a T of 800–865 °C at 6–9kbar (Table 2.6). The P of melt solidification is better constrained in samples that contain retrograde cordierite, because in this case it corresponds to the intersection between the solidus and the cordierite phase boundary. In addition, retrograde replacement of garnet by sillimanite in most samples require a retrograde P – T path with a moderate dP/dT gradient.

Preservation of the peak assemblage suggests that there was melt loss; therefore, the prograde portion of the P – T path was investigated by means of melt-reintegrated P – T pseudosections. This portion of the path falls below the sillimanite/kyanite transition, based on the presence of sillimanite as inclusions within garnet. Melt reintegration suggests that melt loss ranged from 10 to 31%.

Metamorphic P – T paths predicted by the P – T pseudosections, by comparing mineral assemblages textural and mineral composition data of the rocks with the calculated topologies, are broadly similar in all locations and rock types. The generalized P – T path has an overall “tilted hair pin” shape with a moderate dP/dT gradient. The data suggest that this part of the mid- P hinterland in the central Grenville experienced a uniform metamorphic evolution, with large temperature variations relative to pressure. The high metamorphic temperatures recorded by these rocks are consistent with the idea that the Grenville is a large hot orogen.

REFERENCES

- Beaumont, C. Jamieson, R.A., Nguyen, M.H. 2010. Models of large hot orogens containing a collage of reworked and accreted terranes. *Canadian Journal of Earth Sciences* 47, 485–515.
- Beaumont, C., Nguyen, M.H., Jamieson, R.A., Lee, B. 2006. Crustal flow modes in large hot orogens. *Geological Society of London Special Publication* 268, 91–145.
- Brown, M. 2007. Crustal melting and melt extraction, ascent and emplacement in orogens: mechanism and consequences. *Journal of Geological Society of London*, 164, 709–730.
- Coggon, R. and Holland, T. J. B., 2002. Mixing properties of phengitic micas and revised garnet-phengite thermobarometers. *Journal of Metamorphic Geology*, 20, 683–696.
- Dunning G, and Indares, A., 2010. New insights on the 1.7–1.0 Ga crustal evolution of the central Grenville from the Manicouagan-Baie Comeau transect. *Precambrian Research*, 180, 204–226.
- Gower, C. F. and Krogh, T. E. 2002. A U–Pb geochronological review of the Proterozoic history of the eastern Grenville Province. *Canadian Journal of Earth Sciences* 39, 795–829.
- Grosso, C., Rolfo, F., Mosca, P. 2013. The cordierite-bearing anatectic rocks of the higher Himalayan crystallines (eastern Nepal): low-pressure anatexis, melt productivity, melt loss and the preservation of cordierite. *Journal of Metamorphic Geology*. 31, 187–204.
- Harley, S. L., Thompson, P. P., Hensen, B. J., Buick, I. S. 2002. Cordierite as a sensor of fluid conditions in high-grade metamorphism and crustal anatexis. *Journal of Metamorphic Geology*, 20(1), 71–86.
- Hindemith, M. A., 2013. Petrography and geochemistry of hydrothermally altered volcanic rocks metamorphosed at granulite-facies conditions: an example from the central Grenville Province. Masters Thesis. Memorial University of Newfoundland. 131 Pages.
- Hodych, J.P., and Dunning, G.R. 1992. Did the Manicouagan impact trigger end-of-Triassic mass extinction? *Geology*, 20: 51–54.

- Holland, T. J. B. and Powell, R., 1998. An internally-consistent thermodynamic data set for phases of petrological interest. *Journal of Metamorphic Geology*, 16, 309–343.
- Holland, T. J. B. and Powell, R., 2003. Activity-composition relations for phases in petrological calculations: an asymmetric multicomponent formulation. *Contributions to Mineralogy and Petrology*, 145, 492–501.
- Indares, A. and Moukhsil, A., 2013. Geon 12 crustal extension in the central Grenville Province, implications for the orogenic architecture and potential influence on the emplacement of anorthosites. *Canadian Journal of Earth Sciences*, 50, 955-966.
- Indares, A.D., White, R.W., Powell, R., 2008. Phase equilibria modelling of kyanite bearing anatectic paragneisses from the central Grenville Province. *Journal of Metamorphic Geology*, 26, 815–836.
- Jamieson, R.A. and Beaumont, C., 2011. Coeval thrusting and extension during post-convergent ductile flow - implications for exhumation of high-grade metamorphic rocks. *Journal of Metamorphic Geology*, 29, 33–51.
- Jamieson, R.A., Beaumont, C., Nguyen, M.H., Culshaw, N.G., 2007. Synconvergent ductile flow in variable-strength continental crust: Numerical models with application to the western Grenville orogen. *Tectonics*, 26, 1–23.
- Jamieson, R.A., Beaumont, C., Warren, C.J., Nguyen, M.H., 2010. The Grenville Orogen explained? Applications and limitations of integrating numerical models with geological and geophysical data. In: *Lithoprobe - parameters, processes and the evolution of a continent* (Lithoprobe Synthesis Volume II, eds Clowes, R M., and Skulski, T.). *Canadian Journal of Earth Sciences*, 47, 517–539.
- Lasalle, S., Fisher, C.M., Indares, A., Dunning, G., 2013. Contrasting types of Grenvillian granulite facies aluminous gneisses: insights on protoliths and metamorphic events from zircon morphologies and ages. *Precambrian Research*, 228, 117–130.
- Lasalle, S. and Indares, A. (2014) Anatectic record and contrasting P – T paths of aluminous gneisses from the central Grenville Province. *Journal of Metamorphic Geology*, 32, 627-646.
- Letourneau, M. 2011. Anatectic aluminous gneisses from the mesoproterozoic Complexe de la Plus-Value, Grenville Province, Quebec. Memorial University: Honours thesis.
- Moukhsil, A., Solgadi, F., Lacoste, P., Gagnon, M., David, J., 2012. Geologie de la region du lac du Milieu. Ministere des Ressources naturelles et de la Faune, RG 2012-01, 1-33.

- Patrick, M. E., 2013 Metamorphic investigation of anatectic aluminous gneisses from the Complexe de la Plus-Value, Grenville Province. Honours thesis, Memorial University of Newfoundland
- Powell, R., Holland, T.J.B. 1988 An internally consistent thermodynamic dataset with uncertainties and correlations: 3. Applications to geobarometry, worked examples and a computer program. *Journal of Metamorphic Geology*, 6, 173-204
- Rivers, T., 2008 Assembly and preservation of lower, mid and upper orogenic crust in the Grenville Province – Implications for the evolution of large hot long-duration orogens. *Precambrian Research*, 167, 237-259.
- Rivers, T., 2012. Upper-crustal orogenic lid and mid-crustal core complexes: signature of a collapsed orogenic plateau in the hinterland of the Grenville Province. *Canadian Journal of Earth Sciences*, 49, 1–42.
- Rivers T, Culshaw N, Hynes A, Indares A, Jamieson R, Martignole J. 2012. The Grenville Orogen – A post-LITHOPROBE perspective. Chapter 3 In *Tectonic Styles in Canada: The LITHOPROBE Perspective*. (eds JA Percival, FA Cook, and RM Clowes) *Geological Association of Canada, Special Paper* 49, 97–236.
- Rivers, T. and Corrigan, D. 2000. Convergent margin on southeastern Laurentia during the Mesoproterozoic: tectonic implications. *Canadian Journal of Earth Sciences*, 37, 359–383.
- Rivers, T., Martignole, J., Gower, C.F., Davidson, A., 1989. New tectonic divisions of the Grenville Province, Southeast Canadian Shield. *Tectonics*, 8, 63-84.
- Spear, Frank S. 1993. *Metamorphic Phase Equilibria And Pressure-Temperature-Time Paths Monograph Series*. United States: Mineralogical Society of America : Washington, DC, United States, 1993. 799 Pages.
- Spear, F.S., Kohn, M.J., Cheney, J.T., 1999. P–T paths from anatectic pelites. *Contributions to Mineralogy and Petrology*, 134, 17–32.
- Strowbridge, S., 2006. Metamorphic evolution of anatectic metapelites from the Gabriel high strain zone, Grenville Province. Masters Thesis. Memorial University of Newfoundland.
- White, R.W. and Powell, R. 2002. Melt loss and the preservation of granulite facies assemblages. *Journal of Metamorphic Geology*, 20, 621-632.
- White, R. W., Powell, R., Clarke, G. L., 2002. The interpretation of reaction textures in Fe-rich metapelitic granulites of the Musgrave Block, central Australia: constraints

from mineral equilibria calculations in the system $K_2O-FeO-MgO-Al_2O_3-SiO_2-H_2O-TiO_2-Fe_2O_3$. *Journal of Metamorphic Geology*, 20, 621–632.

White, R.W., Powell, R., Holland, T.J.B., 2007. Progress relating to calculation of partial melting equilibria for metapelites. *Journal of Metamorphic Geology*, 25, 511–527.

White, R. W., Powell, R., Holland, T. J. B., Worley, B. A., 2000. The effect of TiO_2 and Fe_2O_3 on metapelitic assemblages at greenschist and amphibolite facies conditions: mineral equilibria calculations in the system $K_2O-FeO-MgO-Al_2O_3-SiO_2-H_2O-TiO_2-Fe_2O_3$. *Journal of Metamorphic Geology*, 18, 497–511.

White, R. W., Powell, R., Johnson, T. E., 2014. The effect of Mn on mineral stability in metapelites revisited: new a–x relations for manganese-bearing minerals. *Journal of Metamorphic Geology*, 32, 809–828.

Table 2.1. (a) Mineral modes as determined by SEM–MLA, and (b) compared with the modes at the solidus of the phase equilibria diagram. Sill/Al_{tot} = Proportion of sillimanite to total Sill-G-Bi-Cd; QF = Quartzofeldspathic; SR = Sillimanite-rich group; SP = Sillimanite-poor group. Sum of Al. Min.= Sill+G+Bi+Cd.

Mineral	PLV					GAG							LBS			
	10-AI-20A	10-AI-108-F	10-AI-58-2A	10-AI-58-3B1	10-AI-114-B1	HJ-34b	HJ-35a	HJ-58c	HJ-74	HJ-57c2	HJ-57b	10-AI-76	331-e2-11	333-2-03	354-2-03	216a
Garnet	7.10	1.97	4.43	9.57	15.22	14.32	15.19	13.98	9.38	0.16	4.87	4.75	3.64	6.62	6.42	12.48
Biotite	12.20	13.35	7.47	34.84	21.55	6.99	17.57	6.75	13.83	5.38	9.99	5.20	19.01	6.38	11.57	4.09
Sillimanite	5.31	5.07	3.55	30.92	13.15	4.52	5.49	1.99	0.00	9.41	4.14	0.02	0.59	0.00	0.51	0.50
Cordierite	0.05	0.77	2.84	2.25	0.20	0.00	2.04	0.00	0.00	0.76	0.00	0.00	0.00	0.00	0.00	0.87
Sum of Al. Min.	24.66	21.15	18.29	77.58	50.12	25.82	40.29	22.73	23.21	15.71	19.00	9.98	23.25	13.00	18.50	17.94
Sill/Altot	21.55	23.96	19.41	39.86	26.23	17.50	13.62	8.77	0.00	59.90	21.78	0.21	2.53	0.00	2.74	2.77
Quartz	36.57	47.32	68.86	12.53	37.76	62.54	56.72	35.08	19.85	73.65	41.74	23.26	14.88	39.73	19.76	32.12
K-Feldspar	27.36	1.72	4.39	6.51	7.81	11.63	2.37	12.70	5.17	10.49	37.32	48.67	39.35	12.52	28.75	30.27
Plagioclase	11.39	29.81	8.40	3.30	4.30	0.00	0.56	29.13	51.63	0.06	1.92	17.69	22.15	34.51	32.67	19.22
Sum of QF. Minerals	75.32	78.85	81.65	22.35	49.88	74.17	59.65	76.90	76.65	84.21	80.98	89.62	76.38	86.76	81.18	81.61
Rutile	0.00	0.00	0.03	0.02	0.00	0.00	0.00	0.28	0.02	0.08	0.02	0.00	0.00	0.12	0.00	0.36
Magnetite	0.02	0.00	0.00	0.00	0.00	0.01	0.05	0.09	0.11	0.00	0.00	0.00	0.00	0.00	0.00	0.08
Ilmenite	0.00	0.00	0.02	0.05	0.00	0.00	0.00	0.00	0.00	0.00	0.00	0.16	0.38	0.11	0.16	0.00
Spinel	0.00	0.00	0.00	0.00	0.00	0.00	0.00	0.00	0.00	0.00	0.00	0.25	0.00	0.00	0.17	0.00
SUM	100	100	100	100	100	100	100	100	100	100	100	100	100	100	100	100
Group	SR	SR	SR	SR	SR	SR	SR	SR	SP	SR	SR	SP	SP	SP	SP	SP

b)

	10-AI-20A		10-AI-58-3B1		HJ-58c		10-AI-76		331-e2-11		216a	
	TS mode	Solidus	TS mode	Solidus	TS mode	Solidus	TS mode	Solidus	TS mode	Solidus	TS mode	Solidus
Garnet	7.10	8.86	9.57	13.51	13.98	19.41	4.75	7.02	3.64	5.76	12.48	17.30
Biotite	12.20	13.91	34.84	31.95	6.75	7.77	5.20	5.50	19.01	21.76	4.09	4.31
Sillimanite	5.31	5.31	30.92	25.91	1.99	1.81	0.02	0.00	0.59	0.00	0.50	0.34
Cordierite	0.05	0.00	2.25	4.42	0.00	0.00	0.00	0.00	0.00	0.00	0.87	0.00
Quartz	36.57	36.86	12.53	12.04	35.08	34.00	23.26	24.26	14.88	15.94	32.12	32.15
Sum of Felds	38.75	34.99	9.81	11.47	41.83	37.00	66.35	62.63	61.50	56.16	49.49	45.19

Table 2.2. Compositional ranges of garnet in terms of Alm, Prp, Grs, Sps and $x(\text{Fe}) = \text{Fe}/(\text{Fe}+\text{Mg})$.

Location	Sample	End Members of Grt (%)				$x(\text{Fe})$ (%)
		Alm	Prp	Grs	Sps	
PLV-LM ¹	10-AI-58-3B1	64.4-71.7	23.8-31.5	2.65-2.94	1.12-1.66	64.4-71.7
PLV-LM ¹	10-AI-20A	65.2-75.7	19.4-29.6	2.25-3.23	1.98-2.67	65.1-75.7
PLV-LM ¹	10-AI-58-2A	67.3-72.2	23.7-28.7	2.94-3.13	0.89-1.05	68.4-72.2
PLV-LM ¹	10-AI-108F	69.7-72.6	19.8-23.1	2.32-2.47	4.79-5.40	69.7-72.6
PLV-LM ¹	10-AI-114B1	68.9-76.8	17.1-25.2	0-2.58	3.15-4.82	68.9-76.8
LBS ²	216a	51-65	30-46	3-4	0-1	53-68
LBS ²	331-e2-11	62.3-68.0	20.5-37.1	0.1-0.7	1.0-3.1	62.7-76.1
LBS ²	333-2-03	58.1-62.1	28.2-37.3	0-1.1	1.2-1.7	61.4-68.8
LBS ²	354-2-04	71.1-74.6	15.0-24.5	0.5	1.8-2.9	74.0-83.2
GAG ²	10-AI-76	64.3-65.9	22.3-25.2	0.1-0.6	4.5-4.9	72.0-74.5
GAG ³	HJ-34B	60	36	1	3	63
GAG ³	HJ-35a	56-59	35-38	2	3	59-63
GAG ³	HJ-58C	61-65	32-36	2-3	1	63-67
GAG	HJ-74	59.2-66.0	20.4-26.2	7.0-12.7	3.5-5.0	70.0-76.4
GAG	HJ-57b	49-50	38-40	5-7	5	55-57
GAG	HJ-57-C2	21.1-23.2	39.2-48.0	4.0-4.9	26.6-34.4	30.6-36.9

From: ¹Patrick (2013) ²Hindemith (2013) ³Strowbridge (2006)

Table 2.3. Compositional ranges of biotite in terms of Ti, Al^{VI}, x(Fe) = Fe/(Fe+Mg) and F, and cordierite in terms of x(Fe).

Location	Sample	Biotite				Cordierite
		Ti (p.f.u)	Al(VI) (p.f.u)	x(Fe) (%)	F	x(Fe) (%)
PLV-LM ¹	10-AI-58-3B1	0.27-0.30	0.15-0.17	39-42	0.09-0.11	21.8-25.5
PLV-LM ¹	10-AI-20A	0.06-0.22	0.24-0.36	30-42	0.14-0.23	X
PLV-LM ¹	10-AI-58-2A	0.26-0.31	0.16-0.21	36-42	0.08-0.10	22.0-24.6
PLV-LM ¹	10-AI-108F	0.14-0.24	0.26-0.42	43-47	0.07-0.12	26.5-27.3
PLV-LM ¹	10-AI-114B1	0.12-0.24	0.24-0.35	35-48	0.10-0.13	X
LBS ²	216a	0.26-0.36	0.08-0.12	34-39	N/A	X
LBS ²	331-e2-11	0.12-0.24	0.17-0.37	35.6-45.6	0-0.07	X
LBS ²	333-2-03	0.20-0.33	0.14-0.29	29.6-46.2	0.05-0.15	X
LBS ²	354-2-04	0.14-0.32	0.14-0.33	34.0-48.5	0.04-0.16	X
GAG ²	10-AI-76	0.49-0.68	0.21-0.40	38.6-49.6	0.09-0.31	X
GAG ³	HJ-34B	0.25	0.1	25	0	X
GAG ³	HJ-35a	0.10-0.18	0.08-0.14	17-18	0.22-0.30	9-13
GAG ³	HJ-58C	0.28-0.29	0.10-0.11	32	N/A	X
GAG	HJ-74	0.23-0.31	0-0.02	34.5-39.7	N/A	X
GAG	HJ-57b	0.24-0.31	0.02-0.07	18.7-25.2	N/A	X
GAG	HJ-57-C2	0.13-0.26	0.01-0.09	5.9-19.6	N/A	4.5-5.0

From: ¹Patrick (2013) ²Hindemith (2013) ³Strowbridge (2006)

X = none in sample

p.f.u: on the basis of 11 O

N/A = Not analyzed

Table 2.4. Compositional ranges of feldspars in terms of An, Or and Ab (%).

Location	Sample	Plagioclase			K-feldspar		
		Ab	An	Or	Ab	An	Or
PLV-LM ¹	10-AI-58-3B1	71.9-73.9	25.3-27.2	0.77-1.11	14.1-17.9	0.18-0.67	81.5-85.7
PLV-LM ¹	10-AI-20A	75.8-83.2	16.0-22.7	0.72-1.57	10.8-15.9	0-2.5	83.1-86.3
PLV-LM ¹	10-AI-58-2A	70.4-69.5	28.7-29.5	0.91-1.36	8.9-14.9	0.28-0.93	83.4-90.3
PLV-LM ¹	10-AI-108F	77.2-79.2	19.8-21.4	1.00-1.73	11.5-12.5	0.19-0.29	86.2-87.5
PLV-LM ¹	10-AI-114B1	76.4-83.1	15.9-22.7	0.77-1.07	10.5-12.6	0-.21	86.3-88.3
LBS ²	216a	73-94	13-26	N/A	N/A	N/A	N/A
LBS ²	331-e2-11	78.9-90.3	8.4-20.6	0.6-1.4	7.9-21.3	0.2-0.6	78.4-91.2
LBS ²	333-2-03	80.6-87.2	12.7-13.9	0.9-1.9	5.9-16.1	0.1-1.0	83.1-93.1
LBS ²	354-2-04	71.5-87.1	11.3-25.9	0.6-1.6	9.3-24.2	0.1-0.5	76.8-91.0
GAG ²	10-AI-76	73.3-76.3	22.7-26.9	1-1.7	8.4-19.0	0.2-0.7	76.3-92.1
GAG ³	HJ-34B	X	X	X	7.4-17.9	0.02-0.52	82.0-92.6
GAG ³	HJ-35a	76	23	0	8.9-19.7	0-0.02	80.0-91.1
GAG ³	HJ-58C	78	20-21	1-2	8.7-18.8	0.01-1.8	79.4-91.1
GAG	HJ-74	80	20	0	9.4-20.4	0.02-1.0	79.1-90.3
GAG	HJ-57b	18	82	0	10.8-17.4	0.5-2.4	80.8-88.7
GAG	HJ-57-C2	X	X	X	9.7-10.4	0.32-0.36	88.6-89.8

From: ¹Patrick (2013) ²Hindemith (2013) ³Strowbridge (2006)

X = none in sample

N/A = Not analyzed

Table 2.5. Bulk compositions used in phase equilibrium modeling. $x(\text{Fe}) = \text{Fe}/(\text{Fe}+\text{Mg})$; $x(\text{Na})=\text{Na}/(\text{Na}+\text{Ca}+\text{K})$; $x(\text{K})=\text{K}/(\text{Na}+\text{Ca}+\text{K})$; $x(\text{Ca})=\text{Ca}/(\text{Na}+\text{Ca}+\text{K})$.

	Oxides (Mol %)										sum	X(Fe)*	x(Na)	x(K)	x(Ca)
	SiO2	Al2O3	MgO	FeO	MnO	CaO	Na2O	K2O	TiO2	H2O					
PLV															
10-AI-58-3B1	52.57	21.25	8.55	8.53	0.06	0.36	0.44	3.02	1.46	3.77	100	0.50	0.12	0.79	0.09
10-AI-20-A	73.75	10.25	3.8	4.56	0.09	0.67	1.49	3.52	0.3	1.58	100	0.55	0.26	0.62	0.12
10-AI-58-2A	83.64	6.35	2.75	3.03	0.03	1.63	0.26	1.02	0.17	1.13	100	0.52	0.09	0.35	0.56
10-AI-108F	77.21	9.38	2.82	2.93	0.06	1.47	2.73	1.32	0.41	1.67	100	0.51	0.49	0.24	0.27
10-AI-114-B	64.64	13.88	5.97	9.08	0.34	0.35	0.49	2.17	0.58	2.49	100	0.60	0.16	0.72	0.12
LBS															
216a	73.97	9.38	3.94	4.91	0.00	1.36	1.75	3.60	0.63	0.46	100	0.55	0.26	0.54	0.20
331-e2-11	67.09	10.87	4.69	4.94	0.05	1.11	2.73	5.21	0.89	2.41	100	0.51	0.30	0.58	0.12
333-2-03	77.77	7.97	2.64	3.27	0.46	1.32	3.62	1.70	0.50	0.73	100	0.55	0.55	0.26	0.20
354-2-04	70.38	10.43	3.31	5.08	0.10	1.46	3.65	3.64	0.63	1.32	100	0.61	0.42	0.42	0.17
Gabriel															
HJ-34b	79.33	6.91	4.67	5.76	0.25	0.08	0.50	1.44	0.26	0.81	100	0.55	0.25	0.71	0.04
HJ-35a	74.83	5.27	8.55	6.65	0.27	0.21	0.19	1.35	0.28	2.40	100	0.44	0.11	0.77	0.12
HJ-58C	72.17	9.93	4.25	6.49	0.08	1.62	2.81	1.59	0.29	0.76	100	0.60	0.47	0.26	0.27
HJ-74	67.52	11.24	3.61	6.06	0.25	2.87	4.83	1.49	0.56	1.57	100	0.63	0.53	0.16	0.31
HJ-57b	78.10	8.73	2.91	3.27	0.12	0.15	0.81	4.26	0.48	1.16	100	0.53	0.15	0.82	0.03
HJ-57c2	88.54	6.54	1.72	0.61	0.03	0.01	0.18	1.41	0.34	0.62	100	0.26	0.11	0.88	0.00
10-AI-76	74.94	9.99	1.89	3.20	0.14	1.28	2.57	5.03	0.36	0.61	100	0.63	0.29	0.57	0.14
Melt reintegrated															
10-AI-20-A	71.87	9.82	3.08	3.77	0.00	0.66	1.85	3.45	0.24	5.25	100	0.55	0.31	0.58	0.11
10-AI-76	73.94	9.78	1.73	2.96	0.00	1.22	2.63	4.85	0.32	2.58	100	0.63	0.30	0.56	0.14

Table 2.6. Mineral isopleths (mineral compositions) and P - T path coordinates. Isopleths used in determining the minimum peak T are in bold. Min Max T = minimum maximum T reached on the P - T path.

Location	Sample	Isopleths (%)			P - T path coordinates			
		x(g)	x(bi)	z(g)	Min Max T	Peak P	T at solidus	P at solidus
PLV	10-AI-20A	65	38	2.2- 3.2	840	9-11	820	6-7
PLV	10-AI-114B1	69	43	1.9- 2.6	830	8-11	813	6-7
PLV	10-AI-58-3B1	64	41	2.6- 2.9	865	8-11	839	6.1
PLV	10-AI-58-2A	67	42	2.9-3.1	X	X	841	6.5
PLV	10-AI-108F	70	44	2.5	815	8-11	800	6
GAG	HJ-34B	63	31	1.4	865	8-11	850	6.8-8.5
GAG	HJ-57B	55	N/A	5.5- 7.5	880	8-11	860	6.8-8.5
GAG	HJ-58C	65	40	2.4- 3.0	845	8-11	835	6.5-8.5
GAG	HJ-74	73	38	6.9-9.1	850	8-11	820	5-8
GAG	10-AI-76	73	43	4.5- 5.9	840	8-11	840	6-8.5
LBS	354-2-04	74	43	2.9- 3.5	835	8-11	830	6-8
LBS	331-e2-11	62	51	2.3- 4.2	830	9-11	825	6.5-8
LBS	333-2-03	65	39	1.8- 3.1	845	8-11	845	7-8
LBS	216a	53	37	3-4	875	8-11	874	7.2

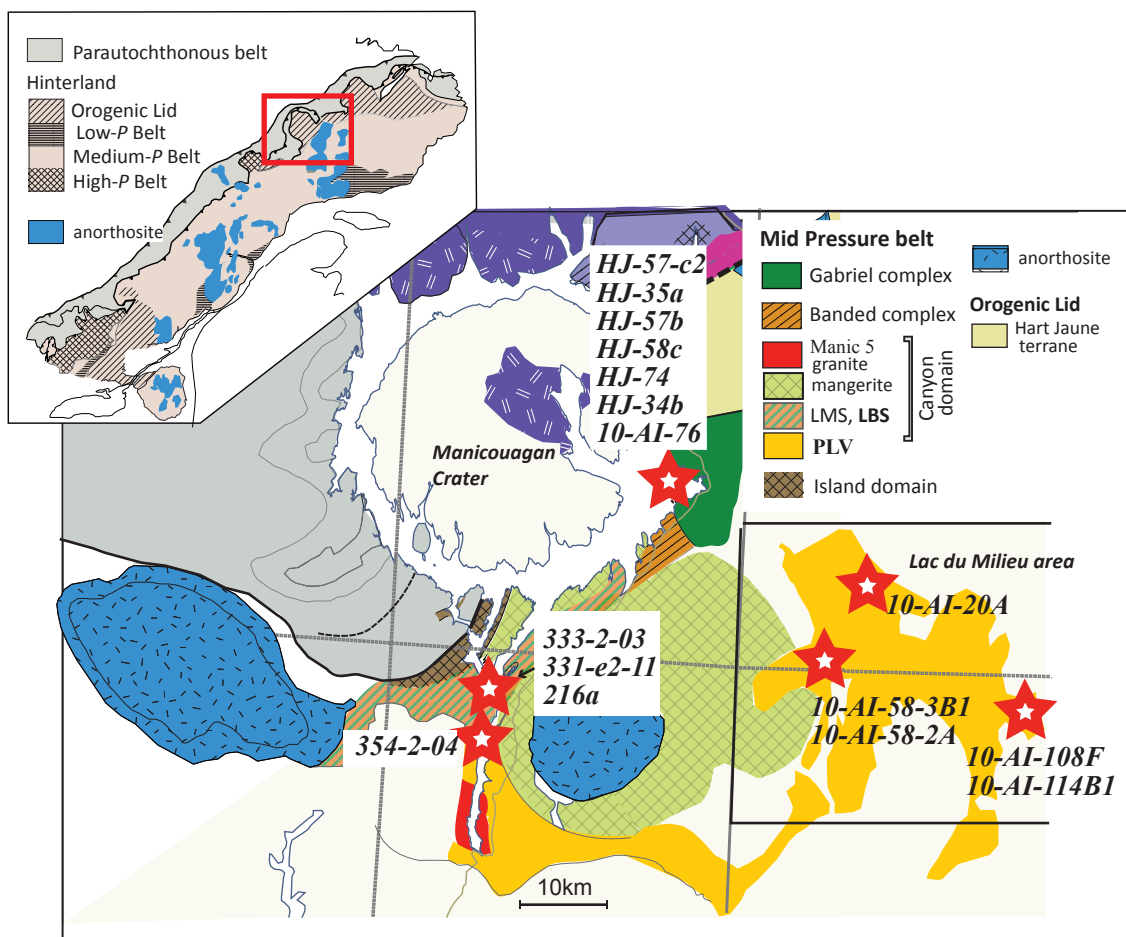


Figure 2.1. Generalized map of the Manicouagan and Lac du Milieu areas showing the locations of the samples. Inset: location of the study area in the Grenville Province.

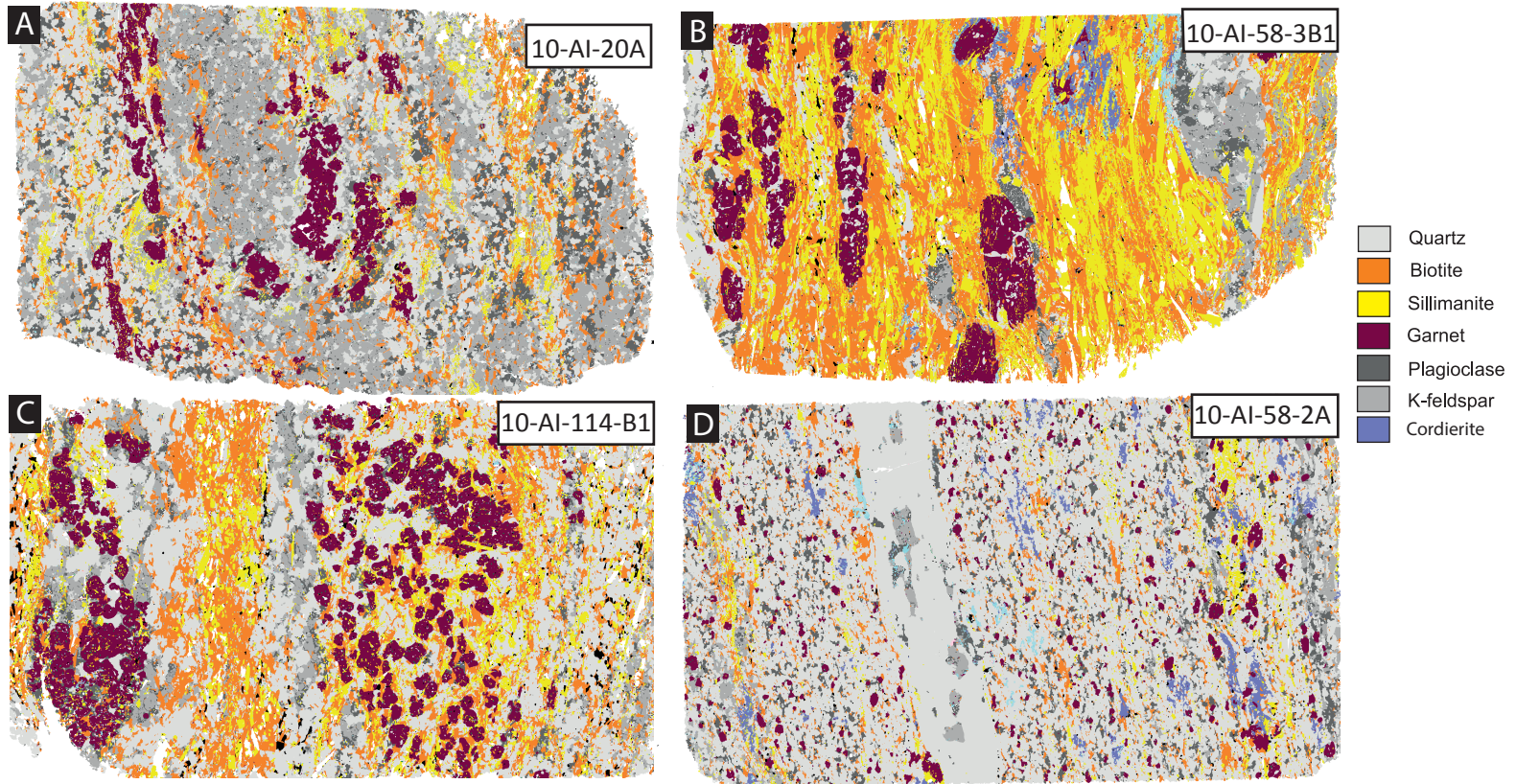


Figure 2.2. SEM-MLA maps for thin sections (46mm length) of aluminous gneisses from the PLV-LM (a) 10-AI-20A; (b) 10-AI-58-3B1; (c) 10-AI-114-B1; and (d) 10-AI-58-2A. Image (a) is from Patrick (2013) and (b-d) from Letourneau (2011).

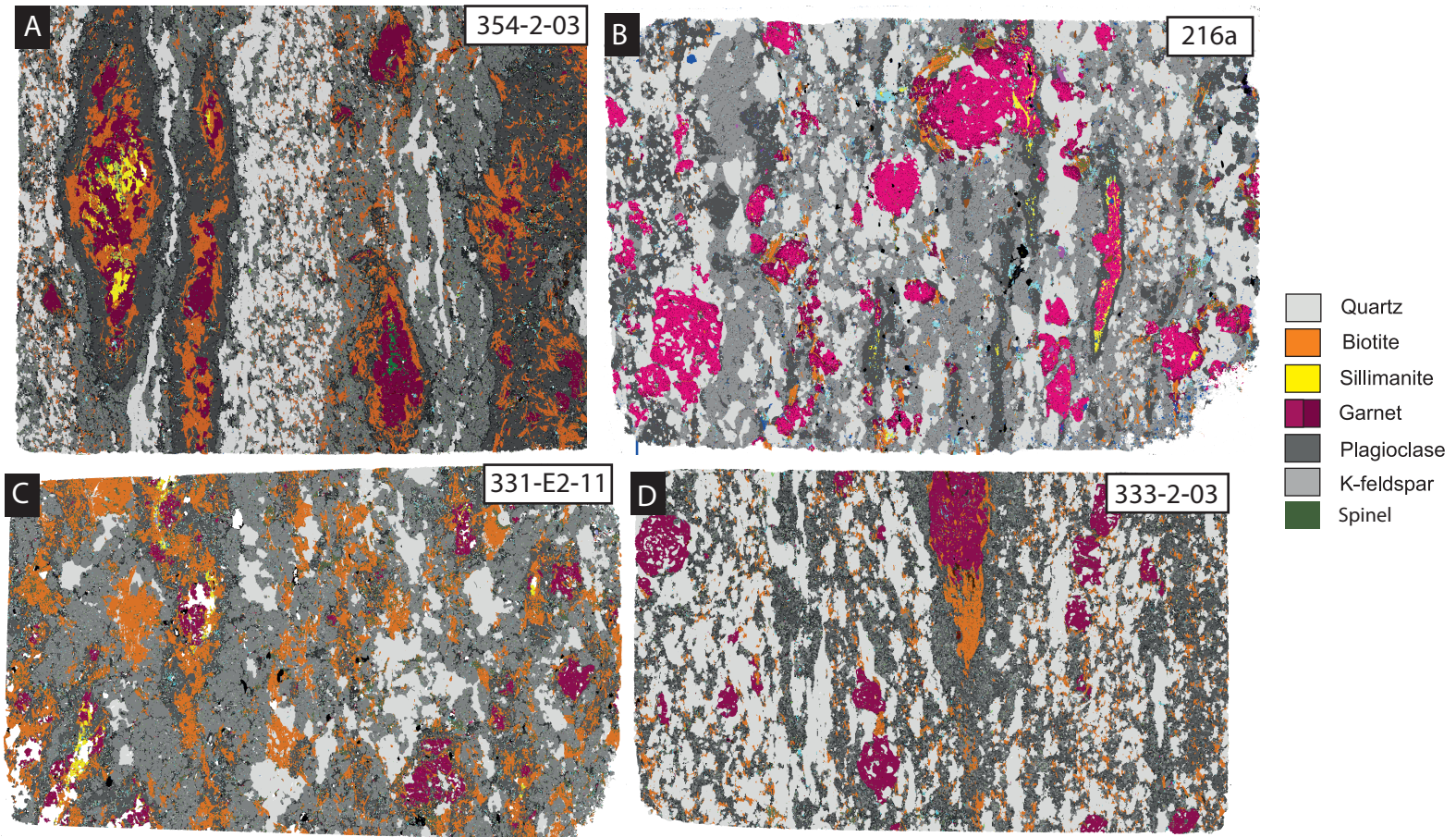


Figure 2.3. SEM-MLA maps of aluminous gneisses from the LBS: (a) 354-2-03; (b) 216a; (c) 331-e2-11; and (d) 333-2-03. Images (a,c,d) are from Hindemith (2013) and (b) is from Lasalle & Indares (2014).

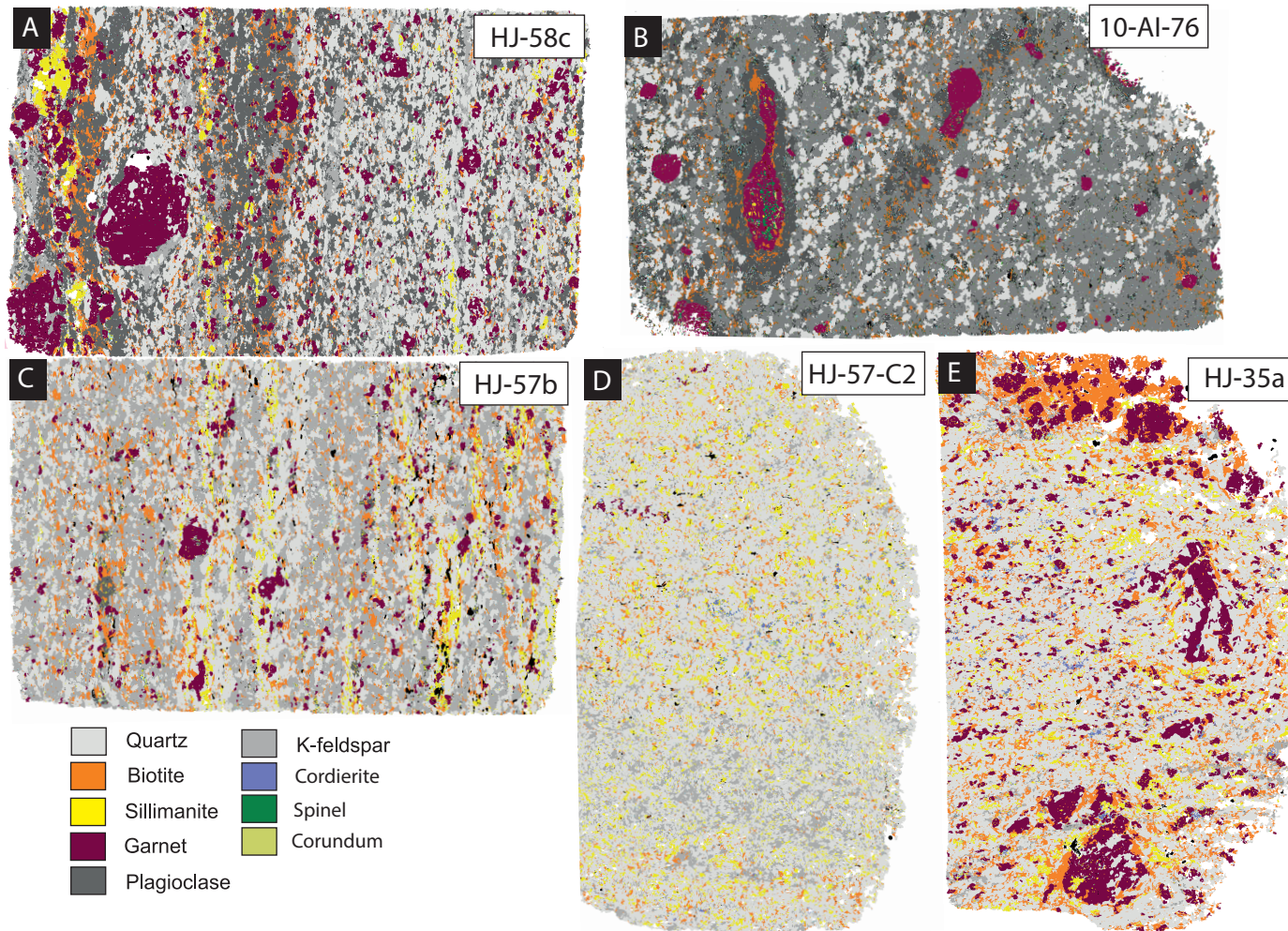
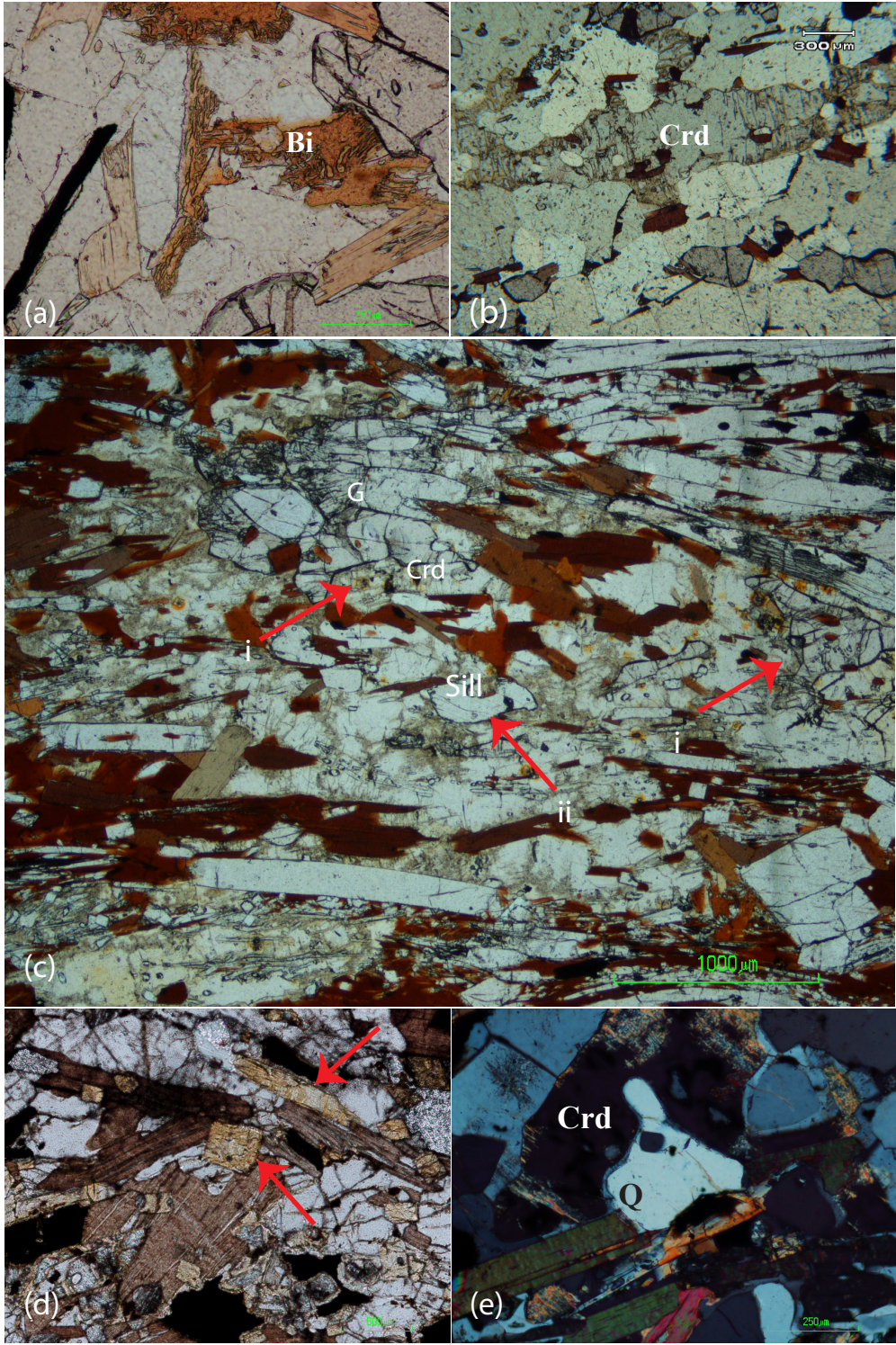


Figure 2.4. SEM-MLA maps of aluminous gneisses from the GAG: (a) HJ-58c; (b) 10-AI-76; (c) HJ-57b; (d) HJ-57-C2; and (e) HJ-35a.



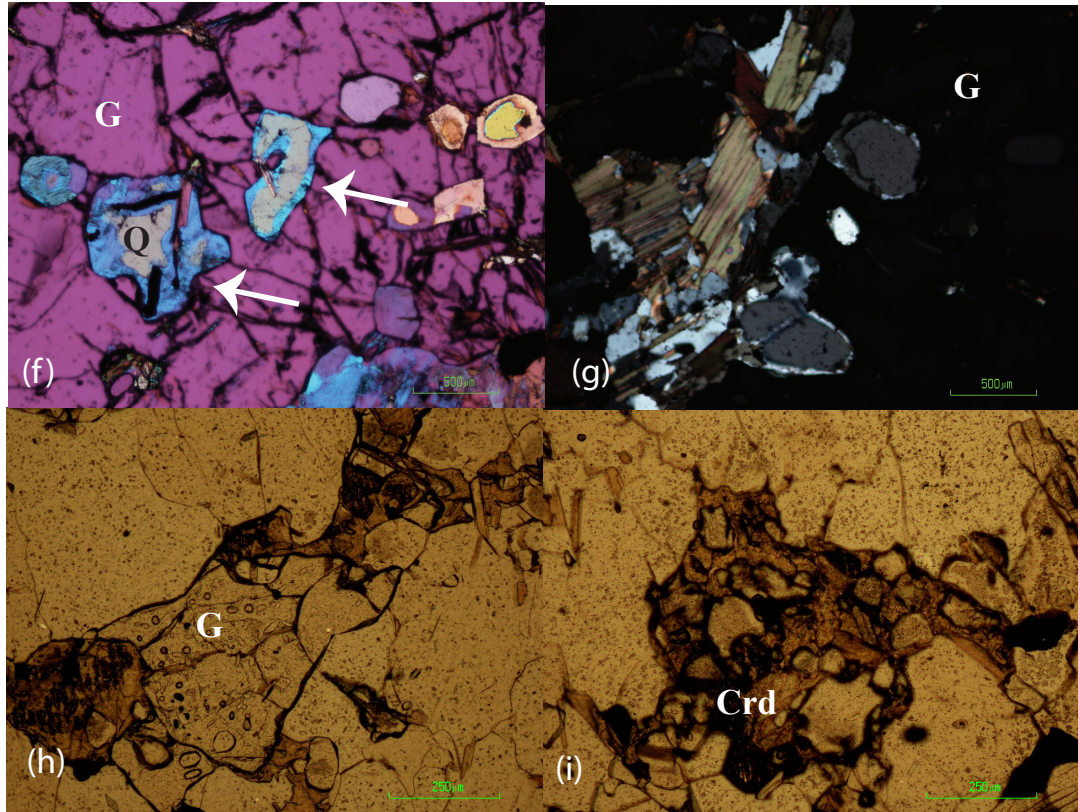
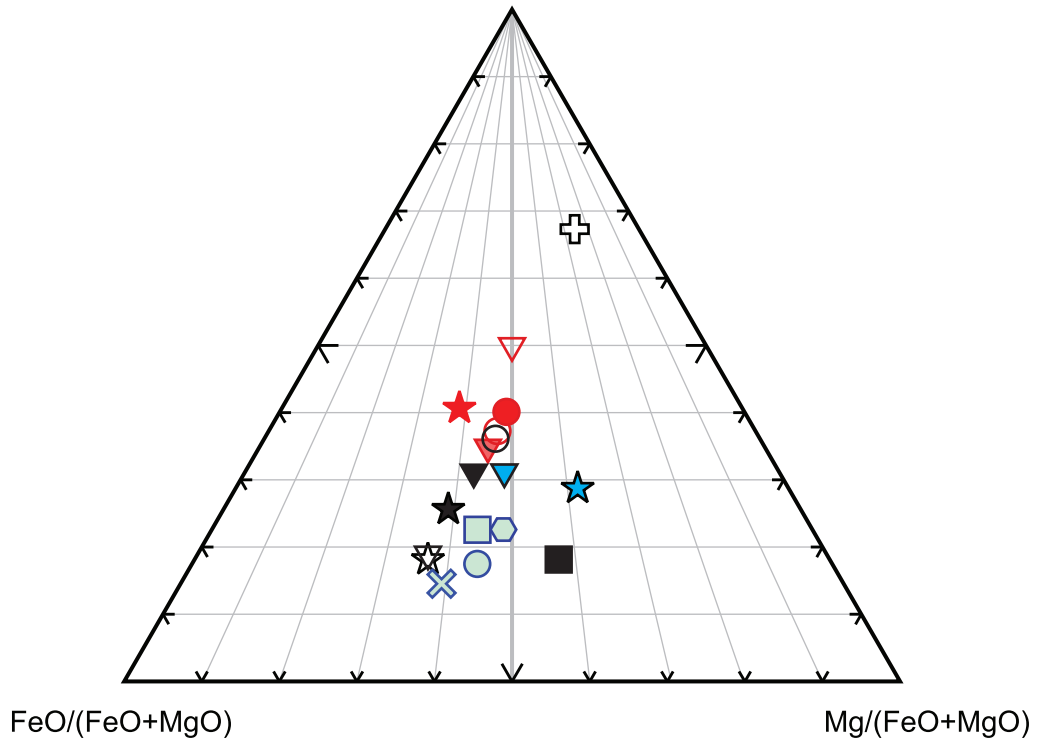


Figure 2.5. Photomicrographs showing characteristic microtextures: (a) biotite-quartz symplectites (10-AI-20A; PLV; PPL); (b) interstitial cordierite in the matrix (10-AI-58-2a; PLV; PPL); (c) cordierite corroding: (i) garnet and (ii) sillimanite (10-AI-58-3B1; PLV; PPL); (d) cordierite pseudomorphing sillimanite prisms(10-AI-58-3B1; PLV; PPL); (e) rounded quartz with thin rims of feldspar in the matrix(10-AI-108F; PLV; XP); (f-g) polyminerallic inclusions in garnet with thin rims of feldspar (331-e2-11; LBS; quartz plate in (f) and XP in (g)); (h) garnet and cordierite relationship (HJ-57-C2; GAG; PPL); and (i) cordierite enclosing matrix minerals (HJ-57-C2; GAG; PPL). PPL: Plane polarized light, XP: Cross polars.

$(\text{Al}_2\text{O}_3\text{-K}_2\text{O-Na}_2\text{O-CaO})/(\text{Al}_2\text{O}_3\text{-K}_2\text{O-Na}_2\text{O-CaO+FeO+MgO})$



PLV-LM

- 10-AI-58-3B1
- 10-AI-20A
- 10-AI-58-2A
- 10-AI-108F
- 10-AI-114B1

- ▽
- ▽
-
-
- ★

GAG

- HJ-34b
- HJ-35a
- HJ-58-C
- HJ-74
- HJ-57B
- HJ-57C2
- 10-AI-76

- ▼
-
- ★
- ▽
-
- +
- ☆

LBS

- 216a
- 331-e2-11
- 333-2-03
- 354-2-04
- 333x
- 216c

-
- ⬡
-
- ×
- ★
- ▼

Figure 2.6. Bulk compositions of the studied samples plotted on an AFM diagram.

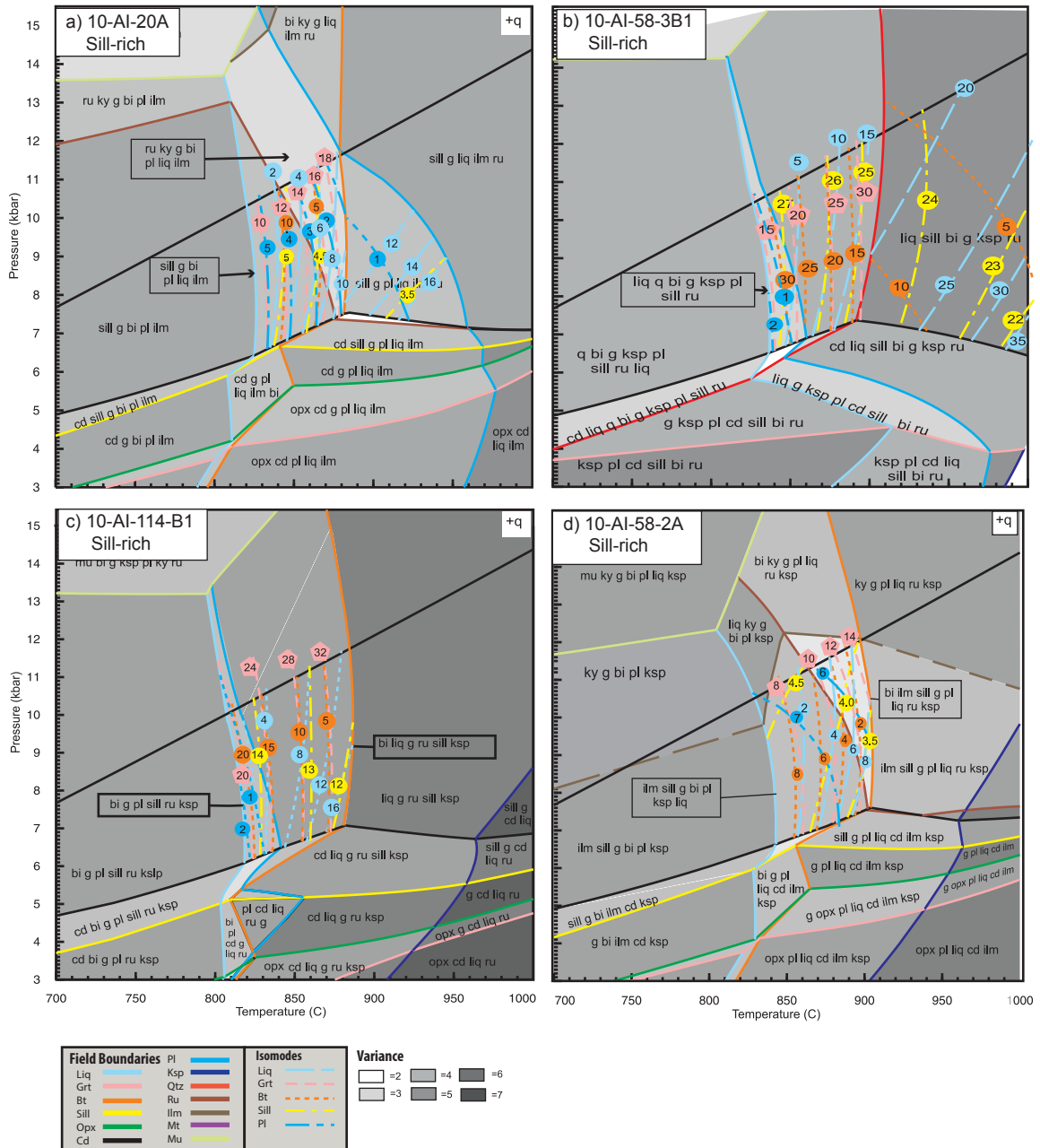


Figure 2.7. *P-T* pseudosections showing the general topologies and relevant isomodes for (a) 10-AI-20A, (b) 10-AI-58-3B1, (c) 10-AI-114-B1 and (d) 10-AI-58-2A from the PLV-LM. Mineral abbreviations: garnet (g); biotite (bi); sillimanite (sill); K-feldspar (ksp); plagioclase (pl); quartz (q); silicate melt (liq); rutile (ru); ilmenite (ilm); cordierite (cd); orthopyroxene (opx); muscovite (mu). Phases in the top right box are stable throughout.

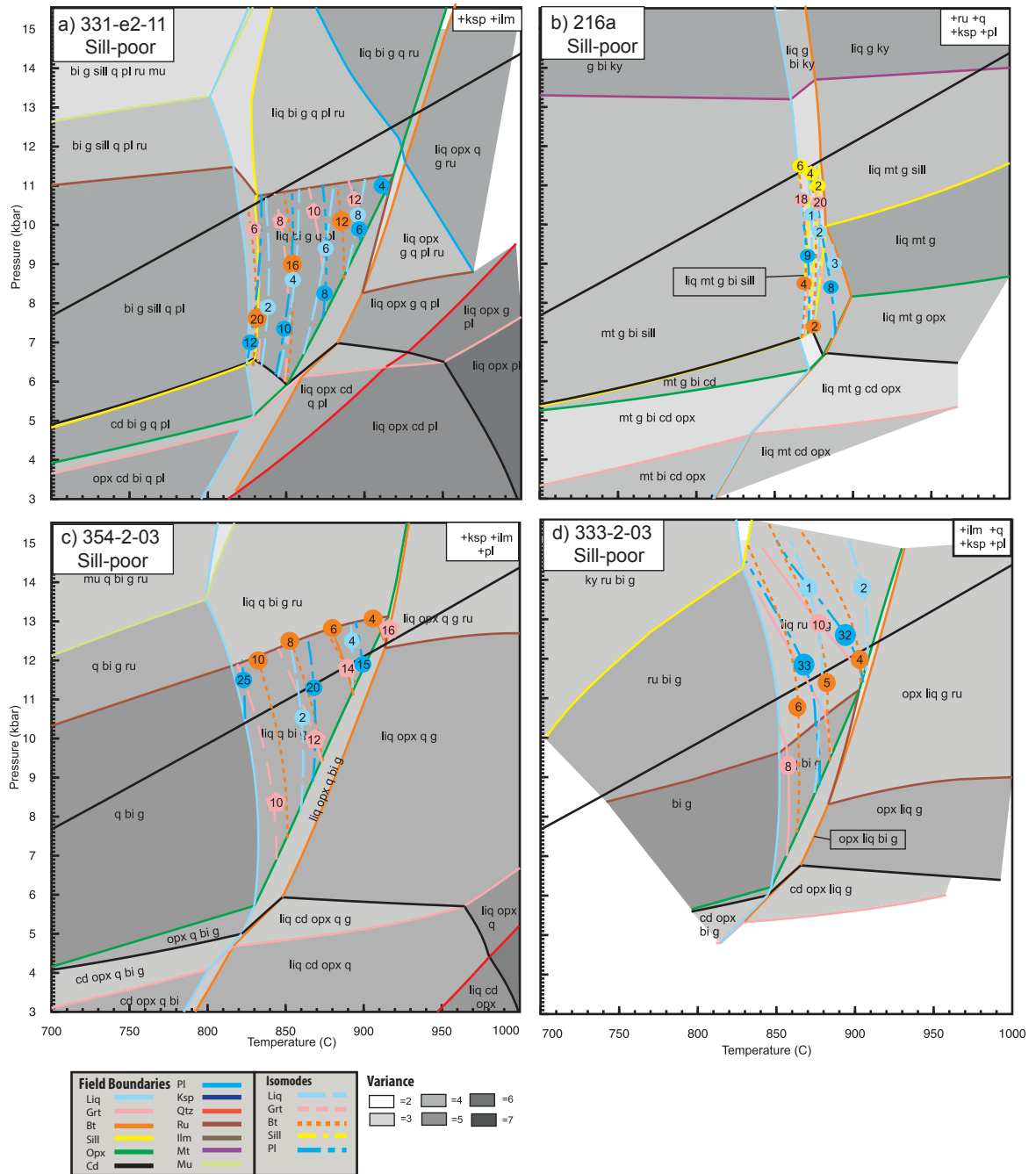


Figure 2.8. *P-T* pseudosections showing the general topologies and relevant isomodes for (a) 331-e2-11, (b) 216a, (c) 354-2-03 and (d) 333-2-03 from the LBS. Phases in the top right box are stable throughout.

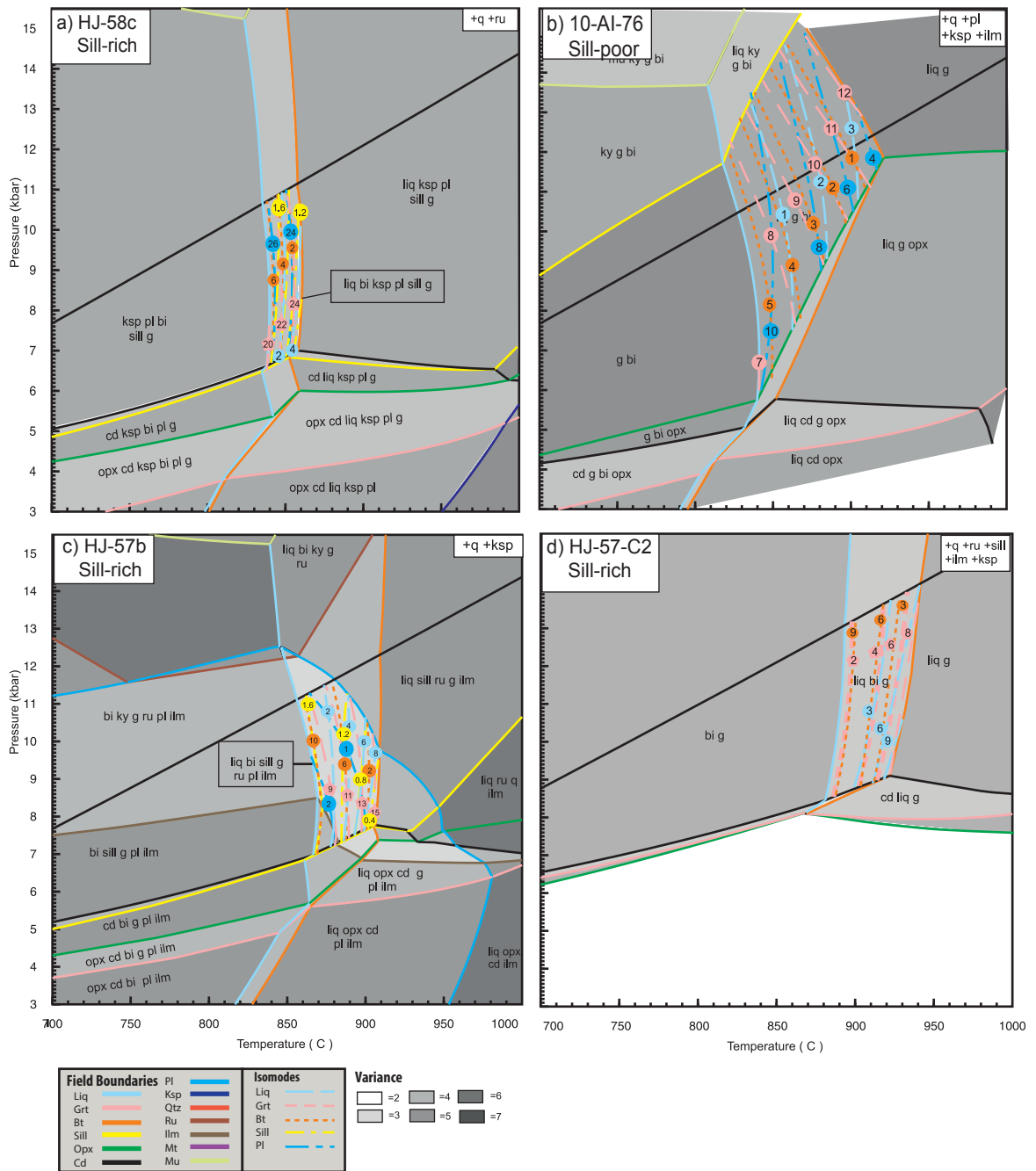


Figure 2.9. P – T pseudosections showing the general topologies and relevant isomodes for (a) HJ-58c, (b) 10-AI-76, (c) HJ-57b and (d) HJ-57-C2 from the GAG. Phases in the top right box are stable throughout.

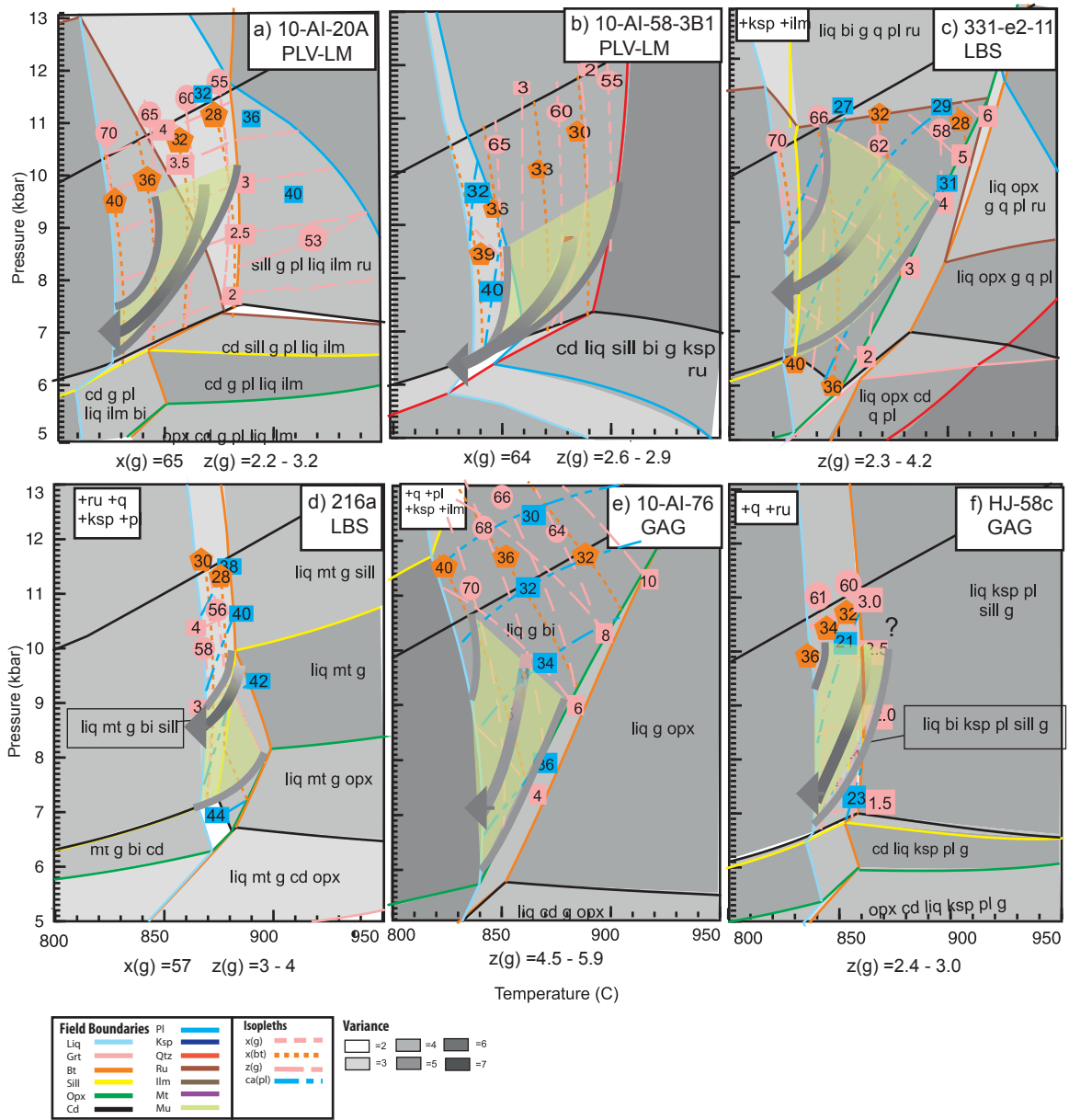


Figure 2.10. Selected P - T pseudosections from Figures 2.7-2.9 with a reduced range showing relevant isopleths (as %) and inferred P - T paths: (a) 10-AI-20A, (b) 10-AI-58-3B1, (c) 331-e2-11, (d) 216a, (e) 10-AI-76 and (f) HJ-58c. Phases in the top right box are stable throughout.

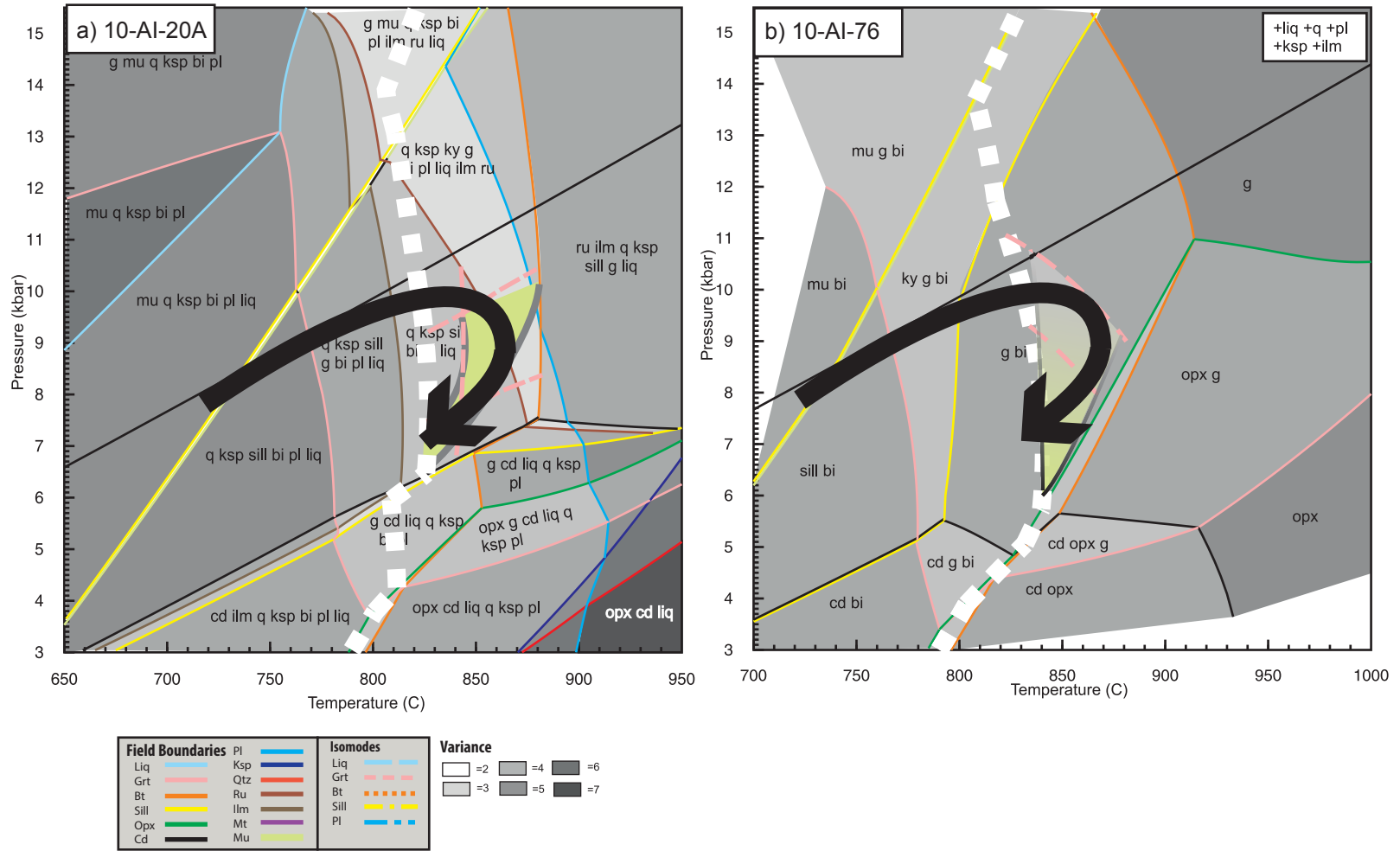


Figure 2.11. Melt reintegrated P – T pseudosections from a sillimanite-rich and sillimanite-poor sample: (a) 10-AI-20A, and (b) 10-AI-76. Phases in the top right box are stable throughout. Thick white dashed lines mark the dry-solidus.

CHAPTER 3: THE INFLUENCE OF Fe^{3+} ON PHASE STABILITY AND P - T PATHS IN MID- P ANATECTIC GNEISSES

ABSTRACT

Phase equilibria modeling in the Na_2O - CaO - K_2O - FeO - MgO - Al_2O_3 - SiO_2 - H_2O - TiO_2 - O (NCKFMASHTO) system is commonly used to infer pressure-temperature (P - T) paths in anatectic aluminous gneisses. This system allows for discrimination between Fe^{2+} and Fe^{3+} , but because conventional analytical techniques do not differentiate between the two, it has been common practice to use an assumed value in the modeling. This study investigates the effect of Fe^{3+} on the phase stability relations in of mid- P anatectic gneisses from the Grenville Province. These rocks have little to no Fe^{3+} bearing minor phases, but they have varying modal abundances of biotite, which is potentially an important contributor to the bulk Fe^{3+} . The study compares P - T pseudosections calculated with the measured Fe^{3+} in biotite (by Mössbauer spectroscopy) with those calculated with different proportions of Fe^{3+} in the bulk composition. The former pseudosections were the most consistent with the rock data, with predicted biotite compositions and stabilities of minor phases comparable to those of the thin section. Increasing bulk Fe^{3+} mainly affected the stability and proportions of minor phases such as ilmenite, rutile and magnetite and produced minor shifts in composition isopleths of ferromagnesian minerals, as well as changes in the Fe^{3+} content of biotite. However, the predicted P - T paths are not significantly affected by such changes.

3.1 INTRODUCTION

Partial melting of aluminous rocks such as metapelites and metagreywackes is characteristic of granulite-facies metamorphic belts and the P - T evolution of these rocks offers insight into both crustal evolution and the generation of crustal melt. The use of phase equilibria modeling has facilitated and expanded investigations of anatectic processes and P - T paths in aluminous systems using P - T diagrams (pseudosections) calculated for specific bulk compositions. Particular aspects relevant to these systems

include the availability of felsic melt models (White *et al.*, 2002), improved activity models for solid phases involved (ex. White *et al.*, 2007), and the ability to take into account the loss of melt (White *et al.*, 2002). Furthermore, the commonly used Na₂O–CaO–K₂O–FeO–MgO–Al₂O₃–SiO₂–H₂O–TiO₂–O (NCKFMASHTO) system, takes into account the two valence states of iron as Fe²⁺ and Fe³⁺. However, most bulk rock chemical data from natural rocks that have been used in modeling have all iron as Fe²⁺, and any bulk Fe³⁺ is generally assumed.

In aluminous gneisses, Fe³⁺ occurs in minor phases such as ilmenite and magnetite, but also in ferromagnesian phases such as biotite, garnet, cordierite and pyroxene. Fe³⁺ cannot be measured directly by microprobe techniques; however, Fe³⁺ contents of most Fe-bearing minerals can be calculated using stoichiometry (Droop, 1987) and are generally low in ferromagnesian silicates (Cesare *et al.*, 2005). Biotite is an exception, because the presence of vacancies in its structure makes the stoichiometric calculation of Fe³⁺ impossible without making several assumptions that cannot be readily verified.

The Fe³⁺ content in biotite can be measured by Mössbauer spectroscopy, and in metapelites it has been found to make up between 0–35% of the total iron, most frequently within 4–16%, where the lowest values are associated with graphitic-bearing assemblages (Ferry and Spear, 1978; Guidotti and Dyar, 1991; Dachs and Berisek, 1995; Dyar *et al.*, 2002; Cesare, 2005). Consequently, biotite may contribute significantly to the Fe³⁺ budget of aluminous rocks.

Most research on the effect of changing the proportion of Fe^{3+} on phase stability in pseudosections of aluminous systems has focused on low- P topologies, within the cordierite stability field, or on ultra-high- T assemblages including sapphirine. For instance, Diener and Powell (2010) used a T - ($\text{Fe}^{3+}/\text{Fe}_{\text{tot}}$) pseudosection for a typical metapelite composition to show how the mineral assemblages change while increasing Fe^{3+} between 450 and 950°C at a constant pressure of 5 kbar. The stability of minerals such as muscovite and plagioclase was shown to be insensitive to changes in $\text{Fe}^{3+}/\text{Fe}_{\text{tot}}$, however, ferromagnesian minerals were affected. For example, the stabilities of garnet, staurolite and orthopyroxene were restricted to relatively reduced conditions, cordierite was stabilized to lower T with increase in Fe^{3+} , and oxide phases changed from ilmenite to magnetite to hematite with an increase in $\text{Fe}^{3+}/\text{Fe}_{\text{tot}}$.

Boger *et al.* (2012) investigated granulite-facies metapelites from the Anosyen domain of Madagascar, where the rocks of three different formations had similar bulk compositions but different oxidation states and mineral assemblages. The most reduced formation had the assemblage Bi–Cd–Sill–Sp–G (list of mineral abbreviations is available on page xii), compared with Sp–G–Cd–Mt in the formation with intermediate composition, and Bi–Sill–Cd–Mt in the most oxidized of the three (additionally, Q–Ilm–Pl–Ksp–Liq was present in all). This shows that Fe^{3+} can have an effect on more than just minor phases, and even on nominally non-ferromagnesian phases, such as sillimanite. The oxidation ratio of each formation was estimated by means of T and P vs. oxidation ratio diagrams by comparing the stability field of a given mineral assemblage. In

addition, the effect of variations in Fe^{3+} on the mineral assemblages was modeled (within the range of 750–1000°C and 4–8 kbar) in each formation.

Additionally, two studies have investigated the role of Fe^{3+} in sapphirine–quartz assemblages of ultrahigh- T metapelites and showed that the assemblages were shifted to lower T in highly oxidized systems. The first study (Taylor-Jones and Powell, 2010) used a T – Fe^{3+} diagram at a constant 7 kbar in the simpler FMASTO system and showed that the stability of sapphirine was shifted from above 1000°C to as low as 930°C with an increase in $x(\text{Fe}^{3+}) = \text{Fe}^{3+}/\text{Fe}_{\text{tot}}$. The results were similar in the NCKFMASHTO system modeled by Korhonen et al. (2012); however, additionally they used a T – M_0 (T vs. $\text{Fe}^{3+}/\text{Fe}_{\text{tot}}$) pseudosection at constant P to identify the bulk Fe^{3+} amount that is most consistent with the observed peak mineral assemblage. This was possible because at ultrahigh- T conditions, and for the modeled bulk compositions, several minerals accommodate Fe^{3+} , and therefore the stability fields of mineral assemblages are narrow and well constrained.

All of the aforementioned previous work has focused on metapelites with complex topologies and several minor phases that accommodate Fe^{3+} (ex. spinel, sapphirine, ilmenite, magnetite). Alternately, in mid- P anatectic aluminous rocks, at P above the cordierite-out line, the topologies are simpler and are mainly represented by a wide P – T field with the assemblage $\text{Liq}+\text{Bi}+\text{G}+\text{Sill}+\text{Ksp}+\text{Q}+\text{Pl}\pm\text{Ilm}\pm\text{Mt}\pm\text{Ru}$. This field corresponds to the dehydration melting of biotite, bounded at low- T and high- T by the solidus and biotite-out phase boundary, respectively. In rocks with low modal

abundances of minor Fe³⁺ bearing phases, biotite may be a large contributor of Fe³⁺ within this field due to the large modal proportion of this mineral in most metapelites and the commonly high proportion of total iron as Fe³⁺ compared with other major minerals (Dyar *et al.*, 2002; Cesare, 2005).

This paper aims to evaluate the effect of Fe³⁺ on the dehydration melting field of biotite in mid-*P* aluminous granulites, using a set of four samples with a wide range of biotite modal proportions, from the central Grenville Province. The following approach was used. (1) First, *P*–*T* pseudosections were calculated with bulk compositions that incorporate Fe³⁺ contents of biotite measured by Mössbauer spectroscopy. (2) Next, all *P*–*T* pseudosections were calculated with the same low value of Fe³⁺ in the bulk, such as what is typically done when there not any constraints on the bulk Fe³⁺. (3) Lastly, the diagrams were recalculated with bulk Fe³⁺ contents derived from different assumed bulk Fe³⁺/Fe_{tot} ratios, calculated by setting 10, 15 and 20% of the total Fe as Fe³⁺ in biotite.

3.2 SAMPLE CHOICE AND DESCRIPTIONS

Four anatectic aluminous gneisses from the mid-*P* hinterland of the central Grenville Province were used in this study; three samples from a metasedimentary sequence (Complexe de la Plus-Value) from the Lac du Milieu area (PLV-LM): 10-AI-20A, 10-AI-114B and 10-AI-58-3B1, and one from a layered bimodal suite (LBS) from the Manicouagan area: 331-e2-11. These rocks are inferred to have acquired their aluminous character, at least in part, by pre-metamorphic hydrothermal alteration of the

protoliths (Letourneau, 2011; Hindemith, 2013), and their setting is described in Chapter 2. The samples contain the mineral assemblage $\text{Bi}+\text{G}+\text{Sill}+\text{Ksp}+\text{Q}\pm\text{Pl}\pm\text{Ilm}$, and were selected based on the range of biotite proportions and the availability of samples from both the sillimanite-rich and sillimanite-poor groups (as defined in Chapter 2).

3.2.1 Petrography

The general distribution of minerals for each sample is illustrated in SEM–MLA false color mineral maps (Figure 3.1; for the technique see Chapter 2), and the mineral modes, also acquired by SEM–MLA, are listed in Table 3.1. Below is a brief description of the each sample.

Sample 10-AI-20A (Figure 3.1a) is medium-grained and consists of diffuse quartzofeldspathic and aluminous ($\text{Bi}+\text{Sill}+\text{G}$) layers. It has a foliation defined by biotite, sillimanite and elongated stringers of ameboidal garnet that overgrow acicular aligned sillimanite. Garnet also contains inclusions of biotite, quartz (swiss cheese appearance; some corroded with rim of feldspar), K-feldspar, as well as polyminerallic inclusions of quartz, biotite and feldspars. Biotite forms aggregates with sillimanite, symplectites with quartz and locally corrodes garnet. This is the biotite-poorest sample.

Sample 10-AI-114-B1 (Figure 3.1b) is medium-grained and consists of quartzofeldspathic, biotite–sillimanite-rich, and garnet-rich layers. Garnet occurs as framboidal grains and in one section of the slide these form a large aggregate. Biotite fills

the spaces between the aggregates. Garnet contains inclusions of sillimanite, quartz and biotite.

Sample 10-AI-58-3B1 (Figure 3.1c) is medium-grained and consists mainly of a biotite–sillimanite matrix, the orientation of which, together with “pancake” shaped garnet, defines a strong foliation. Garnet contains inclusions of sillimanite, biotite and quartz, some of which are polyminerallic and are rimmed by feldspar, and the garnet rims are variably corroded by sillimanite and biotite. This sample is the most rich in biotite (and sillimanite). Quartzofeldspathic minerals are scarce and form aggregates within the biotite–sillimanite matrix; plagioclase rims K-feldspar and garnet. This sample also contains minor cordierite in the form of xenomorphic aggregate patches, which enclose or rim garnet and sillimanite, and garnet has straight faces against it locally.

Sample 331-E2-11 (Figure 3.1d) is the only sillimanite-poor rock in this set. It is fine- to coarse-grained and contains aggregates of aluminous minerals (biotite, sillimanite and garnet) in a quartzofeldspathic matrix. Garnet porphyroblasts frequently display sieve texture, and contains inclusions of biotite and/or sillimanite and/or quartz, commonly rimmed by feldspars and sillimanite. Biotite is quite coarse grained in places, and commonly forms symplectites with quartz, while sillimanite is restricted only to the aluminous aggregates. The matrix is zoned based on the aluminum content of the minerals: plagioclase mantles patches of garnet + biotite + sillimanite, K-feldspar encloses plagioclase, and quartz resides farthest from the patches.

3.2.1.1 Interpretation of Petrography

The textures described earlier suggest that the mineral assemblages stable at metamorphic peak conditions were: G+Sill+Q+Ksp+Bi+Pl in 10-AI-20A, G+Sill+Q+Ksp+Bi in 10-AI-58-3B1 and 10-AI-114B, and G+Q+Ksp+Bi+Pl in 331-E2-11. Plagioclase and cordierite are inferred to be retrograde phases in 10-AI-58-3B1 and 10-AI-114B because they rim and corrode garnet as well as K-feldspar in the case of plagioclase, and sillimanite in the case of cordierite. Sillimanite is considered retrograde in 331-E2-11 because it is only found in sites of garnet replacement.

In addition, pseudomorphed melt has been identified in most samples as thin films of feldspar surrounding corroded relict phases (commonly quartz) and ameboid-shaped or polyminerallic inclusions in garnet. Where garnet exhibits euhedral crystallographic faces into cordierite, it is likely that garnet grew into melt that was later pseudomorphed into cordierite. This suggests that the peak mineral assemblages were stable in the presence of melt.

3.2.2 Mineral Chemistry

The chemical compositions of biotite, garnet, K-feldspar, plagioclase and cordierite are taken from Patrick (2013) and Hindemith (2013). A JEOL JXA-8230 microprobe at Memorial University of Newfoundland was used to determine the composition of ilmenite in 10-AI-58-3B1 with a 15kV accelerating potential, a 20 nA beam current, and a 3 micron spot beam.

Garnet is almandine-rich (Alm: 62.3–76.8%, in 331-E2-11 and 10-AI-114B, respectively), with moderate pyrope contents (17.1–29.6%), and spessartine and grossular make up less than 5% (1–4.8% and 0.1– 3.6%, respectively). There is negligible Fe³⁺ substitution in all. Garnets are chemically homogeneous except for the rims, which are slightly enriched in Fe and Mn relative to the cores. Fe and Mg in garnet are interpreted to have been reset during cooling, however, Ca from the core can be used to infer the *P* of the metamorphic peak (see Chapter 2).

Biotite has $x(\text{Fe}) = \text{Fe}/(\text{Fe} + \text{Mg})$ that ranges from 30.4 to 47.8%, where in 10-AI-20A and 10-AI-114B it contains the least and most $x(\text{Fe})$, respectively. There are two distinct groups of biotite based on composition: those adjacent to garnet have lower $x(\text{Fe})$ than those that are isolated in the matrix. Ilmenite has an average of 1.88% of the total iron as Fe³⁺.

3.2.3 Fe³⁺ contents of biotite

Mössbauer analysis of powdered biotite separates was used to determine the Fe³⁺/Fe_{tot} of biotite (referred to herein as $x(\text{Fe}^{3+})_{\text{bi}}$) by Dr. Catherine McCammon at the Bayerisches Geoinstitut in Bayreuth, Germany. The powders were soaked in benzophenone to reduce the effects of preferred orientation and the spectra were recorded on a constant acceleration Mössbauer spectrometer with a nominal 1.85 GBq ⁵⁷Co source in a 6µm Rh matrix at room temperature. In cases where there was asymmetry between the high- and low-velocity doublets (preferred orientation), the samples were rerun with the holder tilted at 54.7° to the γ-ray direction (Ericsson and Wäppling 1976).

Values for $x(\text{Fe}^{3+})_{\text{bi}}$ were calculated based on relative area ratios, and are generally lower than measurements found in the literature for biotite in metapelites. They are as follows: (1) 0.00–0.04 in 10-AI-20A; (2) 0.02–0.04 in 10-AI-114-B1; (3) 0.02–0.04 in 10-AI-58-3B1; (4) 0.01–0.03 in 331-e2-11.

3.3 PHASE EQUILIBRIA MODELING

The samples were modeled in the NCKFMASHTO system with THERMOCALC 3.33 (Powell and Holland, 1988) using the internally consistent dataset tcds55 (Holland and Powell, 1998), created November 22, 2003. The minerals Q–G–Ksp–Pl–Sill–Bi–Cd–Mu–Ru–Ilm–Mt–Opx were considered in the calculations. The following a–x models were used: garnet (g: White et al., 2007), biotite (bi: White et al., 2007), cordierite (cd: Holland and Powell, 1998), muscovite (mu: Coggon and Holland, 2002), plagioclase and K-feldspar (pl, ksp: Holland and Powell, 2003), orthopyroxene (opx: White et al., 2002), magnetite (mt: White et al., 2002), ilmenite (ilm: White et al., 2000) and melt (liq: White et al., 2007). The bulk compositions used (see Table 3.2), were taken from chapter 2. In addition, for the NCKFMASHTO system, Thermocalc requires input of a value for O, which accounts for the portion of Fe^{3+} in the bulk Fe.

A first set of P – T pseudosections was calculated with the ‘real’ O value determined by the measured $x(\text{Fe}^{3+})_{\text{bi}}$ for each sample. Next, a second set of pseudosections was calculated with $O = 0.05$, the minimum value that was used for all samples in Chapter 2. Lastly, the diagrams are recalculated with higher O values

corresponding to the proportion of bulk Fe^{3+} needed to make up 10%, 15% and 20% of $x(\text{Fe}^{3+})_{\text{bi}}$.

In each P – T pseudosection, the $\text{Fe}^{3+}/\text{Fe}_{\text{tot}}$ in biotite predicted by Thermocalc (referred to from here on as predicted $x(\text{Fe}^{3+})_{\text{bi}}$) was calculated at several P – T points of interest. This was done using the $x(\text{bi})$, $f(\text{bi})$, $y(\text{bi})$, $t(\text{bi})$ and $Q(\text{bi})$ parameters produced by Thermocalc at these points, and the equations of White et al. (2007) and Tajkmanova et al. (2009). Also listed within these references are the definitions of $x(\text{bi})$, $f(\text{bi})$, $y(\text{bi})$, $t(\text{bi})$ and $Q(\text{bi})$. Two different methods were used to calculate the proportion of Fe^{3+} in biotite and the same results were obtained in each; an example of the calculation using one method is provided in the Appendix.

For each set of pseudosections, the P – T coordinates and modal abundances of the minerals ilmenite, rutile, magnetite and biotite at the P – T points of interest were also recorded. In addition, calculated mineral composition isopleths corresponding to the measured mineral composition parameters ($x(\text{g}) = \text{Fe}/(\text{Mg}+\text{Fe})$ in garnet and $x(\text{bi}) = \text{Fe}/(\text{Fe}+\text{Mg})$ in biotite) in the rocks were compared between the different sets of P – T pseudosections, because these are important for P – T path inferences (see chapter 2). All this information is shown in Tables 3.3 and 3.4

3.3.1 Phase equilibria diagrams calculated with measured $x(\text{Fe}^{3+})_{\text{bi}}$

The $x(\text{Fe}^{3+})_{\text{bi}}$ was measured in each of the samples as a range. For this reason, a pseudosection was calculated for both the average and the upper limit of $x(\text{Fe}^{3+})_{\text{bi}}$. Pseudosections with the average values of each sample are shown in Figure 3.2 (and upper value pseudosections are available in Appendix D).

3.3.1.1 General topologies

All P – T pseudosections show the stability field of the inferred peak mineral assemblage $\text{Liq}+\text{Bi}+\text{G}+\text{Ksp}+\text{Q}\pm\text{Sill}\pm\text{Pl}\pm\text{Ilm}\pm\text{Ru}$ (Field I; Figure 3.2a)). For the sill-rich samples (Figure 3.2a–c) this field is bounded on the low- P side by the appearance of cordierite, on the low- T side by the solidus, and on the upper- T side by the disappearance of biotite. Because sillimanite is the only Al-silicate stable in the samples, this field is bound on the upper- P side by the kyanite–sillimanite transition line. The pseudosection topologies for 10-AI-114B and 10-AI-58-3B1 lose plagioclase half way through Field I with increasing T . For the sill-poor sample 331-e2-11 (Figure 3.2d), there is no sillimanite stable in the pseudosection, and Field I is bound on the upper- T side by the orthopyroxene-in phase boundary.

Low- P topologies are controlled by shallow dP/dT gradient field boundaries. With decreasing P , these include cordierite-in→sillimanite-out→orthopyroxene-in→garnet-out; however, the pseudosection for 10-AI-58-3B1 (Figure 3.2c) does not see the loss of sillimanite or appearance of orthopyroxene. On the high- P , low- T corner, each diagram has a field where muscovite is stable. The higher- T side of each pseudosection sees the loss of a feldspar: pseudosections for 10-AI-20A and 331-e2-11 lose plagioclase

(Figures 3.2a,d), whereas 10-AI-114B and 10-AI-58-3B1 lose K-feldspar (Figures 3.2b,c; plagioclase was lost already at lower- T within Field I).

The pseudosection for 10-AI-58-3B1 is unique in that the biotite-out phase boundary occurs at a much higher T ($>1000^{\circ}\text{C}$), and quartz is lost before biotite (Figure 3.2c). Quartz is a reactant in biotite dehydration melting reactions, and because of its low modal proportion (12.54%) compared with that of biotite (34.85%), it was exhausted first, explaining the stabilization of biotite to much higher T . The pseudosections calculated with the average and upper $x(\text{Fe}^{3+})_{\text{bi}}$ values are very similar (shown in Figure 3.2. and in appendix D, respectively).

3.3.2 Role of varying the bulk $\text{Fe}^{3+}/\text{Fe}_{\text{tot}}$ on the pseudosection topologies and on the predicted $x(\text{Fe}^{3+})_{\text{bi}}$

This section compares P - T pseudosections calculated with $O=0.05$ (as was done in Chapter 2) and with O values corresponding to 10, 15 and 20% $x(\text{Fe}^{3+})_{\text{bi}}$ (to be referred to as 10%, 15% and 20% diagrams). Figures 3.3–3.6 show the P - T pseudosections calculated with $O=0.05$, and with 10% and 20% $x(\text{Fe}^{3+})_{\text{bi}}$, for each sample (the pseudosections for 15% are available in Appendix D). Those with $O=0.05$ were used to interpret the textures and mineral chemistry of the rocks in terms of P - T paths in Chapter 2. The methods used to calculate them are available therein.

For all samples, the greatest change in the pseudosections occurs between the $O=0.05$ and 10% diagrams. In most cases this change is manifested by the appearance of a new minor phase, such as ilmenite, and by a shifting of rutile stability. In addition, in

the case of the sillimanite-poor sample 331-e2-11, sillimanite becomes stable in a narrow field to the higher- T side of the solidus, with increasing bulk $\text{Fe}^{3+}/\text{Fe}_{\text{tot}}$. The differences with increases in the Fe^{3+} content of the bulk for each sample are discussed in full below.

3.3.2.1 Sample 10-AI-20A

Sample 10-AI-20a is the poorest in biotite. The pseudosection shows that with an increase in the proportion of $\text{Fe}^{3+}/\text{Fe}_{\text{tot}}$ in its bulk composition, the stability of minor phases within Field I changes (Figure 3.3). At $O=0.05$, ilmenite is stable throughout the entire range, but in the 10–20% diagrams, magnetite is stable instead. In all cases rutile is stable on the upper P side of the diagram, cross-cutting Field I; however, rutile stability is shifted to higher P with an increase in bulk $\text{Fe}^{3+}/\text{Fe}_{\text{tot}}$. The modal abundance of magnetite increases between the 10 and 20% diagrams; for example, at the biotite-cordierite point, it increases from 0.28 to 0.67%. Rutile abundance decreases slightly with increase in bulk Fe^{3+} content, and biotite remains approximately the same.

With an increase in bulk $\text{Fe}^{3+}/\text{Fe}_{\text{tot}}$, the phase boundaries that surround Field I are shifted slightly; the solidus and biotite-out boundary are shifted a few degrees up- T and the cordierite-in phase boundary is shifted up- P (Table 3.4). The isopleths of $x(\text{bi})$ are displaced to lower T between the 10 and 20% diagrams ($842.2 \rightarrow 836.9$ °C at 9 kbar); however, the lowest $x(\text{bi})$ T is in the $O=0.05$ pseudosections, at 835.8°C.

In general, the predicted $x(\text{Fe}^{3+})_{\text{bi}}$ increases with T across Field I of each pseudosection; it also increases with increased bulk Fe^{3+} . Finally, although the bulk composition was calculated based on 10, 15 or 20% $x(\text{Fe}^{3+})_{\text{bi}}$, Thermocalc did not

actually predict that amount for biotite at any point, with the exception of the 10% diagram, where the upper limit of the biotite phase boundary has 10.1% predicted $x(\text{Fe}^{3+})_{\text{bi}}$. For the P - T path (in $O=0.05$ pseudosection only), the predicted $x(\text{Fe}^{3+})_{\text{bi}}$ was the highest at the peak (3.8–6.5) and dropped to 3.6 where it crosses the solidus.

3.3.2.2 Sample 10-AI-114-B1

In the pseudosections of sample 10-AI-114-B1 (Figure 3.4), with an increase in the proportion of bulk $\text{Fe}^{3+}/\text{Fe}_{\text{tot}}$, the stabilities of minor phases within Field I change. At $O=0.05$, only rutile is stable throughout. With higher bulk $\text{Fe}^{3+}/\text{Fe}_{\text{tot}}$, ilmenite is stable throughout and rutile is stable on the upper P side of the diagram, cross-cutting Field I. However, rutile stability is increasingly shifted to higher P . With an increase in the bulk $\text{Fe}^{3+}/\text{Fe}_{\text{tot}}$, the modal abundance of ilmenite increases, rutile decreases and biotite decrease very slightly, except for where it coexists with rutile, where it decreases more significantly.

With an increase in the bulk $\text{Fe}^{3+}/\text{Fe}_{\text{tot}}$ the phase boundaries that surround Field I are shifted: the solidus down- T , the biotite-out line up- T , and the cordierite-in phase boundary slightly up- P (Table 3.4). The isopleths of $x(\text{g})$ and $x(\text{bi})$ are displaced towards lower T from 838.4 to 826.2 °C, and 821 to 811.4 °C (at 9kbar), respectively.

The predicted $x(\text{Fe}^{3+})_{\text{bi}}$ increases with T across Field I of each pseudosection. It also increases at each point between diagrams with increasing bulk $\text{Fe}^{3+}/\text{Fe}_{\text{tot}}$ with the

exception of in the lowest Fe^{3+} diagram ($O=0.05$ diagram), where the predicted $x(\text{Fe}^{3+})_{\text{bi}}$ along the biotite-out line is 8.0–8.3 compared with 5.0–5.6 along the same line in the highest Fe^{3+} diagram (20% diagram; ilmenite is stable in 10-20% diagrams but not in $O=0.05$). For the P – T path, predicted $x(\text{Fe}^{3+})_{\text{bi}}$ is the highest at the peak, (3.4–5.4) and drops to 2.6 at the solidus.

3.3.2.3 Sample 10-AI-58-3B1

Sample 10-AI-58-B1 is the richest in biotite. In its pseudosections (Figure 3.5), the stabilities of the minor phases within Field I change in the same way as for those of sample 10-AI-114-B1. With an increase in the bulk $\text{Fe}^{3+}/\text{Fe}_{\text{tot}}$, phase boundaries that surround Field I are shifted: the solidus up- T , the biotite-out line down- T (ex. 1060.4 \rightarrow 1048 $^{\circ}\text{C}$ at the biotite–cordierite point), and the cordierite-in phase boundary slightly up- P . The isopleths of $x(\text{g})$ are displaced to lower T from 853.1 to 846.5 $^{\circ}\text{C}$ (at 9kbar), and the $x(\text{bi})$ isopleths are not considered because they fall outside of the field of interest, probably owing to extensive resetting during retrogression.

The predicted $x(\text{Fe}^{3+})_{\text{bi}}$ increases with T across Field I of each pseudosection. It also increases at each point with increasing bulk $\text{Fe}^{3+}/\text{Fe}_{\text{tot}}$, except for the cordierite–biotite point in the $O=0.05$ pseudosection, in which it is 9.2 compared to 7.6 in the 20% diagram. For the P – T path, the predicted $x(\text{Fe}^{3+})_{\text{bi}}$ is the highest at the peak, 2.6–5.1 and drops to 2.0 where it crosses the solidus.

3.3.2.4 Sample 331-E2-11

For the sillimanite-poor sample 331-E2-11, there is one major difference between the $O=0.05$ and the higher bulk Fe^{3+}/Fe_{tot} diagrams: sillimanite is stable at near-solidus conditions in the later diagrams, but not at $O=0.05$. The minor phases within Field I of the diagram change in the same way as in the case of 10-AI-114B and 10-AI-58-3B1: rutile only stable at $O=0.05$ and rutile and ilmenite in the higher bulk Fe^{3+}/Fe_{tot} diagrams, where rutile stability decreases to higher P (11.28 \rightarrow 12.01 kbar at the rutile–orthopyroxene point).

With an increase in the bulk Fe^{3+}/Fe_{tot} , phase boundaries that surround Field I are shifted: the solidus a few degrees up- T , the orthopyroxene-in phase boundary up- T (ex. 841 \rightarrow 857 °C at the orthopyroxene-cordierite point), and the cordierite-in phase boundary up- P significantly (ex. 5.69 \rightarrow 6.52 kbar at the solidus–cordierite point). However, it is between the first two diagrams where the greatest difference is observed, in the near-solidus area where sillimanite becomes stable. The $x(bi)$ and $x(g)$ isopleths are not considered as they fall outside of the field of interest with the exception of the $O=0.05$ diagram, where the $x(g)$ isopleth is located just up- T from the solidus ($\sim 830^\circ\text{C}$).

The predicted $x(Fe^{3+})_{bi}$ increases with T across Field I in each pseudosection; it also increases with P to a lesser extent. With increase in the bulk Fe^{3+}/Fe_{tot} , the predicted $x(Fe^{3+})_{bi}$ increases at each point, between diagrams, with the increase being most

significant at the rutile-in boundary, where present. For the P - T path, predicted $x(\text{Fe}^{3+})_{\text{bi}}$ is the highest at the peak, 3.3, and drops to 2.9 where it crosses the solidus.

3.4 DISCUSSION

3.4.1 Pseudosections using the measured $x(\text{Fe}^{3+})_{\text{bi}}$

The pseudosections calculated using the measured $x(\text{Fe}^{3+})_{\text{bi}}$ are broadly consistent with the observed mineralogy. The rocks have little or no minor phases, no rutile or ilmenite except in 10-AI-58-3B1 where there is 0.05 modal percent of ilmenite. The pseudosections of all samples except 10-AI-20A have rutile stable at the solidus, but in very low quantities (ex. 0.079 modal % in 10-AI-114-B1) so it is possible that it did not form.

The predicted values of $x(\text{Fe}^{3+})_{\text{bi}}$ at the solidus (1.3–2.8%) fall within the range of the average measured ones (0–4%). The values from the solidus are the most appropriate for comparison here because there are no further chemical adjustments expected after the solidification of melt (except where garnet and biotite are in direct contact). The predicted $x(\text{Fe}^{3+})_{\text{bi}}$ is fairly consistent along the entire length of solidus segment that bounds Field I in each pseudosection so no matter at what P the melt solidified, the composition of biotite should be similar.

The samples used in this study have low ratios of $x(\text{Fe}^{3+})_{\text{bi}}$ compared to those measured in the literature, and there were also little or no minor phases containing Fe^{3+}

(0.05 modal percent of ilmenite in 10-AI-58-3B1). Therefore, the low O value estimates that are often used in pseudosections (ex. O=0.05 like the low common value pseudosection used in this study) are appropriate for these samples. If the samples had higher measured $x(\text{Fe}^{3+})_{\text{bi}}$, or a higher modal percentage of Fe^{3+} minor phases, then it is probable that the grossly underestimated Fe^{3+} in the bulk used in most pseudosection calculations would cause complications. For example, there would not be enough Fe^{3+} in the bulk to stabilize both the Fe^{3+} minor phases and biotite even though the thin section may show they are part of the peak assemblage. Thermocalc may allow one phase to be stable but not another, and based on the observations during this study, biotite is stabilized first. Additionally, if mineral compositions are of importance in the study, Fe^{3+} would be underestimated.

3.4.2 Effects of increasing the $\text{Fe}^{3+}/\text{Fe}_{\text{tot}}$ in the bulk composition

With an increase in $\text{Fe}^{3+}/\text{Fe}_{\text{tot}}$ of the bulk, there are several slight changes in the pseudosections, within the P - T field of interest:

- 1. Changes in topologies.** With one exception, it is only minor phases that are affected by increases in the bulk $\text{Fe}^{3+}/\text{Fe}_{\text{tot}}$. Rutile is present even in diagrams with the lowest bulk $\text{Fe}^{3+}/\text{Fe}_{\text{tot}}$ because it does not contain any iron. However, there is a link between rutile and the other minor phases present because its modal proportion and P - T stability are changed based on the presence of other accessory phases, or biotite.

Ilmenite (FeTiO_3) (or magnetite (Fe_3O_4) in 10-AI-20A at higher Fe^{3+}) is stable with rutile when $\text{Fe}^{3+}/\text{Fe}_{\text{tot}}$ is higher in the bulk. Both of these phases accommodate Fe^{3+} in their structure, where the former accommodates a few percent of ferric iron as a substitution, and the later is made of a 1:1 ratio of FeO and Fe_2O_3 , therefore magnetite is indicative of a relatively higher oxidation state. Hematite (Fe_2O_3) was not observed in any of the samples or within the mineral assemblages in the pseudosections as this minor phase is found in only the most oxidized conditions, since all its iron is ferric.

There is only one case where a major phase was affected by changes in bulk $\text{Fe}^{3+}/\text{Fe}_{\text{tot}}$. This is for the bulk composition of the sillimanite-poor sample 331-e2-11, where sillimanite is not stable anywhere in the lowest bulk $\text{Fe}^{3+}/\text{Fe}_{\text{tot}}$ pseudosection, but becomes stable in Field I at near solidus conditions in all the higher bulk $\text{Fe}^{3+}/\text{Fe}_{\text{tot}}$ diagrams.

2. Small shifts in phase boundaries. The solidus increases 2–5 °C with an increase in bulk $\text{Fe}^{3+}/\text{Fe}_{\text{tot}}$ in all cases except for 10-AI-114B. This may be related to the fact that the modal proportion of biotite decreases with an increase bulk $\text{Fe}^{3+}/\text{Fe}_{\text{tot}}$, and since there is less water available from biotite, a higher T is required for melting.

For each sample, the biotite-out phase boundary is shifted up T 3–4°C with increase in bulk $\text{Fe}^{3+}/\text{Fe}_{\text{tot}}$, possibly as a result of the concomitant decrease in the bulk $x(\text{Fe})=\text{Fe}^{2+}/(\text{Fe}^{2+}+\text{Mg}^{2+})$, which would stabilize biotite to higher T . This is with the exception of sample 10-AI-58-3B1, where the biotite-out line was shifted down to 996°C from 1022°C at the cordierite-biotite intersection. However, this is unique amongst our

samples and is due to the exhaustion of the reactants quartz and plagioclase of the biotite dehydration melting equation before biotite, and therefore melting must have occurred by another reaction.

The stability of cordierite is increased to higher P with an increase in bulk $\text{Fe}^{3+}/\text{Fe}_{\text{tot}}$ in all cases by an average 0.2 kbar between the diagrams from the two extremes, except for the bulk composition of the sill-poor sample 331-e2-11, where it is shifted up $P \sim 0.9$ kbar when sillimanite is added to the assemblage between the $\text{O}=0.05$ and 10% diagrams. This increase is the result of a reduction in the whole rock $x(\text{Fe})$, as higher $x(\text{Mg})$ increases cordierites stability (Spear *et al.*, 1999). As a result of these shifts in phase boundaries, the entire field containing the main mineral assemblage is shifted up T and P slightly. The effect is that rock melting is modeled to start and end at higher T .

3. Shifts in measured rock isopleths. Isopleths of $x(\text{g})$ and $x(\text{bi})$ are shifted down T 2–5°C for the same reason as shifts in phase boundaries: as more of the total Fe is being allotted as Fe^{3+} , the whole rock $x(\text{Fe})$ is decreased.

4. Changes in modal proportions of phases. With increasing bulk $\text{Fe}^{3+}/\text{Fe}_{\text{tot}}$, ilmenite and magnetite (in 10-AI-20A only) modal abundances increase moderately (Mt doubled in abundance between the 10 and 20% diagrams), whereas rutile abundance decrease slightly. Although rutile does not contain any Fe^{3+} , it shares Ti with biotite and ilmenite; therefore as ilmenite abundance increases because of Fe^{3+} increase, the remaining Ti available for rutile decreases. Biotite abundance decreased very slightly as well with an

increase in O when in the presence of other minor phases, markedly rutile and ilmenite; these are also linked by sharing of Fe^{3+} and Ti between the phases.

5. Changes in the composition of biotite: predicted $x(\text{Fe}^{3+})_{\text{bi}}$. In general, the predicted $x(\text{Fe}^{3+})_{\text{bi}}$ tends to increase with T across each pseudosection. Isomodes of biotite are displaced to lower T across Field I (not shown in this paper, see Patrick, 2013), so it makes sense that as biotite abundance decreases, the proportion of Fe^{3+} that makes up biotite should increase. This is of course as long as the minor phases that also accommodate Fe^{3+} do not change significantly in abundance across the diagram as well.

For the phase equilibria diagrams where the bulk $\text{Fe}^{3+}/\text{Fe}_{\text{tot}}$ was calculated to be 10, 15 or 20% of iron as $x(\text{Fe}^{3+})_{\text{bi}}$, the program did not actually predict that amount in biotite. Instead, the predicted $x(\text{Fe}^{3+})_{\text{bi}}$ ranged from 2–8%, even in diagrams with the highest bulk $\text{Fe}^{3+}/\text{Fe}_{\text{tot}}$. Nowhere within the field of the main mineral assemblage did biotite reach the calculated amount other than along the biotite phase boundary. Since biotite is at zero modal proportion along this line, biotite does not actually contain this amount of Fe^{3+} ; the biotite-out phase boundary gives more of an upper limit of $x(\text{Fe}^{3+})_{\text{bi}}$.

As expected, with an increase in $\text{Fe}^{3+}/\text{Fe}_{\text{tot}}$ in the bulk composition, the amount of Fe^{3+} that Thermocalc assigned to biotite increased at each point in the diagram; however, it did not increase proportionally with the increase of the bulk $\text{Fe}^{3+}/\text{Fe}_{\text{tot}}$. For example, in the pseudosections of the sillimanite-poor sample 331-e2-11, the predicted $x(\text{Fe}^{3+})_{\text{bi}}$ at the cordierite–liquid point increased only 3.2 to 3.8 between the 10 and 20% diagrams. A twofold increase in Fe^{3+} only produced a slight increase in the predicted $x(\text{Fe}^{3+})_{\text{bi}}$. This is

likely a result of the increase in ilmenite modal abundance from 1.20 to 1.66 modal percent, incorporating more of the Fe^{3+} from the bulk.

This shows that above a certain bulk $\text{Fe}^{3+}/\text{Fe}_{\text{tot}}$, the increase in modal proportion of minor phases takes priority over Fe^{3+} in biotite. Although it has been suggested that biotite commonly contains between 6–10% (Ferry and Spear, 1978), and even up to 12% of Fe^{3+} (Dachs and Benisek, 1995), Thermocalc does not put that amount in the modeled bulk compositions (based on activity models), even in case of the highest bulk $\text{Fe}^{3+}/\text{Fe}_{\text{tot}}$ modeled here.

3.5 SUMMARY AND CONCLUSIONS

Phase equilibria modeling (ex. Thermocalc) has become a popular method to investigate the P – T ranges of stabilities of mineral assemblages as well as P – T paths, for specific bulk rock compositions. Among the parameters used for the bulk compositions, Fe^{3+} is problematic because it is rarely measured in rocks, therefore the values assigned to the bulks of natural systems are generally assumed. This study has investigated the way in which activity models and Thermocalc deal with ferric iron in phase equilibria modeling of aluminous systems at the mid- P range of the granulite facies. This was accomplished by calculating phase equilibria diagrams with bulk compositions using: (1) the actual measured $\text{Fe}^{3+}/\text{Fe}_{\text{tot}}$ in biotite ($x(\text{Fe}^{3+})_{\text{bi}}$) in the sample, and (2) a set with a range of bulk $\text{Fe}^{3+}/\text{Fe}_{\text{tot}}$ corresponding to 10, 15 and 20% $x(\text{Fe}^{3+})_{\text{bi}}$. The $x(\text{Fe}^{3+})_{\text{bi}}$ was

measured directly by Mössbauer spectroscopy, and the $x(\text{Fe}^{3+})_{\text{bi}}$ was low compared to estimates for metapelitic biotite in the literature.

Pseudosections calculated with the measured $x(\text{Fe}^{3+})_{\text{bi}}$ are generally consistent with the observed mineral assemblages, textures, and mineral chemistry, an indication that the thermodynamic model for Fe^{3+} is reliable. The effects of changing the Fe^{3+} content of the bulk composition on the mid- P portion of the biotite dehydration field include: (1) the addition, or change in modal proportions or stability of minor phases such as rutile, ilmenite and magnetite, (2) minor shifts in phase boundaries and composition isopleths of ferromagnesian minerals, and (3) changes in the predicted $x(\text{Fe}^{3+})_{\text{bi}}$. However, these changes are small and do not have a profound effect on P - T path determination when you consider the precision of phase equilibria diagrams in the first place.

The mid- P region topologies of aluminous systems investigated in this study are affected much less by changes in the bulk $\text{Fe}^{3+}/\text{Fe}_{\text{tot}}$ than the considerable changes observed at low- P or at ultrahigh- T conditions as documented in the literature. This is likely because of the larger number of Fe^{3+} bearing phases in these conditions compared with mid- P conditions, resulting in more frequent changes in topologies.

REFERENCES

Boger, S. D., White, R. W., Schulte, B., 2012. The importance of iron speciation ($\text{Fe}^{2+}/\text{Fe}^{3+}$) in determining mineral assemblages: an example from the high-grade

- aluminous metapelites of southern Madagascar. *Journal of Metamorphic Geology*, 30, 997-1018.
- Cesare, B., Meli, S., Nodari, L., Russo, U., 2005. Fe³⁺ reduction during biotite melting in graphitic metapelites: another origin of CO₂ in granulites. *Contributions to Mineralogy and Petrology*, 149, 129-140.
- Coggon, R. and Holland, T. J. B., 2002. Mixing properties of phengitic micas and revised garnet-phengite thermobarometers. *Journal of Metamorphic Geology*, 20, 683-696.
- Dachs, E. and Benisek, A., 1995. The stability of annite + quartz: reversed experimental data for the reaction 2 annite + 3 quartz $\frac{1}{4}$ 2 sanidine + 3 fayalite + 2H₂O. *Contributions to Mineralogy and Petrology*, 121, 380-387.
- Diener, J.F.A. and Powell, R., 2010. Influence of ferric iron on the stability of mineral assemblages. *Journal of Metamorphic Geology*, 28, 599-613.
- Dyar, M.D., Lowe, E.W., Guidotti, C.V., Delaney, J.S., 2002. Fe³⁺ and Fe²⁺ partitioning among silicates in metapelites: A synchrotron micro-XANES study. *American Mineralogist* 87, 514-52.
- Ferry, J. M. and Spear, F. S., 1978. Experimental calibration of the partitioning of Fe and Mg between biotite and garnet. *Contributions to Mineralogy and Petrology*, 66, 113-117.
- Hindemith, M. A., 2013. Petrography and geochemistry of hydrothermally altered volcanic rocks metamorphosed at granulite-facies conditions: an example from the central Grenville Province. Masters Thesis. Memorial University of Newfoundland. 131 Pages.
- Holland, T. J. B. and Powell, R., 1998. An internally consistent thermodynamic dataset for phases of petrological interest. *Journal of Metamorphic Geology*, 16, 309-344.
- Holland, T. J. B. and Powell, R., 2003. Activity-composition relations for phases in petrological calculations: an asymmetric multicomponent formulation. *Contributions to Mineralogy and Petrology*, 145, 492-501
- Korhonen, F.J., Powell, R., Stout, J.H., 2012. Stability of sapphirine + quartz in the oxidized rocks of the Wilson Lake terrane, Labrador: calculated equilibria in NCKFMASHTO. *Journal of Metamorphic Geology*, 30, 21-36.
- Letourneau, M. 2011. Anatectic aluminous gneisses from the mesoproterozoic Complexe de la Plus-Value, Grenville Province, Quebec. Memorial University: Honours thesis.

- Patrick, M. E. 2013. Metamorphic Investigation of Anatectic Aluminous Gneisses from the Complexe de la Plus-Value, Grenville Province. Honours Thesis. Memorial University of Newfoundland.
- Powell, R. and Holland, T. J. B., 1988. An internally consistent thermodynamic dataset with uncertainties and correlations: 3. Application, methods, worked examples and a computer program. *Journal of Metamorphic Geology*, 6, 173–204.
- Spear, F.S., Kohn, M.J., Cheney, J.T., 1999. P–T paths from anatectic pelites. *Contributions to Mineralogy and Petrology*, 134, 17–32.
- Tajcmanova, L., Connolly, J. A. D., Cesare, B. 2009. A thermodynamic model for titanium and ferric iron solution in biotite. *Journal of Metamorphic Geology*, 27, 153–165.
- Taylor-Jones, K. and Powell, R., 2010. The stability of sapphirine + quartz: calculated phase equilibria in FeO–MgO–Al₂O₃– SiO₂–TiO₂–O. *Journal of Metamorphic Geology*, 28, 615–633.
- White, R. W., Powell, R., Holland, T. J. B., Worley, B. A., 2000. The effect of TiO₂ and Fe₂O₃ on metapelitic assemblages at greenschist and amphibolite facies conditions: mineral equilibria calculations in the system K₂O–FeO–MgO–Al₂O₃– SiO₂–H₂O–TiO₂–Fe₂O₃. *Journal of Metamorphic Geology*, 18, 497–511.
- White, R. W., Powell, R., Clarke, G. L., 2002. The interpretation of reaction textures in Fe-rich metapelitic granulites of the Musgrave Block, central Australia: constraints from mineral equilibria calculations in the system K₂O–FeO–MgO– Al₂O₃–SiO₂–H₂O–TiO₂–Fe₂O₃. *Journal of Metamorphic Geology*, 20, 621–632.
- White, R.W., Powell, R., Holland, T.J.B., 2007. Progress relating to calculation of partial melting equilibria for metapelites. *Journal of Metamorphic Geology*, 25, 511–527.

Table 3.1. Mineral modes of samples as determined by the SEM-MLA software; normalized after removing secondary minerals and alterations, unknown minerals, sulfides, and minor phases such as monazite and zircon which cannot be accounted for in the NCKFMASHTO system.

Mineral	10-AI-20A	10-AI-114B1	10-AI-58-3B1	331-E2-11
Biotite	12.2	21.55	34.85	19.01
Garnet	7.1	15.22	9.57	3.64
K-feldspar	27.37	7.81	6.52	39.35
Plagioclase	11.39	4.3	3.3	22.15
Sillimanite	5.32	13.15	30.93	0.59
Quartz	36.59	37.76	12.54	14.88
Cordierite	0	0.2	2.25	0
Ilmenite	0	0	0.05	0

Table 3.2. Bulk compositions used in phase equilibrium modeling.

Sample	SiO ₂	Al ₂ O ₃	MgO	FeO	MnO	CaO	Na ₂ O	K ₂ O	TiO ₂	H ₂ O	sum
10-AI-58-3B1	52.57	21.25	8.55	8.53	0.06	0.36	0.44	3.02	1.46	3.77	100
10-AI-20-A	73.75	10.25	3.8	4.56	0.09	0.67	1.49	3.52	0.3	1.58	100
10-AI-114-B	64.64	13.88	5.97	9.08	0.34	0.35	0.49	2.17	0.58	2.49	100
331-e2-11	67.09	10.87	4.69	4.94	0.05	1.11	2.73	5.21	0.89	2.41	100

Table 3.3. Predicted $x(\text{Fe}^{3+})_{\text{bi}}$ (FB) at corners of Field I in pseudosections calculated with measured $x(\text{Fe}^{3+})_{\text{bi}}$ in the sample. Also indicated: P - T coordinates of each point, and T of $x(\text{g})$ and $x(\text{bi})$. Points 1 and 2 correspond to the lower and upper limits of the solidus, and points 3 and 4 are the lower and upper limits of the biotite-out, quartz-out (10-AI-58-3B1), or orthopyroxene-in (331-e2-11) phase boundaries.

Sample	O Value in bulk	Point 1			Point 2			Point 3			Point 4			x(g)	x(bi)
		P	T	FB	T @ 9kbar	T @ 9kbar									
10-AI-20A	0.015	6.41	825.1	1.3	10.2	920.2	1.3	7.42	877.9	5.1	11.4	876.4	4.6	845.6	838.5
	0.031	6.41	825.9	2.7	10.2	821.6	3.3	7.47	879.5	4.5	11.4	878.4	7	846.1	837.9
10-AI-114B1	0.044	6.09	818.1	2.2	10	806.8	2.2	7.08	881.2	7.2	11.6	883.8	7.5	837.5	820.9
	0.059	6.14	814.6	2	10	807.3	2.1	7.23	882.5	2.4	11.6	882.4	5	834.2	819.3
10-AI-58-3B1	0.07	6.51	837.2	2.8	10.4	827.5	2.8	7.36	892.6	6.4	12.2	910.5	8.6	853.7	N/A
	0.094	6.5	837.9	3.7	10.4	828.4	3.8	7.34	893.8	8.3	12.2	912.5	11	854.6	N/A
331-e2-11	0.031	5.64	827.8	1.8	10.2	819.2	1.8	5.23	839.8	2	11.87	913.3	2	829	N/A
	0.047	5.68	828.2	2.7	10.2	819.6	2.8	5.24	840.9	3.1	11.73	913.3	3.1	828.9	N/A

Table 3.4. Predicted $x(\text{Fe}^{3+})_{\text{bi}}$ (FB) at corners of Field I in pseudosections calculated with O=0.05, 10% (A), 15% (B) and 20% (C) $x(\text{Fe}^{3+})_{\text{bi}}$. Also indicated: P - T coordinates and T of $x(\text{g})$ and $x(\text{bi})$. See previous table for description of points.

10-AI-20A	Point 1			Point 2			Point 3			Point 4 (bi,pl)			$x(\text{g})$	$x(\text{bi})$
	P	T	FB	P	T	FB	P	T	FB	P	T	FB	T @ 9kbar	T @ 9kbar
Original	6.43	825	3.6	10.1	821.1	3.7	7.51	881.5	4.8	11.7	878.5	7.2	844.5	835.8
A (O = 0.079)	6.44	827.2	3.7	10.2	823.9	4.5	7.46	881.7	7.6	11.6	881.4	*10.1	848.1	842.2
B (O = 0.119)	6.48	827.6	3.9	10.3	824.1	4.8	7.5	883.6	7.9	11.67	883.4	*10.4	848	839.3
C (O = 0.158)	6.52	828.2	4	10.4	824.7	5	7.54	885.4	8.1	11.74	885.4	*10.7	848	836.9
10-AI-114B	Point 1			Point 2			Point 3			Point 4			$x(\text{g})$	$x(\text{bi})$
Fe ³⁺ in bulk	P	T	FB	P	T	FB	P	T	FB	P	T	FB	T @ 9kbar	T @ 9kbar
original	6.08	818.3	2.5	10	807.1	2.5	7.07	881.9	8	11.5	884.8	8.3	838.4	821
A (O = 0.15)	6.18	814.8	3.2	10	806.3	3.2	7.27	882	4.3	11.8	885.2	5.3	831.2	815.8
B (O = 0.224)	6.21	813.7	3.5	9.8	806.9	3.6	7.29	882.2	5	11.6	888.3	5.4	829.3	814.1
C (O = 0.30)	6.24	813.2	3.9	9.8	806.2	3.9	7.32	884.3	5	11.6	890.8	5.6	826.2	811.4
10-AI-58-3B1	Point 1			Point 2 (liq,ru)			Point 3			Point 4			$x(\text{g})$	$x(\text{bi})$
Fe ³⁺ in bulk	P	T	FB	P	T	FB	P	T	FB	P	T	FB	T @ 9kbar	T @ 9kbar
original	6.51	836.5	2	10.4	826.7	2	6.07	1060.4	9.2	14.4	1022.4	7.5	853.1	N/A
A (O = 0.23)	6.68	839.7	3.3	10.45	835.1	*3.4	6.67	1050.4	5.2	14.4	1005.8	7.8	849.4	N/A
B (O = 0.351)	6.73	840.7	4	10.6	835.6	4	6.74	1049	6.6	14.2	1002.2	8.4	847.7	N/A
C (O = 0.468)	6.77	841.8	4.3	10.6	837.1	4.4	6.81	1048	7.6	14.2	996.4	9	846.5	N/A
331-e2-11	Point 1			Point 2			Point 3 (cd,opx)			Point 4 (ru,opx)			$x(\text{g})$	$x(\text{bi})$
Fe ³⁺ in bulk	P	T	FB	P	T	FB	P	T	FB	P	T	FB	T @ 9kbar	T @ 9kbar
original	5.69	828.2	2.9	10.2	819.7	2.9	5.24	841.1	3.3	11.71	913.3	3.3	828.9	N/A
A (O = 0.15)	6.44	824.8	3	10.4	918.8	3.1	5.92	850.4	3.6	11.28	918.6	4.1	N/A	N/A
B (O = 0.232)	6.48	825.7	3.6	10.4	820.8	3.6	6.08	853.8	4.4	11.76	925.7	5.7	N/A	N/A
C (O = 0.31)	6.52	826.9	3.8	10.4	822.2	3.8	6.25	857.6	4.9	12.01	930.3	6.6	N/A	N/A

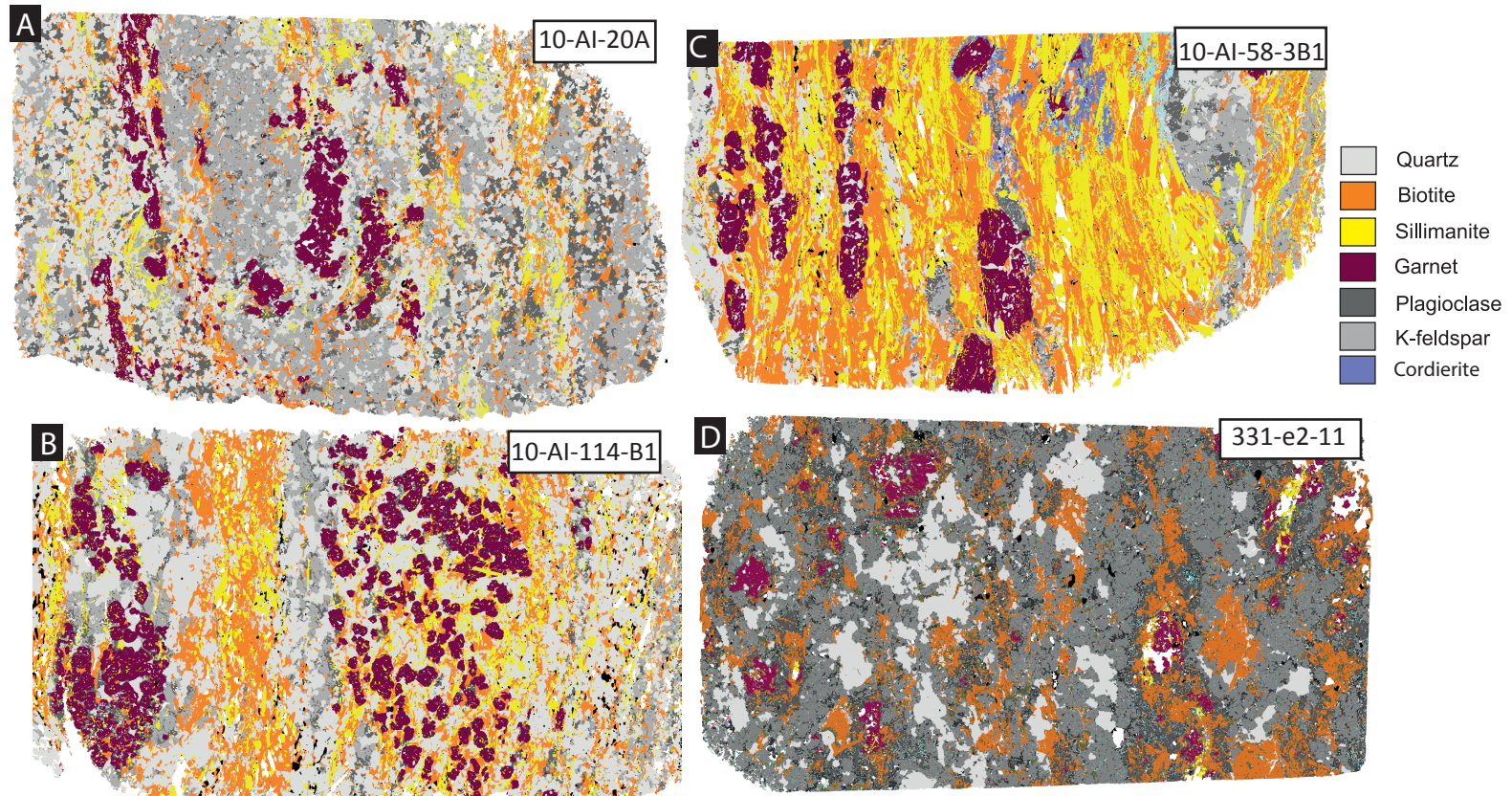


Figure 3.1: False colour MLA-SEM mineral maps showing distribution of minerals at the thin section scale (using standard 46mm slide) for samples (a) 10-AI-20A, (b) 10-AI-114-B!, (c) 10-AI-58-3B1 and (d) 331-E2-11.

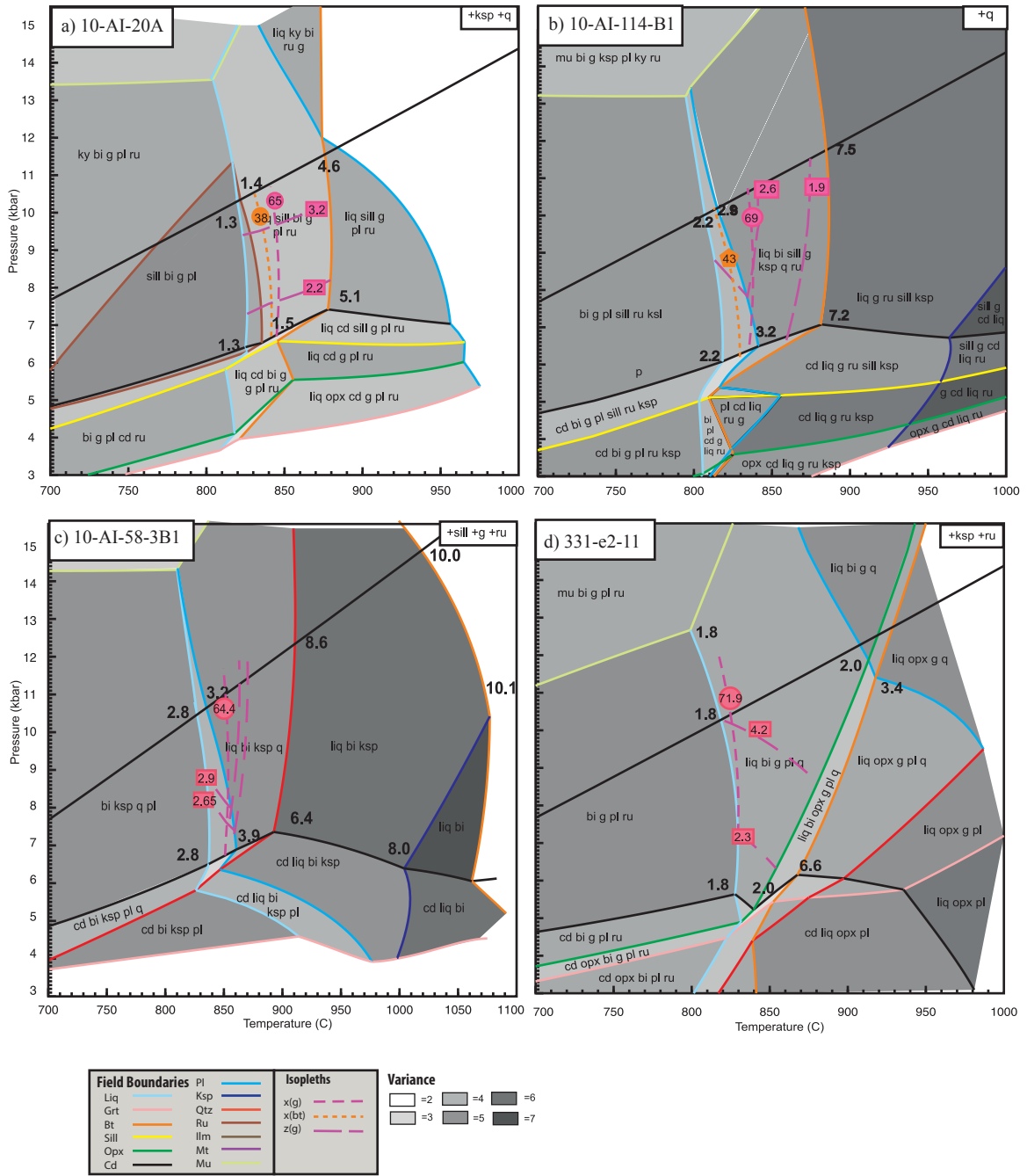


Figure 3.2. Pseudosections calculated with the average of the measured $x(\text{Fe}^{3+})_{\text{bi}}$ in the bulk for (a) 10-AI-20A, (b) 10-AI-114-B1, (c) 10-AI-58-3B1 and (d) 331-e2-11. These pseudosections also show isopleths of $x(\text{bi})$, $x(\text{g})$ and the range of $z(\text{g})$ corresponding to garnet and biotite compositions in the samples, and predicted $x(\text{Fe}^{3+})_{\text{bi}}$ at the corners of the fields of interest. Phases in the top-right box are stable throughout.

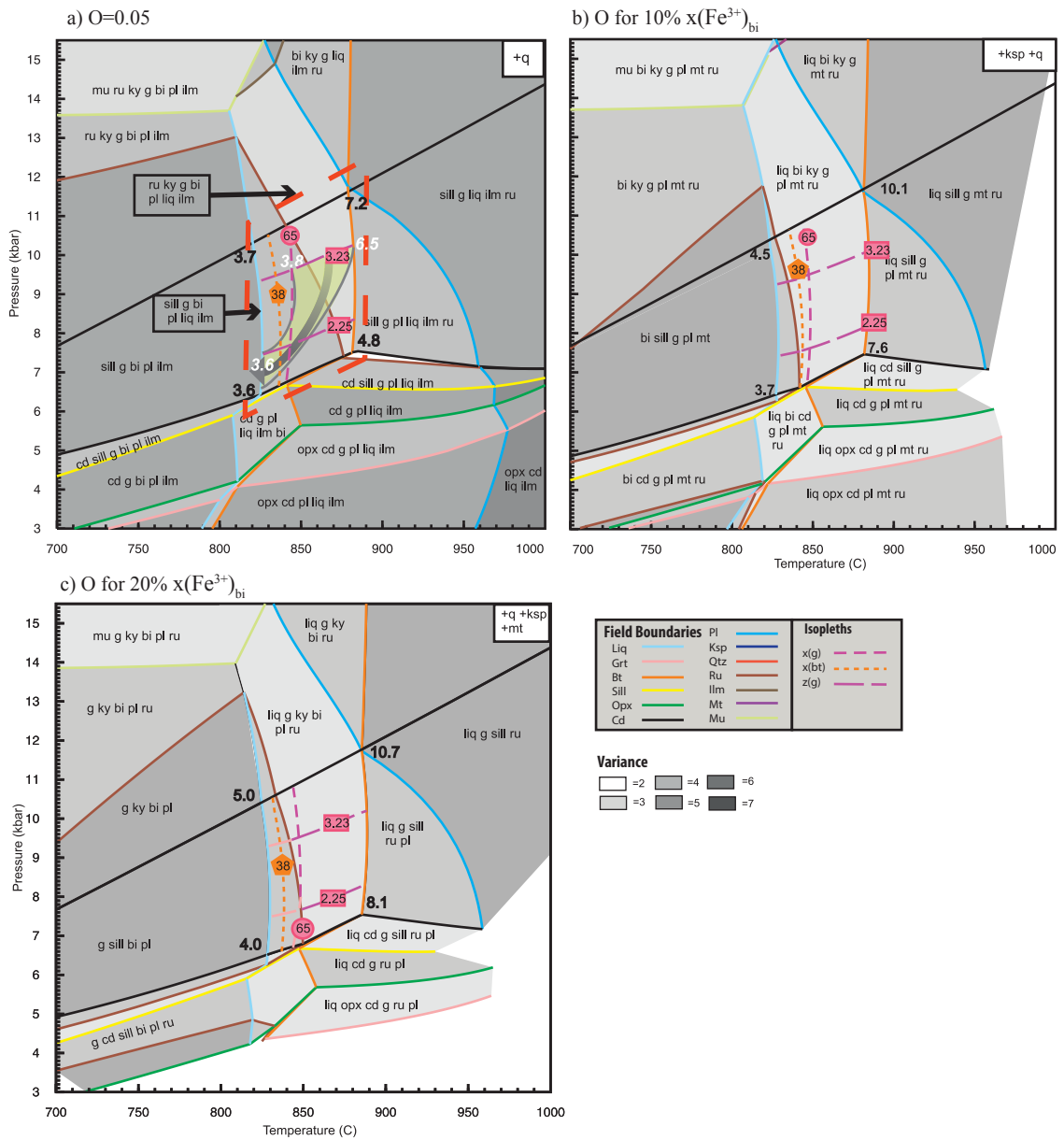


Figure 3.3. Pseudosections for sample 10-AI-20A calculated with: (a) $O=0.05$; (b) O corresponding to $10\% x(\text{Fe}^{3+})_{\text{bi}}$; and (c) O corresponding to $20\% x(\text{Fe}^{3+})_{\text{bi}}$. These pseudosections also show isopleths of $x(\text{bi})$, $x(\text{g})$ and the range of $z(\text{g})$ corresponding to garnet and biotite compositions in the samples and predicted $x(\text{Fe}^{3+})_{\text{bi}}$ at the corners of the fields of interest in bold and in white at points of interest on the P - T path. Phases in the top-right box are stable throughout. Field I is indicated by a thick red dashed line in (a).

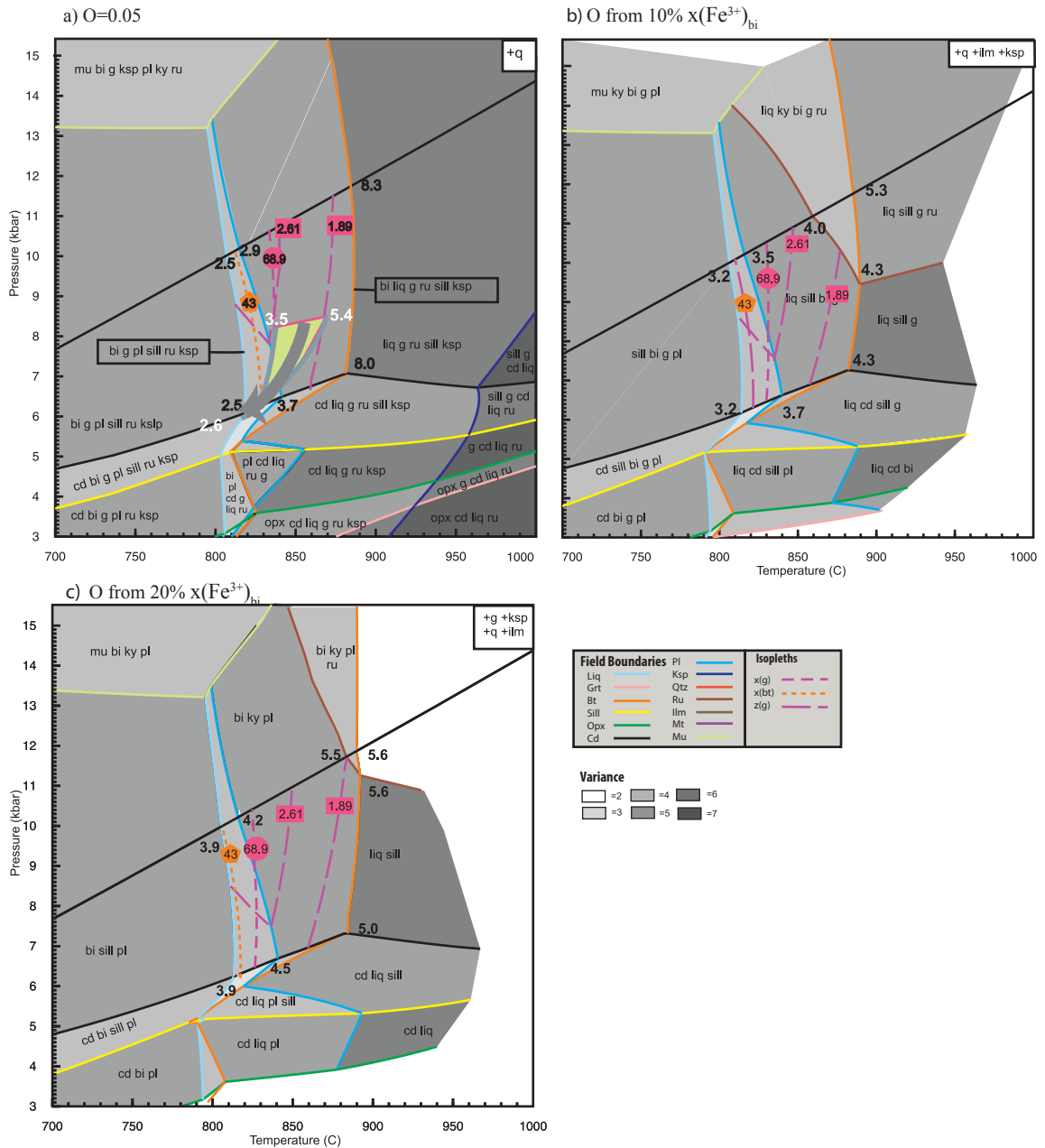


Figure 3.4. Pseudosections for sample 10-AI-114-B1 calculated with: (a) $O=0.05$; (b) O corresponding to $10\% x(\text{Fe}^{3+})_{\text{bi}}$; and (c) O corresponding to $20\% x(\text{Fe}^{3+})_{\text{bi}}$. These pseudosections also show isopleths of $x(\text{bi})$, $x(\text{g})$ and the range of $z(\text{g})$ corresponding to garnet and biotite compositions in the samples, and predicted $x(\text{Fe}^{3+})_{\text{bi}}$ at the corners of the fields of interest in bold and in white at points of interest on the P - T path. Phases in the top-right box are stable throughout.

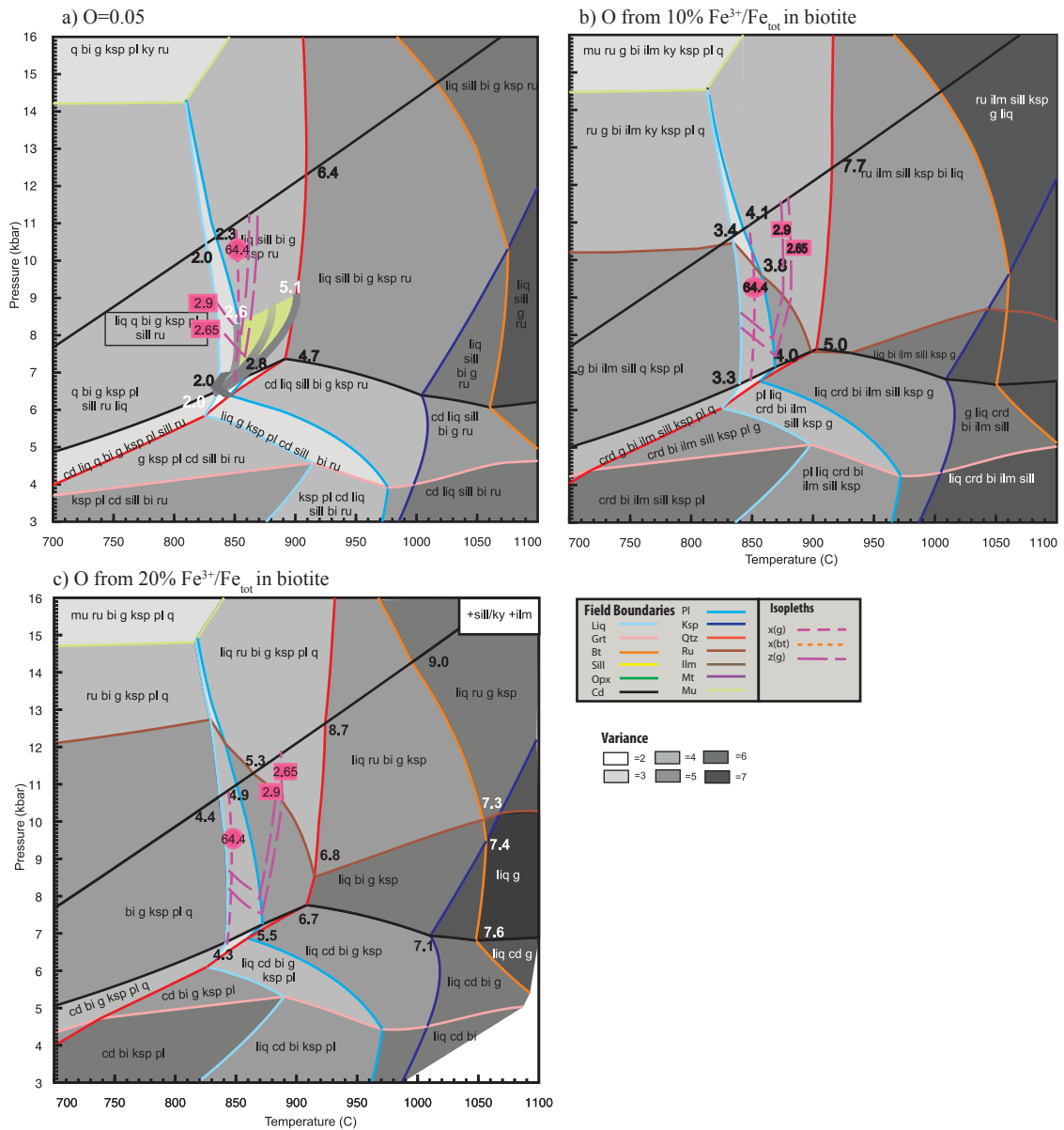


Figure 3.5. Pseudosections for sample 10-AI-58-3B1 calculated with: (a) $O=0.05$; (b) O corresponding to 10% $x(Fe^{3+})_{tot}$; and (c) O corresponding to 20% $x(Fe^{3+})_{tot}$. These pseudosections also show measured isopleths of $x(g)$ and the range of $z(g)$ corresponding to garnet and biotite compositions in the samples, and predicted $x(Fe^{3+})_{tot}$ at the corners of the fields of interest in bold and in white at points of interest on the $P-T$ path. Phases in the top-right box are stable throughout.

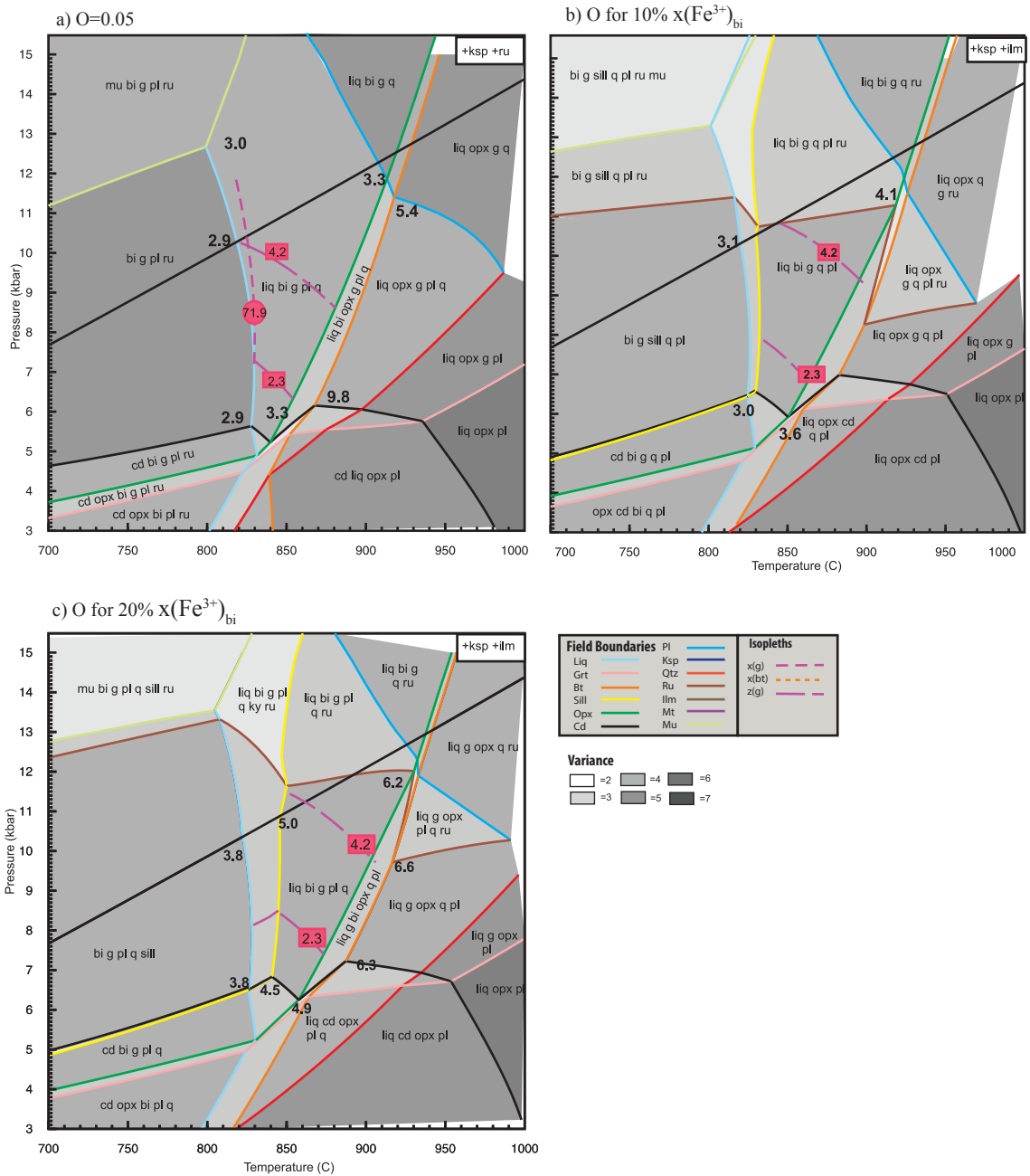


Figure 3.6. Pseudosections for sample 331-e2-11 calculated with: (a) $O=0.05$; (b) O corresponding to $10\% x(\text{Fe}^{3+})_{\text{bi}}$; and (c) O corresponding to $20\% x(\text{Fe}^{3+})_{\text{bi}}$. These pseudosections also show measured isopleths of $x(\text{g})$ and the range of $z(\text{g})$ corresponding to garnet and biotite compositions in the samples, and predicted $x(\text{Fe}^{3+})_{\text{bi}}$ at the corners of the fields of interest in bold. Phases in the top-right box are stable throughout.

CHAPTER 4: COMPARISON OF REINTEGRATION OF MELT AND WATER METHODS IN ANATECTIC ALUMINOUS SYSTEMS

4.1 INTRODUCTION

Following water-saturated melting, which is generally limited, partial melting in aluminous rocks, such as metapelites, under upper- amphibolite and granulite-facies metamorphic conditions proceeds by the dissolution of OH⁻ available in micas (dehydration melting reactions; Spear *et al.*, 1999). Once significant amounts of melt have formed (~ 7%; Rosenberg and Handy, 2005), these rocks commonly experience melt loss. This happens mainly in dynamic environments such as orogenic belts, because the melt is squeezed out under stress (Brown, 2007). The melts produced are felsic and peraluminous in nature, and once solidified, they may form biotite, muscovite, cordierite, garnet, and/or an aluminosilicate (Patiño-Douce and Johnston, 1991).

The melt history and P - T evolution of aluminous rocks is best investigated using phase equilibria modeling. Phase equilibria diagrams calculated with the bulk compositions of melt-depleted rocks show: (a) a solidus at higher- T relative to those calculated with the original bulk composition before melt loss, and (b) reduced (or absent) stability fields for muscovite, a key mineral before the onset of melting, in the subsolidus fields.

White and Powell (2002) developed a method to take into account melt loss in aluminous systems. It involves the reintegration of hypothetical amounts of melt in melt depleted bulk rock compositions, using phase equilibria modeling in Thermocalc. Although it is impossible to determine the exact amount of the lost melt and the number of melt loss episodes, they have shown that suprasolidus topologies of phase equilibria diagrams calculated from melt reintegrated bulk compositions (melt-added pseudosections) do not change significantly with different melt loss histories. As a result, this method allows the calculation of suprasolidus topologies in melt-reintegrated (melt-added) P - T pseudosections, which can be used to constrain the prograde portions of P - T paths, because information on these is recorded in the rocks before they experienced melt loss (Indares *et al.*, 2008; Guilmette *et al.*, 2011; Groppo *et al.*, 2012).

Alternatively, it has been suggested that since in anatectic aluminous systems water is incorporated in the melt fraction, and the melt composition is largely composed minerals in excess (quartz and feldspars), simply adding water to the bulk composition of the rock should allow the calculation of topologies before the melt loss (water-added method). However, since certain elements are preferentially incorporated into the melt over others, adding only water in the bulk composition may be an oversimplification. There are currently no studies that address this issue. This investigation aims to document the differences between the mid- to high- P topologies of P - T pseudosections calculated with the melt-reintegration method of White and Powell (2002) and the added water method by calculating pseudosections using both methods.

Five samples (10-AI-20A, 10-AI-114-B1, HJ-57B, HJ-58C and 10-AI-76) from the central Grenville Province were selected for this study. These were chosen based on their wide range of mineral proportions and bulk compositions; samples 10-AI-20A, 10-AI-114-B1, HJ-57B and HJ-58C are sillimanite-rich (with sillimanite being part of the peak assemblage) and 10-AI-76 is sillimanite-poor (sillimanite is restricted to aluminous nodules). In addition, these have a wide range of biotite proportions, with 10-AI-114-B1 being the richest in biotite with 21.55 modal %, and 10-AI-76 is the poorest with 5.20 modal %. All have experienced mid-*P* granulite facies metamorphism and show evidence of former melt production and loss. The evidence for this, along with the petrography of the samples is discussed in Chapter 2.

4.2 PHASE EQUILIBRIA MODELING

The *P*–*T* pseudosections in this study were calculated with THERMOCALC 3.33 (Powell and Holland, 1988) in the Na₂O–CaO–K₂O–FeO–MgO–Al₂O₃–SiO₂–H₂O–TiO₂–O (NCKFMASHTO) system. The calculations used the internally consistent dataset tcds55, created November 22, 2003, and the minerals Liq–Q–G–Ksp–Pl–Sill–Bi–Cd–Mu–Ru–Ilm–Opx (abbreviation list is available on page xii) were considered in the calculations. The following a–x models were used: garnet (g: White et al., 2007), biotite (bi: White et al., 2007), cordierite (cd: Holland and Powell, 1998), muscovite (mu: Coggon and Holland, 2002), plagioclase and K-feldspar (pl, ksp: Holland and Powell, 2003), orthopyroxene (opx: White et al., 2002), ilmenite (ilm: White et al., 2000) and melt (liq: White et al., 2007).

To calculate melt-added pseudosections (White and Powell, 2002), a P - T pseudosection using the actual bulk composition (melt-depleted bulk) of the rock must first be calculated (these are discussed in Chapter 2; Figures 2.7a,c and 2.9a-c). In this diagram, the composition of the first infinitesimal amount of melt is determined where the prograde portion of the P - T path is projected to have crossed the solidus (the dry solidus in melt-depleted diagrams). Proportions of melt with this composition are then added to the bulk composition until the topologies can be calculated down from the dry solidus to a water saturated solidus (the wet solidus) on the melt-added diagram. Here it is assumed that the rock was actually water saturated at the onset of melting, and that melt was lost in one episode. Using the second method, the amount of water required to saturate the solidus is added to the bulk rock composition.

The bulk compositions that were used to calculate each are listed in Table 4.1. The melt composition that was added obtain the melt-added bulk composition is listed in Table 4.2; this composition was extrapolated at the point where the P - T path intersects the solidus in the melt-depleted diagrams. Also listed in Table 4.2 are the melt compositions taken at the same P - T coordinates in the melt-added and water-added pseudosections.

4.2.1 Comparison of pseudosections with melt and water

The two sets of P - T pseudosections are calculated in the range of 700–1000°C or 650–950°C and 3–15.5 kbar, and are shown in Figures 4.1–4.5. For samples HJ-57B and 10-AI-76 the two sets are almost identical, other than a minor shift down- T of the

plagioclase stability in the former (Figures 4.4 and 4.5). In the case of the other three samples however, there are major differences between the two sets. For these three samples, the isomodes of liquid (melt), muscovite and K-feldspar were calculated and added in the pseudosections.

4.2.1.1 Sample 10-AI-20A

The main differences between the two pseudosections for sample 10-AI-20A are within the muscovite-bearing topologies at the low- T side of the diagram. In the melt-added diagram (Figure 4.1a), the aluminosilicate- and muscovite-out phase boundaries approximately coincide with one another, whereas in the water-added diagram (Figure 4.1b), the aluminosilicate stability is increased to higher P at low T . This shifts the stability field of sillimanite to higher pressures, and most importantly, decreases the size of the field of melting, in the water-only diagram. The high- T , supra-solidus side of P - T pseudosection is very similar in both diagrams. The only significant difference is that the stability field of plagioclase is slightly displaced to higher T in the melt-added pseudosection. Melt production begins at lower- T in the melt-added diagram; however, the amount of melt produced in both diagrams is the same at the biotite-out phase boundary (~40%).

4.2.1.2 Sample 10-AI-114-B1

For sample 10-AI-114-B1, sillimanite, biotite, cordierite, quartz and orthopyroxene have approximately the same field boundaries in both pseudosections (Figure 4.2). In the water-added diagram (Figure 4.2b), the stability fields of plagioclase

and K-feldspar are reduced significantly to lower- T and lower- P , respectively. The melt-added pseudosection (Figure 4.2a) sees the introduction of garnet at $\sim 700^{\circ}\text{C}$ for the mid- P region, which is common in metapelitic pseudosections (that are not modeled in a system with Mn), whereas garnet is stable to low- P and T in the water-added diagram. In general, it appears as though the fields on the low- P side of the mid- P section have been expanded down- T in this rendition of phase relations.

The assemblages of the melt-added diagram are significantly more melt fertile than the water-added one. Melt production reaches $\sim 50\%$ by the biotite-out phase boundary in the former, but only $\sim 40\%$ in the latter diagram.

4.2.1.3 Sample HJ-58c

For sample HJ-58C, the two pseudosections are very different (Figure 4.3). The only phase boundaries that are similar are those of biotite and rutile; orthopyroxene phase boundaries are also similar but are extended to lower temperatures in the water-added pseudosection. In the water-added diagram, K-feldspar's stability is reduced to higher pressures, and sillimanite and muscovite phase boundaries are moved to higher pressures. Similar to 10-AI-114-B1, the melt-added pseudosection sees the introduction of garnet at $\sim 720^{\circ}\text{C}$ for the mid- P region, yet garnet is stable to low- P and T in the water-only diagram. The distribution of isomodes show there is slightly greater melt production in the melt-added diagram (ex. 42% compared with 38% at the biotite boundary), as well as more peritectic K-feldspar at any point.

4.2.1.4 Sample HJ-57b

For sample HJ-57b, both methods produce topologies that are very similar (Figure 4.4a-b), except that the plagioclase stability field has been reduced to lower- T , and sillimanite is reduced to higher- P in the water-only diagram, to a small degree. Also, the distribution of isomodes show that there is more K-feldspar in the melt-added diagram at any point. Finally, melt production is slightly higher in the melt-added diagram, being 44% compared with 40% at the biotite-out boundary.

4.2.1.5 Sample 10-AI-76

Both pseudosections for sample 10-AI-76, the only sillimanite-poor sample, appear to be virtually identical on visual inspection (Figure 4.5). However, on comparison of the P - T coordinates of each point, there are small differences for every phase boundary and point, but these are minor.

4.2.2 Comparison of melt composition

The composition of melt produced in the melt-added and water-added diagrams was compared at the same P - T coordinates: where the melt composition was determined on the original pseudosection at the “dry solidus”. These compositions and coordinates are available in Table 4.2. The P - T coordinates range from 8.5–10 kbar and 812–863°C in each, allowing for development of melt over >150 °C from the “wet solidus” up to this point. Yet the compositions of melt are quite similar to each other and to the original melt composition taken from the original diagram. The melt compositions are most similar in terms of Al_2O_3 , MgO and FeO , while their CaO , Na_2O and K_2O contents are slightly different.

Although only H₂O was added to the water-added diagrams, this does not necessarily produce a melt with more H₂O content.

4.3 DISCUSSION AND CONCLUSIONS

This study compared the topologies of phase equilibria diagrams calculated with two different methods of accommodating for melt loss in aluminous systems. This was done by adding to the bulk compositions of the modeled rocks: (1) an amount of melt, enough to saturate the solidus in H₂O, or (2) only the water required to saturate the solidus. The pseudosections calculated for three of the five pseudosections are significantly different between the two methods.

For samples 10-AI-114-B1 and HJ-58c, the melt-added pseudosections appear to be more complex, having more phase boundaries, and therefore more frequent changes in topologies, than those of water-added diagrams. In these, and also 10-AI-20A, the K-feldspar and plagioclase stability fields tend to be reduced, and the garnet stability field increased, in the water-added diagrams.

The phase boundaries that are affected most by the two methods are generally those involved in muscovite and biotite dehydration melting reactions ($Ms + Q \pm Pl \rightarrow Ksp + Sill + melt$ and $Bi + Sill + Q \pm Pl \rightarrow G + melt + Ksp$), with the exception of quartz, likely because it is in excess in all cases. This makes sense as melt is produced by these reactions and the water-added method does not provide the essential oxides in melt. The

phase boundaries of the minor phases rutile and ilmenite are not affected by the different methods, likely because reintegrated melt does not incorporate any TiO_2 or Fe_2O_3 into the new bulk composition. Additionally, orthopyroxene and cordierite phase boundaries only show negligible shifts.

The amount of melt required to saturate the solidus in H_2O was between 20 and 26% in all cases except for the sillimanite-poor sample 10-AI-76, where it was only 10%. The composition of the added melt was similar for all samples (Table 4.2), within the range of SiO_2 (~61–65%), H_2O (~17–20%) and Al_2O_3 (~7–8%). Na_2O and K_2O make up a few percent of each (2–4% and 3–4%, respectively), CaO around 1%, FeO and MgO at <1%, and TiO_2 is negligible. Such a melt composition would produce a rock mainly consisting of quartzofeldspathic minerals with a small proportion of aluminosilicates and ferromagnesian minerals, which is consistent with S-type granitoids (Patiño-Douce and Johnston, 1991). It makes much more sense to add back melt with a composition that is consistent with what we observe in nature than to simply add water, when we know that the rock has lost more than that.

Nonetheless, the melt-added simplification does have some merit, as the P – T pseudosections calculated for two samples are almost identical using the different methods. However, there are still three samples for which the calculated P – T pseudosections are significantly different, so it is likely that the water method can only be applicable in certain situations. This is not to say that the melt-reintegration method used is perfect; there are assumptions and generalizations made in that process as well (such as

assuming that the composition of melt does not change as melting progresses) that are likely to affect the pseudosection produced. However, these assumptions are not as extreme as those that come with simply adding water. For example, although water is needed to produce melt, other oxides are also needed as previously mentioned, and these must then be taken from the solid phases in the pseudosection. If the purpose is to determine the topologies to create a P - T path, then we do not want solid phases to be affected.

A significant question now remaining is this: what was different in HJ-57b and 10-AI-76 that resulted in both methods producing similar phase diagrams? Factors that may have had an influence include both these samples having: (1) the most quartzofeldspathic minerals (Table 2.1: 81.0 and 89.6 modal %) and lowest combined G+Bi+Sill+Cd, (2) the lowest quantities of water in the melt-reintegrated bulks (Table 4.1: 4.9 and 2.6%), and (3) the lowest MgO and FeO in the original, melt-reintegrated and water-added bulk compositions (Tables 2.5 and 4.1).

To conclude, although simply adding water in some instances was successful, it was not in all cases. Adding melt to the bulk composition is therefore a much more effective method to use, and is also fairly simple to learn.

REFERENCES

- Brown, M. 2007. Crustal melting and melt extraction, ascent and emplacement in orogens: mechanism and consequences. *Journal of Geological Society of London*, 164, 709–730.
- Coggon, R. and Holland, T. J. B., 2002. Mixing properties of phengitic micas and revised garnet-phengite thermobarometers. *Journal of Metamorphic Geology*, 20, 683–696.
- Groppo, C., Rolfo, F., Indares, A. 2012. Partial melting in the Higher Himalayan Crystallines of eastern Nepal; the effect of decompression and implications for the 'channel flow' model. *Journal of Petrology*, 53, 1057-1088.
- Guilmette, C., Indares, A., Hébert, R. 2011. High-pressure anatectic paragneisses from the Namche Barwa, Eastern Himalayan Syntaxis: Textural evidence for partial melting, phase equilibria modeling and tectonic implications. *Lithos*. 124, 66-81.
- Holland, T. J. B. and Powell, R., 1998. An internally-consistent thermodynamic data set for phases of petrological interest. *Journal of Metamorphic Geology*, 16, 309–343.
- Holland, T. J. B. and Powell, R., 2003. Activity-composition relations for phases in petrological calculations: an asymmetric multicomponent formulation. *Contributions to Mineralogy and Petrology*, 145, 492–501.
- Indares, A.D., White, R.W., Powell, R., 2008. Phase equilibria modelling of kyanite bearing anatectic paragneisses from the central Grenville Province. *Journal of Metamorphic Geology*, 26, 815–836.
- Patiño-Douce, A.E. and Johnston, A.D., 1991. Phase equilibria and melt productivity in the pelitic system; implications for the origin of peraluminous granitoids and aluminous granulites. *Contributions to Mineralogy and Petrology*, 107, 202-218.
- Powell, R., Holland, T.J.B. 1988 An internally consistent thermodynamic dataset with uncertainties and correlations: 3. Applications to geobarometry, worked examples and a computer program. *Journal of Metamorphic Geology*, 6, 173-204.
- Rosenberg, C.L., Handy, M.R., 2005. Experimental deformation of partially melted granite revisited; implications for the continental crust. *Journal of Metamorphic Geology*, 23, 19–28.
- Spear, F.S., Kohn, M.J., Cheney, J.T., 1999. P–T paths from anatectic pelites. *Contributions to Mineralogy and Petrology*, 134, 17–32.

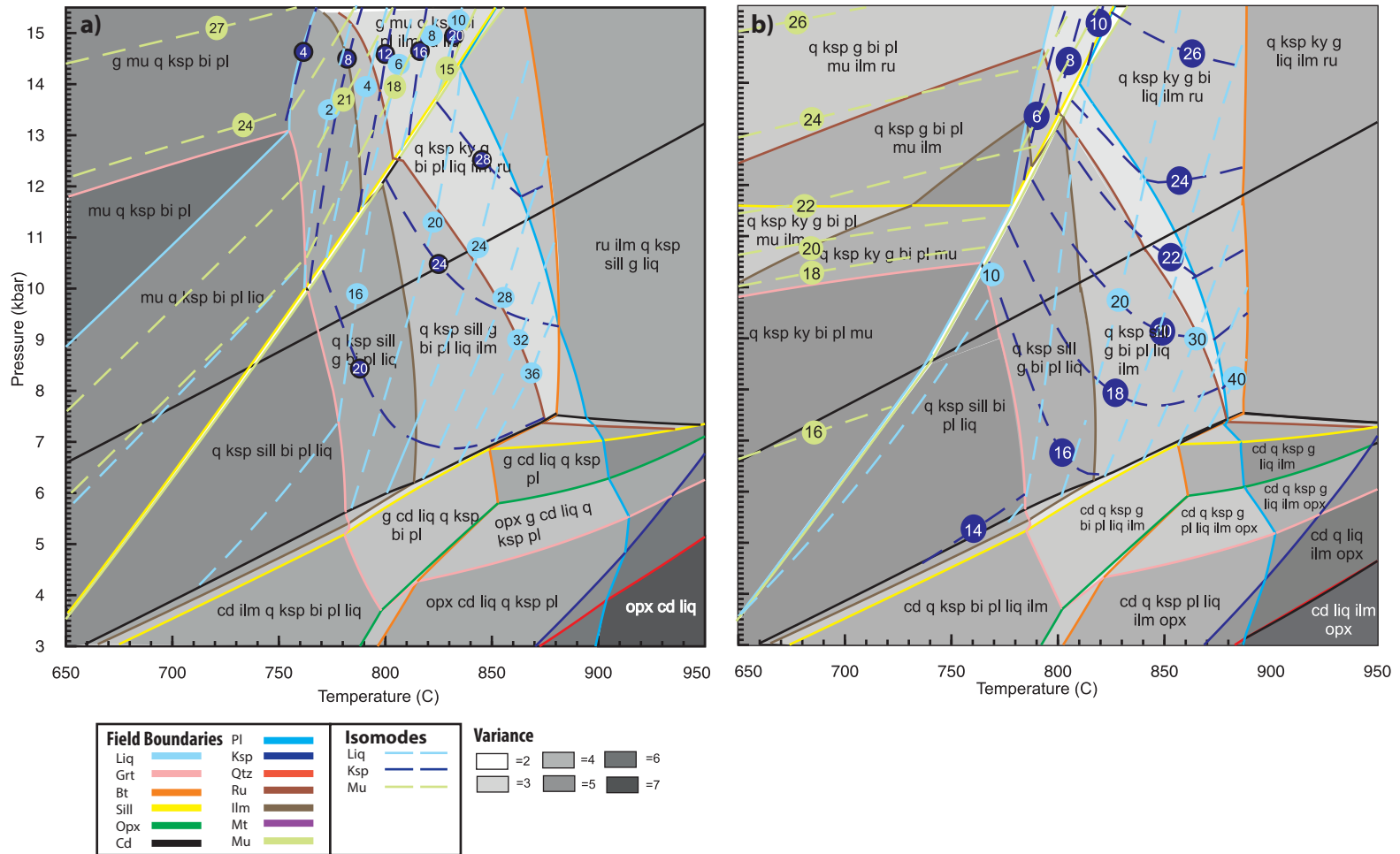
- White, R.W. and Powell, R. 2002. Melt loss and the preservation of granulite facies assemblages. *J. Metamorphic Geology*, 20, 621-632.
- White, R.W., Powell, R., Holland, T.J.B., 2007. Progress relating to calculation of partial melting equilibria for metapelites. *Journal of Metamorphic Geology*, 25, 511-527.
- White, R. W., Powell, R., Holland, T. J. B., Worley, B. A., 2000. The effect of TiO₂ and Fe₂O₃ on metapelitic assemblages at greenschist and amphibolite facies conditions: mineral equilibria calculations in the system K₂O-FeO-MgO-Al₂O₃-SiO₂-H₂O-TiO₂-Fe₂O₃. *Journal of Metamorphic Geology*, 18, 497-511.

Table 4.1. Bulk compositions used in the original, melt-added and water-added pseudosections, in % mol oxide.

	Oxides (mol %)									
	SiO ₂	Al ₂ O ₃	MgO	FeO	CaO	Na ₂ O	K ₂ O	TiO ₂	H ₂ O	O
10-AI-20-A										
Original	73.75	10.25	3.8	4.56	0.67	1.49	3.52	0.3	1.58	0.05
Melt-added	71.84	9.82	3.08	3.76	0.66	1.85	3.45	0.24	5.25	0.04
water-added	71.13	9.89	3.67	4.40	0.65	1.44	3.40	0.29	5.06	0.04
10-AI-114-B										
Original	64.64	13.88	5.97	9.08	0.35	0.49	2.17	0.58	2.49	0.15
Melt-added	64.57	12.38	4.48	6.89	0.39	1.27	2.39	0.43	7.09	0.11
water-added	61.80	13.27	5.71	8.68	0.33	0.47	2.07	0.55	6.78	0.05
HJ-58C										
Original	72.17	9.93	4.25	6.49	1.62	2.81	1.59	0.29	0.76	0.05
Melt-added	72.17	9.92	4.24	6.49	1.62	2.81	1.59	0.29	5.78	0.05
water-added	68.72	9.45	4.04	6.18	1.54	2.68	1.52	0.28	5.50	0.05
HJ-57b										
Original	78.10	8.73	2.91	3.27	0.15	0.81	4.26	0.48	1.16	0.05
Melt-added	75.19	8.10	2.67	2.63	0.84	0.90	4.38	0.37	4.88	0.04
water-added	75.19	7.67	3.28	3.15	0.63	0.67	4.19	0.46	4.66	0.05
10-AI-76										
Original	74.94	9.99	1.89	3.20	1.28	2.57	5.03	0.36	0.61	0.05
Melt-added	73.91	9.77	1.73	2.96	1.22	2.63	4.85	0.32	2.58	0.05
water-added	73.46	9.79	1.86	3.13	1.25	2.51	4.93	0.35	2.53	0.05

Table 4.2. Compositions of melt: (A) calculated at the point where the P - T path is extrapolated to have crossed the dry solidus in the original pseudosections, and determined at the same P - T coordinates as A in the melt-added (B) and water-added (C) diagrams.

	Oxides (mol %)								
	SiO ₂	Al ₂ O ₃	MgO	FeO	CaO	Na ₂ O	K ₂ O	TiO ₂	H ₂ O
10-AI-20A (9kbar - 835 C)									
A)	64.12	8.08	0.20	0.58	0.65	3.29	3.18	0.00	19.91
B)	64.63	8.21	0.23	0.61	0.69	3.22	3.44	0.00	18.98
C)	64.86	8.22	0.22	0.59	0.80	2.90	3.47	0.00	18.94
10-AI-114-B1 (8.5 kbar - 812 C)									
A)	64.01	7.99	0.18	0.57	0.51	3.50	3.01	0.00	20.21
B)	64.00	8.00	0.18	0.57	0.51	3.51	3.01	0.00	20.23
C)	62.86	7.50	0.20	0.60	0.65	2.44	3.34	0.00	22.42
HJ-58c (9.5 kbar - 836 C)									
A)	63.67	8.17	0.23	0.59	0.58	3.80	2.86	0.00	20.10
B)	63.93	8.20	0.23	0.61	0.56	3.78	2.88	0.00	19.81
C)	63.97	8.19	0.23	0.60	0.60	3.64	2.97	0.00	19.79
HJ-57b (10 kbar - 863 C)									
A)	65.74	8.60	0.23	0.53	1.46	1.59	4.48	0.00	17.36
B)	65.71	8.59	0.23	0.53	1.46	1.60	4.48	0.00	17.41
C)	65.78	8.61	0.22	0.52	1.57	1.42	4.61	0.00	17.27
10-AI-76 (9.5 kbar - 834 C)									
A)	64.74	7.84	0.31	0.95	0.74	3.12	3.34	0.00	18.96
B)	63.89	7.84	0.28	0.84	0.77	3.17	3.29	0.00	19.93
C)	63.91	7.81	0.29	0.87	0.79	3.08	3.34	0.00	19.91



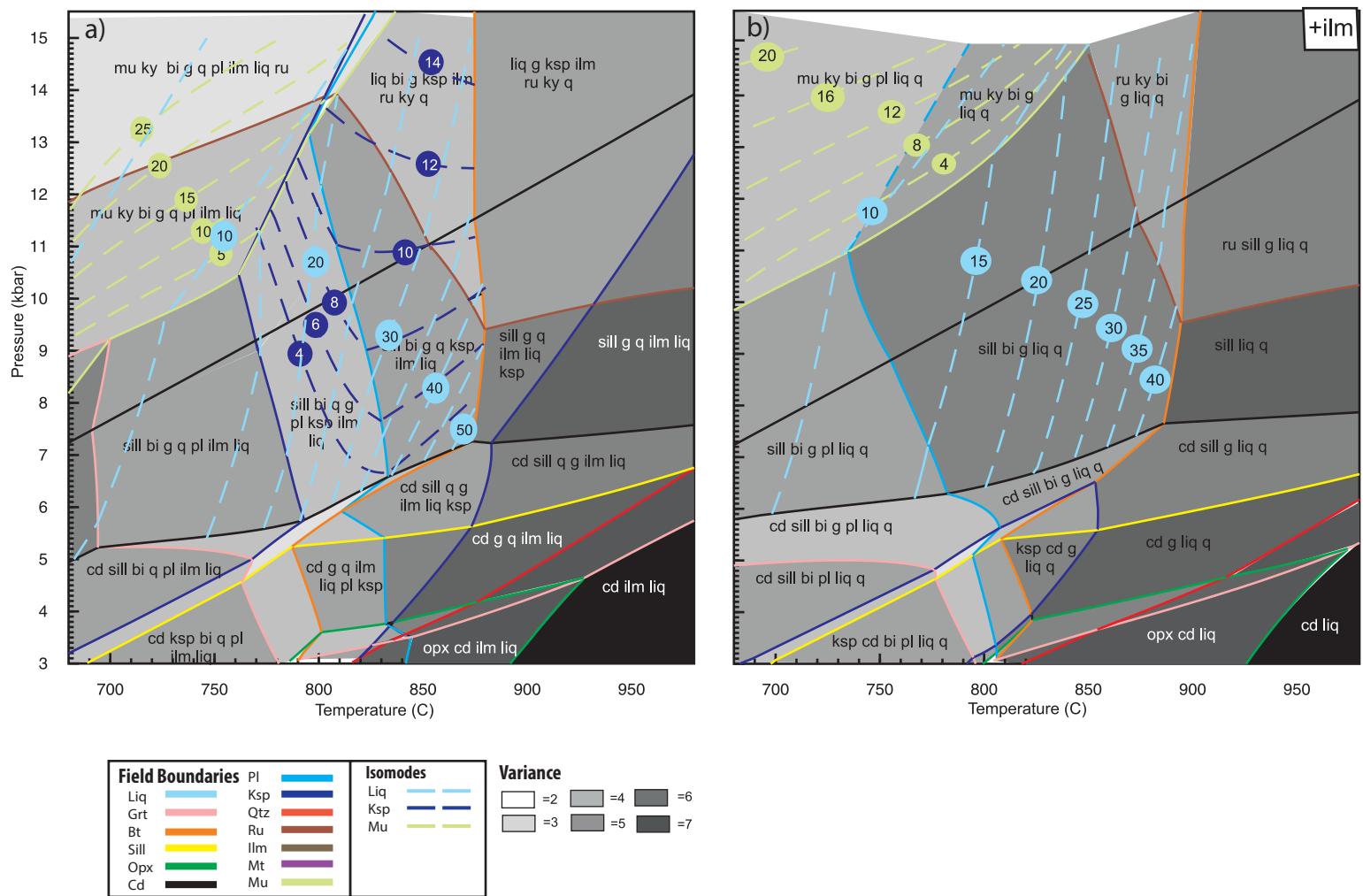
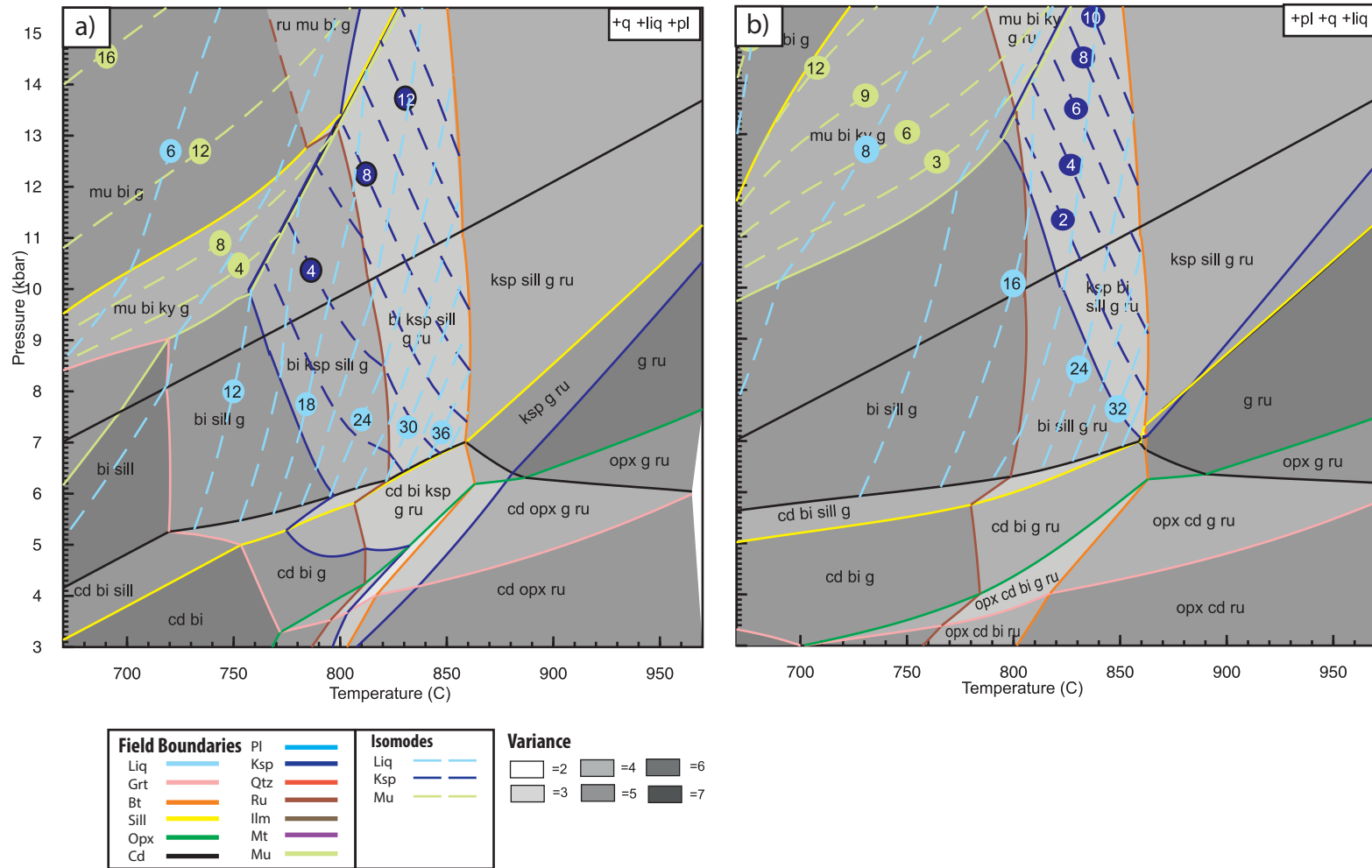


Figure 4.2. For sample 10-AI-114-B1: (a) Melt-added and (b) water-added pseudosections with isomodes of liquid, muscovite and K-feldspar. Phases in the top right box are stable throughout.



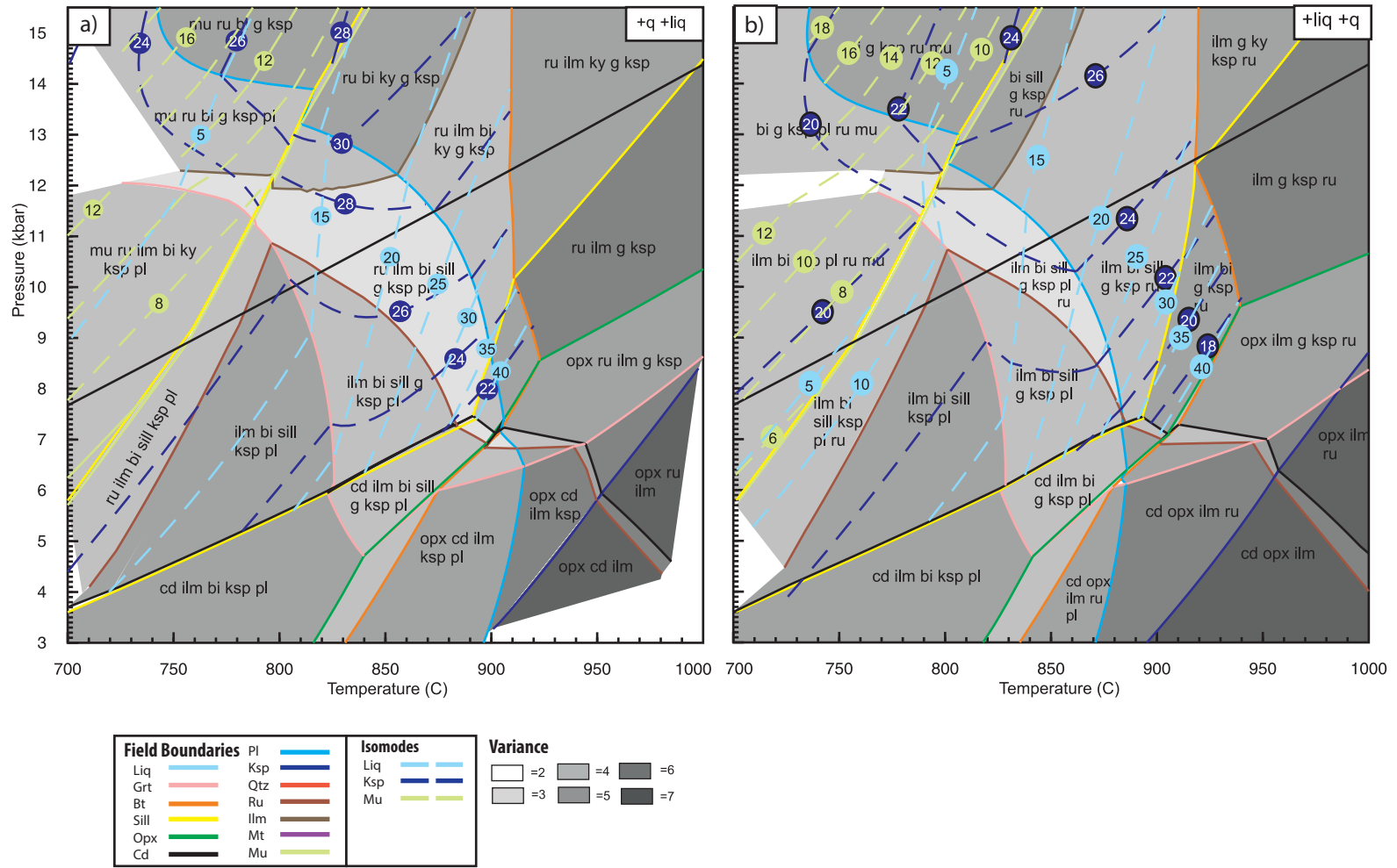


Figure 4.4. For sample HJ-57b: (a) Melt-added and (b) water-added pseudosections with isomodes of liquid, muscovite and K-feldspar. Phases in the top right box are stable throughout.

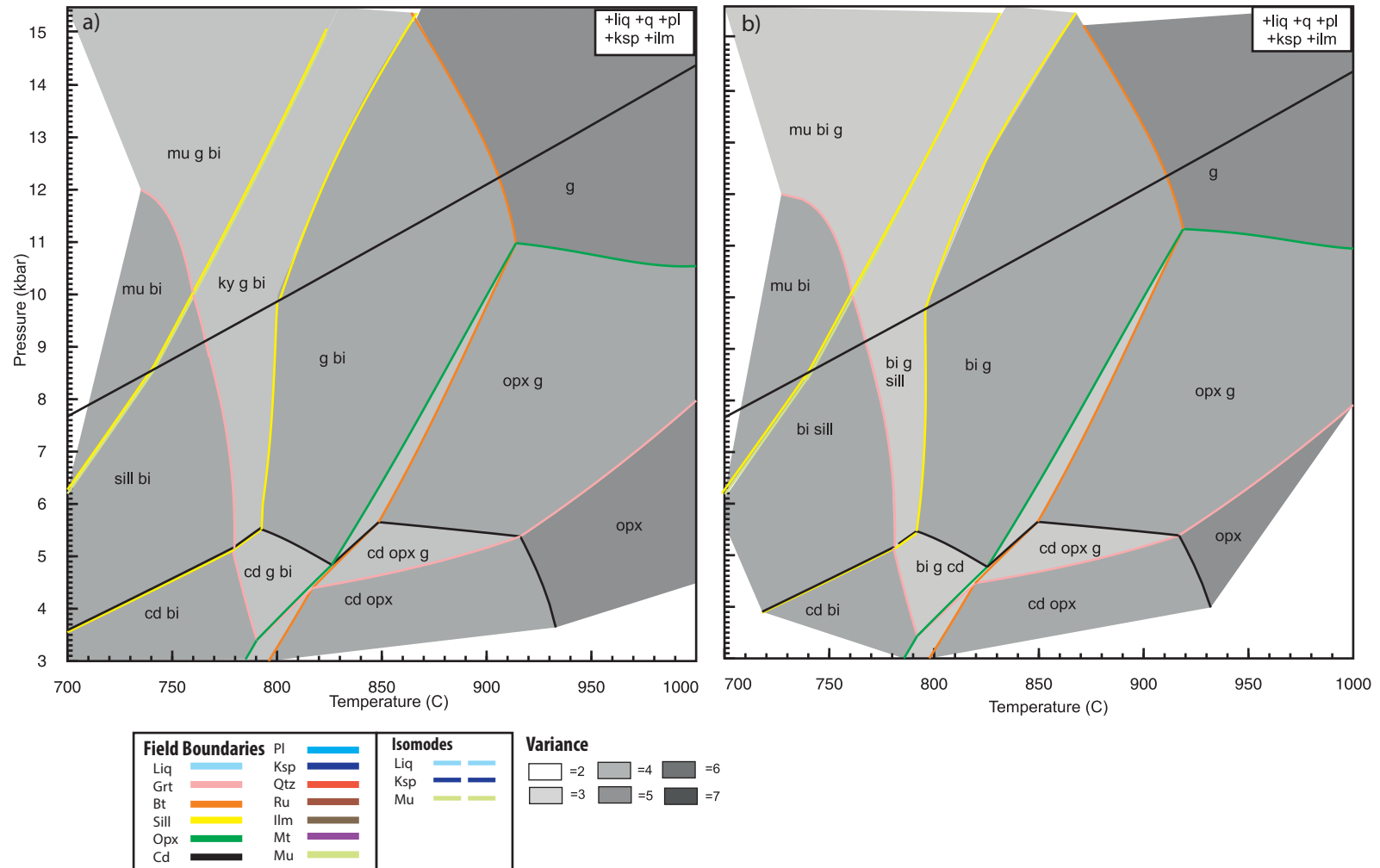


Figure 4.5. For sample 10-AI-76: (a) Melt-added and (b) water-added pseudosections. Phases in the top right box are stable throughout.

CHAPTER 5: SUMMARY AND CONCLUSIONS

This study is an investigation of mid-*P* granulite facies aluminous gneisses from the hinterland of the central Grenville Province, using textures, mineral chemistry and phase equilibria modeling, to elucidate their metamorphic and partial melting history.

The rocks belong to three supracrustal lithologic associations exposed in the Manicouagan and Lac du Milieu areas: the Complexe de la Plus Value in Lac du Milieu (PLV-LM), the Layered Bimodal Sequence (LBS) and the Gabriel Aluminous Gneisses (GAG), that are derived from hydrothermally altered felsic protoliths. Despite having a wide range of textures and bulk compositions, all samples contain the peak mineral assemblage $G + Bi + Q + Ksp \pm Pl \pm Sill$, with retrograde cordierite in some rocks of the PLV-LM and GAG, and show textural evidence of partial melting and melt loss.

The samples are divided into two groups, sillimanite-rich and sillimanite-poor. In the former, sillimanite is dispersed throughout the matrix in modal proportions of $>5\% Sill/(G+Bi+Sill+Cd)$, and is part of the peak assemblage, whereas in the latter, sillimanite is confined to inclusions in garnet, garnet rims and/or in aluminous nodules and in one case, is absent altogether. This division is also evident in the bulk compositions, where sillimanite-rich and poor rocks plot above and below 25% on the A apex of the AFM diagram, respectively.

Phase equilibria modeling in the $\text{Na}_2\text{O}-\text{CaO}-\text{K}_2\text{O}-\text{FeO}-\text{MgO}-\text{Al}_2\text{O}_3-\text{SiO}_2-\text{H}_2\text{O}-\text{TiO}_2-\text{O}$ (NCKFMASH_{THO}) system using Thermocalc allowed for the investigation of phase relationships at different $P-T$ conditions, and the evaluation of the partial melting history and $P-T$ paths. Pseudosections were calculated using the bulk compositions of the samples, and show different topologies for the sillimanite-rich and poor rocks. In both cases the $P-T$ stability field of the peak mineral assemblage of (Field I) is constrained on the low- T side by the solidus. However, the high- T boundary of Field I is marked by the biotite-out phase boundary in the case of the sill-rich rocks, and the orthopyroxene-in phase boundary in the case of the sill-poor rocks.

For both groups of rocks Field I was constrained to 800–900°C and 6–11 kbar, with melt solidification in the range of 800–865°C and 6–8 kbar. The presence of sillimanite inclusions in garnet indicates that garnet grew in the presence of sillimanite along the prograde portion of the $P-T$ path. Along with the presence of retrograde cordierite in several samples, the paths followed by the rocks are consistent with moderate dP/dT gradient ‘hairpin’ $P-T$ paths. The similarity of the $P-T$ paths predicted by phase equilibria modelling in the rocks from the three locations, which are separated by several tens of kilometers, suggests that this portion of the mid- P hinterland of the central Grenville Province experienced a rather uniform metamorphic evolution during the Grenvillian Orogeny.

This study also investigated the role of Fe^{3+} on the phase stability of the mid- P aluminous rocks. One of the advantages of the NCKFMASH_{THO} system is that it

incorporates Fe^{3+} ; however, because conventional mineral analytical techniques do not discriminate between Fe^{2+} and Fe^{3+} , the values used in the modeling are generally assumed. Most previous investigations that have addressed this issue focused on low- P granulites or on ultrahigh- T rocks, but because in mid- P rocks biotite is potentially a major contributor to the bulk Fe^{3+} , the Fe^{3+} of biotite from selected samples was analysed by Mössbauer spectroscopy in this study. The results obtained were $<5\%$ of $\text{Fe}^{3+}/\text{Fe}_{\text{tot}}$, which is lower than what is generally assumed. Pseudosections calculated with the measured Fe^{3+} are generally consistent with the thin section mineral assemblages, textures, and mineral chemistry. In addition, the role of increasing bulk Fe^{3+} was examined. This resulted in addition, or change in proportion of minor phases such as rutile, ilmenite and magnetite as well as minor shifts in phase boundaries and composition isopleths of ferromagnesian minerals to a small degree. In one instance, sillimanite, an important mineral involved in melting reactions, was absent in pseudosections calculated with low Fe^{3+} but present in those calculated with higher Fe^{3+} , presumably a result of Fe^{3+} substitution for Al in this phase. However, it was found that P - T paths remained largely unaffected.

Finally, the methods commonly used to determine topologies relevant to the prograde portion of P - T paths in anatectic aluminous systems were compared. These account for melt loss by adding melt or water to the bulk composition in order to saturate the solidus. The two methods yielded phase equilibria diagrams with major differences in the topologies in three of the five modeled samples. The former method is more rigorous

and in all cases, the topologies calculated with it are consistent with the rock data, therefore it is the method of choice.

REFERENCES

- Beaumont, C. Jamieson, R.A., Nguyen, M.H. 2010. Models of large hot orogens containing a collage of reworked and accreted terranes. *Canadian Journal of Earth Sciences*, 47, 485–515.
- Beaumont, C., Nguyen, M.H., Jamieson, R.A., Lee, B. 2006. Crustal flow modes in large hot orogens. *Geological Society of London Special Publication* 268, 91–145.
- Boger, S. D., White, R. W., Schulte, B., 2012. The importance of iron speciation ($\text{Fe}^{2+}/\text{Fe}^{3+}$) in determining mineral assemblages: an example from the high-grade aluminous metapelites of southern Madagascar. *Journal of Metamorphic Geology*, 30, 997-1018.
- Brown, M. 2007. Crustal melting and melt extraction, ascent and emplacement in orogens: mechanism and consequences. *Journal of Geological Society of London*, 164, 709–730.
- Cesare, B., Meli, S., Nodari, L., Russo, U., 2005. Fe^{3+} reduction during biotite melting in graphitic metapelites: another origin of CO_2 in granulites. *Contributions to Mineralogy and Petrology*, 149, 129-140.
- Coggon, R. and Holland, T. J. B., 2002. Mixing properties of phengitic micas and revised garnet-phengite thermobarometers. *Journal of Metamorphic Geology*, 20, 683–696.
- Dachs, E. and Benisek, A., 1995. The stability of annite + quartz: reversed experimental data for the reaction $2 \text{annite} + 3 \text{quartz} \rightleftharpoons 2 \text{sanidine} + 3 \text{fayalite} + 2 \text{H}_2\text{O}$. *Contributions to Mineralogy and Petrology*, 121, 380–387.
- Diener, J.F.A. and Powell, R., 2010. Influence of ferric iron on the stability of mineral assemblages. *Journal of Metamorphic Geology*, 28, 599–613.
- Dunning G, and Indares, A., 2010. New insights on the 1.7–1.0 Ga crustal evolution of the central Grenville from the Manicouagan-Baie Comeau transect. *Precambrian Research*, 180, 204–226.

- Dyar, M.D., Lowe, E.W., Guidotti, C.V., Delaney, J.S., 2002. Fe³⁺ and Fe²⁺ partitioning among silicates in metapelites: A synchrotron micro-XANES study. *American Mineralogist*, 87, 514–52.
- Ericsson T, Wäppling R .1976. Texture effects in 3/3-1/2 Mössbauer spectra. *Journal of Physics (Paris) Colloque*, C6, 719-723.
- Ferry, J. M. and Spear, F. S., 1978. Experimental calibration of the partitioning of Fe and Mg between biotite and garnet. *Contributions of Mineralogy and Petrology*, 66, 113–117.
- Gower, C. F. and Krogh, T. E. 2002. A U–Pb geochronological review of the Proterozoic history of the eastern Grenville Province. *Canadian Journal of Earth Sciences*, 39, 795–829.
- Groppo, C., Rolfo, F., Indares, A. 2012. Partial melting in the Higher Himalayan Crystallines of eastern Nepal; the effect of decompression and implications for the 'channel flow' model. *Journal of Petrology*, 53, 1057-1088.
- Groppo, C., Rolfo, F., Mosca, P. 2013. The cordierite-bearing anatectic rocks of the higher Himalayan crystallines (eastern Nepal): low-pressure anatexis, melt productivity, melt loss and the preservation of cordierite. *Journal of Metamorphic Geology*, 31,187-204.
- Guilmette , C., Indares, A., Hébert, R. 2011. High-pressure anatectic paragneisses from the Namche Barwa, Eastern Himalayan Syntaxis: Textural evidence for partial melting, phase equilibria modeling and tectonic implications. *Lithos*, 124, 66-81.
- Harley, S. L., Thompson, P. P., Hensen, B. J., Buick, I. S. 2002. Cordierite as a sensor of fluid conditions in high-grade metamorphism and crustal anatexis. *Journal Of Metamorphic Geology*, 20(1), 71-86.
- Hindemith, M. A., 2013. Petrography and geochemistry of hydrothermally altered volcanic rocks metamorphosed at granulite-facies conditions: an example from the central grenville province. Masters Thesis. Memorial University of Newfoundland. 131 Pages.
- Hodych, J.P., and Dunning, G.R. 1992. Did the Manicouagan impact trigger end-of-Triassic mass extinction? *Geology*, 20, 51–54.
- Holland, T. J. B. and Powell, R., 1998. An internally-consistent thermodynamic data set for phases of petrological interest. *Journal of Metamorphic Geology*, 16, 309–343.
- Holland, T. J. B. and Powell, R., 2003. Activity-composition relations for phases in petrological calculations: an asymmetric multicomponent formulation. *Contributions to Mineralogy and Petrology*, 145, 492–501.

- Holness, M.B., Cesare, B., Sawyer E.W. 2011. Melted Rocks under the Microscope: Microstructures and Their Interpretation. *Elements*, 7, 247-252.
- Indares, A., and Dunning, G. 2004. Crustal architecture above the high-pressure belt of the Grenville Province in the Manicouagan area: new structural, petrologic and U–Pb age constraints. *Precambrian Research*, 130, 199-208.
- Indares, A. and Moukhsil, A., 2013. Geon 12 crustal extension in the central Grenville Province, implications for the orogenic architecture and potential influence on the emplacement of anorthosites. *Canadian Journal of Earth Sciences*, 50, 955-966.
- Indares, A.D., White, R.W., Powell, R., 2008. Phase equilibria modelling of kyanite bearing anatectic paragneisses from the central Grenville Province. *Journal of Metamorphic Geology*, 26, 815–836.
- Jamieson, R.A. and Beaumont, C., 2011. Coeval thrusting and extension during post-convergent ductile flow - implications for exhumation of high-grade metamorphic rocks. *Journal of Metamorphic Geology*, 29, 33–51.
- Jamieson, R.A., Beaumont, C., Nguyen, M.H., Culshaw, N.G., 2007. Synconvergent ductile flow in variable-strength continental crust: Numerical models with application to the western Grenville orogen. *Tectonics*, 26, 1–23.
- Jamieson, R.A., Beaumont, C., Warren, C.J., Nguyen, M.H., 2010. The Grenville Orogen explained? Applications and limitations of integrating numerical models with geological and geophysical data. In: *Lithoprobe - parameters, processes and the evolution of a continent* (Lithoprobe Synthesis Volume II, eds Clowes, R M., and Skulski, T.). *Canadian Journal of Earth Sciences*, 47, 517–539.
- Korhonen, F.J., Powell, R., Stout, J.H., 2012. Stability of sapphirine + quartz in the oxidized rocks of the Wilson Lake terrane, Labrador: calculated equilibria in NCKFMASHTO. *Journal of Metamorphic Geology*, 30, 21–36.
- Lasalle, S., Dunning, G., Indares, A., 2014. In situ LA–ICP–MS dating of monazite from aluminous gneisses: insights on the tectono-metamorphic history of a granulite-facies domain in the central Grenville Province. *Canadian Journal of Earth Sciences*, 51, 558–572.
- Lasalle, S., Fisher, C.M., Indares, A., Dunning, G., 2013. Contrasting types of Grenvillian granulite facies aluminous gneisses: insights on protoliths and metamorphic events from zircon morphologies and ages. *Precambrian Research*, 228, 117–130.

- Lasalle, S. and Indares, A., 2014 Anatectic record and contrasting P - T paths of aluminous gneisses from the central Grenville Province. *Journal of Metamorphic Geology*, 32, 627-646.
- Letourneau, M. 2011. Anatectic aluminous gneisses from the mesoproterozoic Complexe de la Plus-Value, Grenville Province, Quebec. Memorial University: Honours thesis.
- Moukhsil, A., Solgadi, F., Lacoste, P., Gagnon, M., David, J., 2012. Geologie de la region du lac du Milieu. Ministere des Ressources naturelles et de la Faune, *RG 2012-01*. 1-31.
- Nesse, William D. 2000. Introduction To Mineralogy. United States: Oxford University Press: New York, NY, United States.
- Patiño-Douce, A.E. and Johnston, A.D., 1991. Phase equilibria and melt productivity in the pelitic system; implications for the origin of peraluminous granitoids and aluminous granulites. *Contributions to Mineralogy and Petrology*, 107, 202-218.
- Patrick, M. E., 2013 Metamorphic investigation of anatectic aluminous gneisses from the Complexe de la Plus-Value, Grenville Province. Honours thesis, Memorial University of Newfoundland.
- Platten, I. M., 1983. Partial melting of semipelite and the development of marginal breccias around a late Caledonian minor intrusion in the Gremplan highlands of Scotland. *Geological Magazine*, 120, 37-49.
- Powell, R., Holland, T.J.B. 1988 An internally consistent thermodynamic dataset with uncertainties and correlations: 3. Applications to geobarometry, worked examples and a computer program. *Journal of Metamorphic Geology*, 6, 173-204.
- Powell, R., Holland, T.J.B. 2008. On thermobarometry. *Journal of Metamorphic Geology* 26, 155-179.
- Rivers, T., 2008 Assembly and preservation of lower, mid and upper orogenic crust in the Grenville Province – Implications for the evolution of large hot long-duration orogens. *Precambrian Research*, 167, 237-259.
- Rivers, T., 2012. Upper-crustal orogenic lid and mid-crustal core complexes: signature of a collapsed orogenic plateau in the hinterland of the Grenville Province. *Canadian Journal of Earth Sciences*, 49, 1-42.
- Rivers T, Culshaw N, Hynes A, Indares A, Jamieson R, Martignole J. 2012. The Grenville Orogen – A post-LITHOPROBE perspective. Chapter 3 In Tectonic Styles in Canada: The LITHOPROBE Perspective. (eds JA Percival, FA Cook, and RM Clowes) *Geological Association of Canada, Special Paper 49*, 97-236.

- Rivers, T. and Corrigan, D. 2000. Convergent margin on southeastern Laurentia during the Mesoproterozoic: tectonic implications. *Canadian Journal of Earth Sciences* 37, 359–383.
- Rivers, T., Martignole, J., Gower, C.F., Davidson, A., 1989. New tectonic divisions of the Grenville Province, Southeast Canadian Shield. *Tectonics* 8, 63-84.
- Rosenberg, C.L. and Handy, M.R., 2005. Experimental deformation of partially melted granite revisited; implications for the continental crust. *Journal of Metamorphic Geology*, 23, 19–28.
- Sawyer, E. W., 1999. Criteria for the recognition of partial melting. *Physics and Chemistry of the Earth*, 24, 269–279.
- Sawyer, Edward W. 2008. Atlas Of Migmatites. *Canadian Mineralogist*. Special Publication 9.
- Shaffer, M., Gu, Y., and Rohde, M. 2008. Practical Applications for the Silicon Drift Xray Detector in SEM-Platformed Image Analysis: The Bruker-MLA in Practice. *In* SME Annual Meeting 2007 and CMS 109th National Western Conference 2007 The Power of Mining: Energy's Influence, Denver, CO, U.S.A., 25-28 February, 2007, 1(Preprint 07-029), 1-6.
- Spear, Frank S. 1993. Metamorphic Phase Equilibria And Pressure-Temperature-Time Paths Monograph Series. United States: Mineralogical Society of America : Washington, DC, United States, 1993. 799 Pages.
- Spear, F.S., Kohn, M.J., Cheney, J.T., 1999. P–T paths from anatectic pelites. *Contributions to Mineralogy and Petrology*, 134, 17–32.
- Strowbridge, S., 2006. Metamorphic evolution of anatectic metapelites from the Gabriel high strain zone, Grenville Province. Masters Thesis. Memorial University of Newfoundland.
- Tajcmanova, L., Connolly, J. A. D., Cesare, B. 2009. A thermodynamic model for titanium and ferric iron solution in biotite. *Journal of Metamorphic Geology*, 27, 153-165.
- Taylor-Jones, K. and Powell, R., 2010. The stability of sapphirine + quartz: calculated phase equilibria in FeO–MgO–Al₂O₃– SiO₂–TiO₂–O. *Journal of Metamorphic Geology*, 28, 615–633.
- Vernon, R. H. and Collins, W. J., 1988. Igneous microstructures in migmatites. *Geology*, 16, 1126–1129.

- White, R. W., Powell, R., Holland, T. J. B., Worley, B. A., 2000. The effect of TiO₂ and Fe₂O₃ on metapelitic assemblages at greenschist and amphibolite facies conditions: mineral equilibria calculations in the system K₂O–FeO–MgO–Al₂O₃–SiO₂–H₂O–TiO₂–Fe₂O₃. *Journal of Metamorphic Geology*, 18, 497–511.
- White, R.W. and Powell, R. 2002. Melt loss and the preservation of granulite facies assemblages. *J. Metamorphic Geology*, 20, 621-632.
- White, R. W., Powell, R., Clarke, G. L., 2002. The interpretation of reaction textures in Fe-rich metapelitic granulites of the Musgrave Block, central Australia: constraints from mineral equilibria calculations in the system K₂O–FeO–MgO–Al₂O₃–SiO₂–H₂O–TiO₂–Fe₂O₃. *Journal of Metamorphic Geology*, 20, 621–632.
- White, R.W., Powell, R., Holland, T.J.B., 2007. Progress relating to calculation of partial melting equilibria for metapelites. *Journal of Metamorphic Geology*, 25, 511–527.
- White, R. W., Powell, R., Holland, T. J. B., Worley, B. A., 2000. The effect of TiO₂ and Fe₂O₃ on metapelitic assemblages at greenschist and amphibolite facies conditions: mineral equilibria calculations in the system K₂O–FeO–MgO–Al₂O₃–SiO₂–H₂O–TiO₂–Fe₂O₃. *Journal of Metamorphic Geology*, 18, 497–511.
- White, R. W., Powell, R., Johnson, T. E., 2014. The effect of Mn on mineral stability in metapelites revisited: new a–x relations for manganese-bearing minerals. *Journal of Metamorphic Geology*, 32, 809-828.